Morphology controlled synthesis of 1-D-nanomaterials for electrocatalysis and energy storage applications

Dissertation

Zur Erlangung des akademischen Grades
Doktor der Ingenieurwissenschaften
(Dr.-Ing.)
der Technischen Fakultät
der Christian-Albrechts-Universität zu Kiel

Farrukh Iqbal Dar

Kiel
April, 2016

1. Gutachter	Prof. Dr. Franz Faupel
2. Gutachter	Prof. Dr. Lorenz Kienle

Datum der mündlichen prüfung: 13.07.2016

Abstract

This dissertation is about morphology controlled synthesis of one dimensional (1 D) nanomaterials for electrocatalysis and supercapacitance applications. Template assisted electrodeposition technique was employed to grow 1 D nanomaterials; the morphology of which could be varied from nanotubes to nanorods, taking advantage of two simple and cost effective methods.

In the first method, morphology was controlled by controlling the time of electrodeposition inside the anodic aluminum oxide (AAO) template while keeping constant the other deposition parameters, such as potential, concentration and pH of the electrolyte. The presence of sputtered gold on the inside walls of the AAO template played key role by providing the first nucleation sites for the formation of nanotube walls that are subsequently thickened through the gradual increase of the deposition time. With this method, we could successfully tune the wall thickness of gold (Au), platinum (Pt) and palladium (Pd) nanotubes until closure and the formation of nanorods. Moreover, this method was extended to the processing of bimetallic and trimetallic nanotubes by the sequential deposition of one metal on the other. Furthermore, Pt nanotubes modified with monolayers of tin (Sn) and ruthenium (Ru) were also synthesized. The surface modification of the Pt nanotubes was attained through underpotential deposition of Sn and Ru.

In the second method, 1 D nanotubes of nickel (Ni) were grown inside the template using the method outlined above. These Ni nanotubes were oxidized to yield 1D-NiO nanostructures; the morphology of which was controlled from thin walls to thick walls and completely closed nanorods via adjusting the annealing time and temperature. Annealing thus helped controlling the morphology of the NiO nanotubes through advancing layer of oxide with the annealing time.

The synthesized 1 D nanomaterials in this thesis were tested as electrodes for direct liquid fuel cells and electrochemical supercapacitors for energy conversion and energy storage applications, respectively. Among the synthesized noble metal 1D nanomaterials, Pt and Pd were characterized for electrooxidation of methanol and formic acid, respectively, in acidic medium while NiO was tested for supercapacitance applications in basic medium. All our nanomaterials exhibited high electrochemical activity towards electrocatalysis and supercapacitance properties. In addition, our modified Pt nanotubes showed efficient and enhanced electrooxidation of methanol as compared to bare Pt nanotubes due to a bifunctional mechanism. Furthermore, a strong dependence of the electrochemical properties on morphology was observed where, understandably, superior electrochemical properties were observed for thin wall nanotubes owing to the large active surface area involved.

Contents

1 Introduction

1.1 Synthesis of nanomaterials

Nanomaterials exhibit novel physiochemical properties such as improved plasticity and strength [1], modified thermal stability [2], marked optical properties (localized surface plasmons) [3], higher reactivity [4] and faster charge transport [5]. Due to these superior properties, nanomaterials are preferred over corresponding bulk materials in various applications such as electrocatalysis in fuel cells, biosensing, labeling, cancer therapy, gas sensors, molecular detection and energy storage [6-12].

To further explore their unique and fascinating properties and realize new potential applications, synthesis of nanomaterials with suitable size, shape, morphology and aspect ratio is the first important step. Moreover, fast track progress in nanotechnology demands low cost, less complex and high production rate synthesis techniques of these minuscule nanostructures (NSs). There are various methods to synthesize nanomaterials that can be categorized based on the process (physical or chemical) or phase (liquid or gas) involved or size and dimension (zero, one and two dimensional) of the end product. However, for synthesis of one dimensional (1D) nanomaterials such as nanorods (NRs) and nanotubes (NTs) solution based chemical methods, physical methods, nanolithography and template assisted methods are more popular as described below briefly along with their main advantages and disadvantages.

In solution based approach controlled wet chemical reactions are employed to synthesize nanostructures [13-16]. For example, solvothermal chemical synthesis is among the most popular and widely employed solution-based techniques [15, 16]. The solvothermal technique refers to dissolving and recrystallizing a material in a solvent under high temperature and pressure conditions. The solvent is carefully selected to dissolve the precursor material and appropriate temperature and pressure are employed accordingly. The higher temperature also increases the solubility by facilitating the precursor interaction with the solvent. The typical process of recrystallization and crystal growth is carried out in an autoclave at appropriate reaction conditions (temperature and pressure), after placing in it the solvent containing material precursor and crystal growth control agent. For example 1D TiO_2 NRs have been synthesized by solvothermal route using titanium (IV) isopropoxide in the presence of isopropyl alcohol and acetic acid for dye-sensitized solar cells (DSSC) applications [15]. The processed 1D TiO_2 NRs electrode possessed large surface area and showed better photovoltaic performance (conversion efficiency) as compared to the commercial DP-25 TiO_2 nanoparticles due to its high dye absorption ability, good light harvesting and fast electron transport [15]. Similarly hierarchical $NiCo_2O_4$ nanowires and nanosheets have been synthesized on carbon fiber paper with solvothermal technique to analyze the morphology dependent pseudocapacitance [16]. The morphologies of $NiCo_2O_4$ (nanowires and nanosheets) were controlled by changing the solvent from methanol to water. The pseudocapacitance performance of carbon fiber supported nanosheets electrode was much better than nanowires in terms of specific capacitance and recycling life. This improved performance is attributed to the hierarchical nanosheets arrays structure and large specific surface area of the nanosheets which provides not only more active sites and fast penetration but also accommodate strain during cycling [16].

The solution based approach is an inexpensive and environment friendly technique to synthesize crystalline 1D nanostructure with controlled size and shape. The disadvantages are the high cost of the initial equipment and inability to monitor the crystal growth. Furthermore, the process is considered relatively complex due to the chemical reaction and crystal growth mechanism involve. The purity and homogeneity of the products are also generally not ideal.

Another competitive method to grow 1D NSs is the glancing angle deposition (GLAD) technique which is an extension to the physical vapor deposition (PVD). Thus, it is a gaseous phase

technique to synthesize different nano-sized columns with controlled surface morphology and structure [17-20]. In GLAD the deposition flux is directed onto a rotating substrate in a position that makes a large angle with the perpendicular to the substrate surface. The shadowing effect during film growth in GLAD produces columnar structures. The parameters which define the morphology of the columns in this technique are incident angle, growth rate and substrate rotational speed. The structural design of the columns (C-shape, S-shape and zigzag shape) is controlled through the incidence angle, while columns morphology (matchstick, helical or vertical) is controlled by proportionally changing the deposition rate and rotational speed [21,22]. A recent example of GLAD from literature is the silica thin films synthesized by RF magnetron sputtering at four different oblique angles (45°, 60°, 75°, 85°) [20]. The films showed featureless to columnar structure depending upon the incident angle. The produced nanostructured silica films were characterized for their optical and wetting properties. The nanostructured films exhibited morphology dependent properties, for example the minimum reflectance (3.15 %) and maximum transmittance (93.43 %) was achieved from film deposited at 85°. Similarly wettability results showed that minimum water contact angle is measured for the film deposited with highest oblique angle (85°). Thus, produced films showed high potential for use in applications such as antireflection and self-cleaning coatings.

The main advantage of the GLAD is its ability to control the morphology and shape of 1D NSs during film growth by controlling the incident angle, deposition rate and rotational speed of substrate. Moreover, being a PVD technique, most of the materials can be processed to nano columns. Disadvantages: This sophisticated technique is based on vacuum system and requires relatively complex equipment which also means high initial investment. The technique relies only on shadowing effect to grow columnar NSs which results in non-uniform diameter of columns on planar substrates. The synthesis of discrete nanostructures such as self-standing nanorods on a substrate is therefore not possible. Also the synthesis of multi-materials is difficult and complex because of different evaporation temperatures or sputtering rates of different materials.

Nanolithography is a top-down approach in which NSs are patterned by the combination of lithography, etching and deposition. Photolithography [23,24] and electron beam lithography [24,25] are the main advanced nanolithography techniques to synthesize 1D NSs. These

techniques provide a way to carve NSs on substrates and typical process involves coating the photoresist, masking with the pattern, exposing to ultraviolet light or electron beam and finally etching the exposed surfaces of the substrate. An interesting and worth mentioning combination of electron beam lithography and self- assembly technique has also been employed to fabricate nanostructures [26,27] For example gold nanoparticle cluster arrays were fabricated by this combination in two steps [27]. At first, electron beam lithography is employed to carve a template with regular structure of nano wells on photoresist present on gold coated glass. The exposed gold surface was functionalized with positively charged monolayer of amino-terminated PEGs (polyethylene glycol). In the second step 40 nm gold particles were coated with negatively charged monolayer of carboxyl-terminated PEGs before these were self-assembled electrostatically in nano wells. The nanoparticle cluster arrays of different sizes (average number of particles in a cluster) and edge to edge distances between clusters were synthesized and characterized for surface enhanced Raman scattering (SERS). The SERS signals showed strong dependency on size and edge to edge distance between clusters. The synthesized nanoparticle cluster arrays were not only able to induce strong signals from small molecules but also from whole three different bacterial cells tested, which enabled to distinguish them optically.

With nanolithography techniques structures are directly and precisely patterned on to the substrate. The electron beam lithography has a high resolution (20 nm) due to small wavelength of the electrons as compared to conventional photolithography with resolution of 1 µm. The main disadvantages of lithography techniques are high cost due to expensive equipment involved, complexities in implementation such as precise alignment of mask with the pattern on substrate, careful control of density of defects and slow nature of the lithography process.

Template assisted synthesis is another widely employed method to grow 1D NSs [28]. In this method a sacrificial template with a desired structure is utilized to grow the NSs, later on which is selectively removed to expose the NSs. Therefore, template defines the size and morphology of the NSs. There are different techniques which employ templates such as electrodeposition [11], sol-gel [29] and layer by layer assembly [30] to grow NSs; however, last two are usually restricted to metal oxide and organic polymer or organic-inorganic NSs respectively. Therefore, template assisted electrodeposition is most suitable and widely employed technique to synthesis metallic 1D NSs [11,31-37]. For example platinum (Pt) nanowires were synthesized by

electrodepositing Pt inside the nano channels of track etched poly carbonate template [37]. The synthesized Pt nanowires were annealed at 200 °C, 400 °C and 600 °C and subsequently tested for methanol oxidation and oxygen reduction reactions. All the Pt nanowires exhibited better electrocatalytic activity than commercial carbon supported Pt catalyst for both the reactions.

Thus, analysis of the above mentioned techniques suggests that, for supported metallic 1D NSs the template aided electrochemical deposition is one of the most suitable and applicative technique. It can be advantageously compared to other techniques due to its low cost of processing, simplicity, easy and direct control of shape and dimension and highly ordered NSs assembly.

In this dissertation NTs and NRs of Pt, Pd, Au and Ni/NiO as well as multimaterial NTs have been synthesized by electrodeposition method using anodic aluminum oxide template (AAO). It is well known that unique physiochemical properties of the nanomaterials are associated not only to the small size but also to the shape, structure and morphology [15,16,20] which is also briefly discussed with examples and references in chapter 2 section 2.3. Therefore, emphasis is placed on controlling the processing conditions and through them the morphology of the NSs in order to achieve large area substrates of highly ordered, small aspect ratio NRs and NTs. The judicious choice of electrolyte composition, deposition and annealing conditions allowed us to make ordered and self-standing NRs and NTs with controlled morphology and subsequently to investigate their electrocatalytic and capacitive behaviors. We processed and controlled the morphology from thin walls to thick walls NTs and to completely filled nanorods. The morphology control is attained via electrodeposition time in case of mono and multi-metallic noble metal NSs, and annealing time in case of NiO NSs while keeping the other deposition parameters constant. The importance of nanomaterials in energy conversion and energy storage is well established and has been extensively studied [38]. Therefore, we also evaluated the performance of our synthesized 1D NSs for energy conversion and energy storage applications. Among the synthesized noble metal NSs, Pt and Pd were tested as electrodes, for electrocatalysis of small organic molecules that is methanol and formic acid respectively in acidic media, and NiO NSs were tested as electrode for supercapacitance properties in NaOH.

1.2 Organization of the thesis

This dissertation consists of seven chapters including the current one. Chapter 2 discusses some of the theoretical concepts of electrodeposition, template aided electrochemical synthesis of NSs, morphology dependant properties and characterization techniques related to this work. Chapter 3 describes the synthesis of noble metal mono/hetero-NSs with controlled morphology. Chapter 4 describes the catalysis experiments of the synthesized Pt and Pd NSs using small organic molecules that is, CH_4OH and HCOOH. Chapter 5 describes the synthesis and catalysis of Pt NTs the surface of which is modified with Ru and Sn add atoms. Chapter 6 presents the synthesis and morphology control of NiO NSs through annealing conditions. The morphology dependant supercapacitance behavior is experimentally shown in the same chapter. Chapter 7 presents the summary of the principal results and brief experimental discussions followed by an outlook.

References

[1] C. C. Koch, D.G. Morris, K. Lu and A. Inoue, *Ductility of nanostructured materials*, MRS Bulletin **24**(2), 54–58 (1999).

[2] M. Rieth, W. Schommers and S. Baskoutas, *Thermal stability and specific material properties of nanosystems*, Modern Physics Letters B **14**, 621–629 (2000).

[3] A. Polman and H. A. Atwater, *Plasmonics: optics at the nanoscale*, Materials Today **8**(1), 56 (2005).

[4] A. T. Bell, *The Impact of Nanoscience on Heterogeneous Catalysis*, Science **299**(5613), 1688–1691 (2003).

[5] W. Y. Kim, Y. C. Choi, S. K. Min, Y. Cho and K. S. Kim, *Application of quantum chemistry to nanotechnology: electron and spin transport in molecular devices*, Chemical Society Reviews **38**(8), 2319–2333 (2009).

[6] R. Sardar, A. M. Funston, P. Mulvaney and R. W. Murray, *Gold Nanoparticles: Past, Present, and Future*, Langmuir **25**(24), 13840–13851 (2009).

[7] J. N. Anker, W. P. Hall, O. Lyandres, N. C. Shah, J. Zhao and R. P. V. Duyne, Nat. Mater. *Biosensing with plasmonic nanosensors* **7**, 442–453 (2008).

[8] M. E. Aubin, D. G. Morales and K. H. Schifferli, *Labeling Ribonuclease S with a 3 nm Au Nanoparticle by Two-Step Assembly*, Nano Lett. **5**(3), 519–522 (2005).

[9] X. Huang and M. A. El-Sayed, *Gold nanoparticles: Optical properties and implementations in cancer diagnosis and photothermal therapy*, J. Adv. Res. **1**, 13–28 (2010).

[10] D. M. Gattia, M. V. Antisari, L. Giorgi, R. Marazzi, E. Piscopiello, A. Montone, S. Bellitto, S. Licoccia and E. Traversa, *Study of different nanostructured carbon supports for fuel cell catalysts*, J. Power Sources **194**, 243–251 (2009).

[11] S. Habouti, M. Mátéfi-Tempfli, C. H. Solterbeck, M. Es-Souni, S. Mátéfi-Tempfli and M. Es-Souni, *On-substrate, self-standing Au-nanorod arrays showing morphology controlled properties*, Nano Today **6**, 12–19 (2011).

[12] M. Zhi, C. Xiang, J. Li, M. Li and N. Wu, *Nanostructured carbon–metal oxide composite electrodes for supercapacitors: a review*, Nanoscale **5**, 72–88 (2013).

[13] P. Yang, Y. Wu, and R. Fan, *Inorganic semiconductor nanowires*, Inter. J. Nanoscience **1**, 1 (2002).

[14] T. J. Trentler, K. M. Hickman, S. C. Geol, A. M. Viano, P. C. Gibbons and W. E. Buhro, *Solution-liquid-solid growth of crystalline III-V semiconductors: an analogy to vapor-liquid-solid growth*, Science **270**, 1791 (1995).

[15] S. Kathirvel, C. Su, H.-C. Lin, B.-R. Chen and W.-R. Li, *Facile non-hydrolytic solvothermal synthesis of one dimensional TiO_2 nanorods for efficient dye-sensitized solar cells*, Materials Letters **129**, 149–152 (2014).

[16] F. Deng, L. Yu, M. Sun, T. Lin, G. Cheng, B. Lan and F. Ye, *Controllable Growth of Hierarchical $NiCo_2O_4$ Nanowires and Nanosheets on Carbon Fiber Paper and their Morphology-Dependent Pseudocapacitive Performances*, Electrochimica Acta **133**, 382–390 (2014).

[17] Y.-P. Zhao, D.-X. Ye, G.-C. Wang, and T.-M. Lu, *Sculpture aligned nano-column arrays and nano-flowers by glancing angle deposition*, Nano Letters **2**, 351 (2002).

[18] M. Malac and R. F. Egerton, *Observations of the microscopic growth mechanism of pillars and helices formed by glancing-angle thin-film deposition*, J. Vac. Sci. Technol. **A19**, 158 (2001).

[19] Z. Li, Y. Zhu, Q. Zhou, J. Ni, and Z. Zhang, *Photocatalytic properties of TiO2 thin films obtained by glancing angle deposition*, Applied Surface Science **258**, 2766-2770 (2012).

[20] S. Sarkar and S. K. Pradhan, *Tailoring of optical and wetting properties of sputter deposited silica thin films by glancing angle deposition*, Applied Surface Science **290**, 509-513 (2014).

[21] R. Messier, T. Gehrke, C. Frankel, V. C. Venugopal, W. Otaño, and A. Lakhtakia, *Engineered sculptured nematic thin films*, J. Vac. Sci. Technol. **A15**, 2148 (1997).

[22] K. Robbie and M. J. Brett, *Sculptured thin films and glancing angle deposition: growth mechanisms and applications*, J. Vac. Sci. Technol. **A15**, 1460 (1997).

[23] K. Keem, J. Kang, C. Yoon, D. Yeom, D.-Y. Jeong, B.-M. Moon and S. Kim, *A fabrication technique for top-gate ZnO nanowire field-effect transistors by a photolithography process*, Microelectronic Engineering **84**, 1622-1626 (2007).

[24] S. Okazaki, *High resolution optical lithography or high throughput electron beam lithography: The technical struggle from the micro to the nano-fabrication evolution*, Microelectronic Engineering **133**, 23-35 (2015).

[25] Y. Chen, *Nanofabrication by electron beam lithography and its applications: A review*, Microelectronic Engineering **135**, 57-72 (2015).

[26] D. Stamou, C. Musil, W.-P. Ulrich, K. Leufgen, C. Padeste, C. David, J. Gobrecht, C. Duschl and H. Vogel, *Site-Directed Molecular Assembly on Templates Structured with Electron-Beam Lithography*, Langmuir **20**, 3495–3497 (2004).

[27] B. Yan, A. Thubagere, W. R. Premasiri, L. D. Ziegler, L.D. Negro and B. M. Reinhard, *Engineered SERS Substrates with Multiscale Signal Enhancement: Nanoparticle Cluster Arrays*, ACS Nano **3**, 1190-1202 (2009).

[28] Y. Liu, J. Goebla and Y. Yin, *Templated synthesis of nanostructured materials*, Chem. Soc. Rev. **42**, 2610-2653 (2013).

[29] B. B. Lakshmi, C. J. Patrissi and C. R. Martin, *Sol-Gel Template Synthesis of Semiconductor Oxide Micro- and Nanostructures*, Chem. Mater. **9**, 2544–2550 (1997).

[30] O. Azzaroni and K. H. A. Lau, *Layer-by-Layer Assemblies in Nanoporous Templates: Nano-Organized Design and Applications of Soft Nanotechnology*, Soft Matter. **7**(19) 8709–8724 (2011).

[31] A. Walcarius, *Mesoporous materials and electrochemistry*, Chem. Soc. Rev. **42**, 4098-4140 (2013).

[32] N. Taşaltın, S. Öztürk, N. Kılınç¸ H. Yüzer and Z. Öztürk, *Fabrication of vertically aligned Pd nanowire array in AAO template by electrodeposition using neutral electrolyte*, Nanoscale Research Letters **5**, 1137-1143 (2010).

[33] Z. Jindal and N. K. Verma, *Electrochemical template-assisted fabrication of CdS micro/nanostructures*, Physica E: Low-dimensional Systems and Nanostructures **41**(10), 1752-1756 (2009).

[34] X. L. Li, K. F. Cai, H. Li, D. H. Yu, X. Wang and H. F. Wang, *Alumina template-assisted electrodeposition of $Bi_2Te_{2.7}Se_{0.3}$ nanowire arrays*, Superlattices and Microstructures **47**(6), 710-713 (2010).

[35] G. Song, X. Li, Y. Wang, Z. Peng, Y. Yu and P. Li, *Patterned procedure for template-synthesis and microstructural characterization of copper nanowires*, Materials Characterization **61**(3), 371-375 (2010).

[36] K. D. Alexander, K. Skinner, S. Zhang, H. Wei and R. Lopez, *Tunable SERS in Gold Nanorod Dimers through Strain Control on an Elastomeric Substrate*, Nano Lett. **10**(11), 4488–4493 (2010).

[37] Y. Su, M. Feng, C. Zhang, Z. Yan, H. Liu, J. Tang and H. Du, *Platinum Nanowires: Structural and catalytic evolution upon annealing temperature*, Electrochimica Acta **164**, 182-186 (2015).

[38] Q. Zhang, E. Uchaker, S. L. Candelaria and G. Cao, *Nanomaterials for energy conversion and storage*, Chem. Soc. Rev. **42**, 3127-3171 (2013).

2 Theory

This chapter discusses some of the basic theoretical concepts related to this dissertation. It includes electrodeposition, template aided nanomaterials synthesis, size and morphology effect on properties and characterization techniques used in this work. These all are well known in literature, therefore, here we discuss them briefly. For first section, "Electrodeposition" of this chapter most of the material has been referenced from books [1,2].

2.1 Electrodeposition

2.1.1 Introduction

Electrodeposition is a process in which a metal is coated or deposited electrochemically on to an electrically conductive substrate by reduction of metal ions from an electrolyte. The electrolytes are usually conductive aqueous solution of chemical species containing metal to be deposited. Although there are other electrolytes like molten salts and some organic solvents instead of water for electrodeposition, this work is concerned only with aqueous electrolytes.

The electrodeposition process is carried out by immersing the working electrode (work piece on which metal is to be deposited) into the electrolyte containing counter electrode which is externally electrically connected to working electrode with a power supply to provide a constan

current to the circuit. The working electrode is connected to negative terminal so that positive metal ions in the solution can reduce here after accepting electrons. If a constant current is supplied to reduce the metal ions as described in the above case then the process is called galvanostatic. However, electrodeposition carried out at constant potential is called potentiostatic and usually requires a third electrode (reference electrode) which has stable and well known potential to precisely control the potential on the working electrode. In a steady state electrode reaction the potential and current density have one to one correspondence but in an actual reaction where deposition is taking place, it is not stationary.

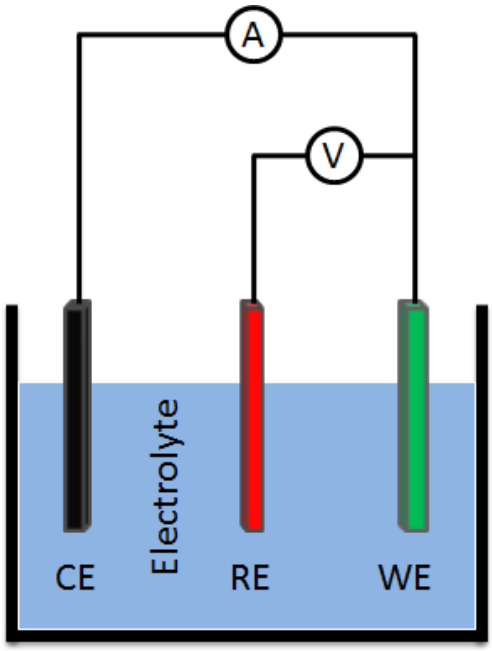

Figure 2.1: Schematic of three electrode setup of an electrochemical cell. CE, RE and WE represent counter, reference and working electrodes respectively. RE controls the potential on the WE in a potentiostatic electrodeposition.

For example in a potentiostatic deposition the current is changing over time and in a galvanostatic deposition the potential is changing over time. These changes are significant at initial stages of the electrodeposition and at least two factors are considered for this behavior.

First is the surface state of the electrode is changing in terms of morphology and roughness with the time as the electrodeposition progress and second the change in solution pH and concentration near the electrode surface during deposition process. In this work potentiostatic electrodeposition method was employed and electrochemical cell depicting a typical three electrode setup is schematically shown in Figure 2.1.

Electrodeposition of Cu metal from $CuSO_4$ solution is a simple example. The solution contains positively charged Cu^{2+} and negatively charged SO_4^{2-} ions. The Cu^{2+} ions migrate to the cathode under the influence of external electric field and discharge as metallic Cu. The reactions at cathode and anode can be expressed by following equations.

At Cathode:

$$Cu^{2+} + 2e^- \rightarrow Cu \tag{2.1.1}$$

At Anode:

If Cu metal is used as anode it is discharged to keep the electrical neutrality.

$$Cu \rightarrow Cu^{2+} + 2e^- \tag{2.1.2}$$

If some noble metal like platinum is used as anode the water oxidation takes place.

$$2H_2O \rightarrow 4H^+ + O_2 + 4e^- \tag{2.1.3}$$

The actual electrodeposition is rather complicated process. By applying potential the rearrangements of ions near the cathode surface takes place resulting in the formation of a double layer followed by the diffusion layer. The hydrated metal ions are migrated to cathode surface under the influence of applied current through diffusion layer where its water molecules are aligned. Then hydrated metal ions enter into double layer where it is deprived of the water molecules and finally reduce by accepting electrons from cathode.

2.1.2 Fundamental equations and concepts

2.1.2.1 Faraday's Law

Faraday's Law defines the relationship between electricity passed through the electrochemical cell and mass of the electrodeposited specie. It states that the amount of electrochemical reaction is directly proportional to quantity of charge passed through the electrochemical cell and can be calculated from the following expression when metal deposition is the only reaction.

$$m = \frac{AQ}{nF} \tag{2.1.4}$$

Where m is the mass of metal deposited (grams), Q the quantity of charge passed in circuit (Coulombs), A the atomic weight of the metal, n the number of electrons transferred per atom and F the Faraday's constant (96485 C mol^{-1}).

When current i is constant, $Q = it$ and when i is not constant, $Q = \int idt$, where t is the time of deposition.

Thus for constant current density equation 2.1.4 can be written as:

$$m = \frac{Ait}{nF} \tag{2.1.5}$$

It is very important relationship as it gives controlled deposition of metal mass through controlling the deposition current and time or in other way mass of deposited metal can be determined by calculating quantity and time of electricity passed through the circuit as was done for Pt, Pd and Ni in this work. The relationship is true only when there is no electrochemical side reaction taking place, for example hydrogen liberation at cathode.

2.1.2.2 Cottrell equation

In galvanostatic electrodeposition the quantity of mass deposited is controlled by two parameters

that is constant current and time of electrodeposition (equation 2.1.5). However, current is changing with the time during potentiostatic electrodeposition as mentioned in section 2.1.1, "Introduction". Therefore, it is very important to predict the changes in current to estimate or control the mass deposited during potentiostatic electrodeposition. Cottrell equation determines the changes in current with the time when a large overpotential is applied in an electrochemical cell (equation 2.1.6). This equation is valid only when deposition process is diffusion controlled and overpotential should be high enough to immediately reduce the ions reaching to the surface of the electrode.

$$i = \frac{nFAD^{1/2}c_b}{\pi^{1/2}t^{1/2}} \tag{2.1.6}$$

where i is the current, n the number of electrons transferred per ion discharge, F the Faraday's constant, A the surface area of the electrode, D the diffusion coefficient of depositing ions, c_b the bulk concentration of the depositing ions in the solution and t the time. This equation not only predicts the current during deposition but also allows calculating the diffusion coefficient D. A similar inverse relationship of current i and time $t^{1/2}$ is observed during nanostructure synthesis in this work which depicts the diffusion limited electrodeposition.

2.2 Electrochemical synthesis of nanomaterials by AAO template

There are two types of templates available commercially, track etched polycarbonate (PC) membrane and anodic aluminum oxide (AAO) membrane. The pore channels in these membranes are aligned almost parallel to each other and perpendicular to the surface of the membrane without pore interconnections. The AAO membrane is prepared from Al metal sheet by electrochemical method and usually has high density of pores (about 10^9 to 10^{11} cm^{-2}), while PC template is prepared by track etch method that is, non-porous material is bombarded with ions to carve damage and then porous structure is obtained by subsequent chemical etching.

The pore density in this method is relatively lesser (6 x 10^8 cm^{-2}), and pores are usually randomly distributed. From high density of pores in AAO membrane, higher surface area is expected from NSs grown by AAO template as compared to PC template. Thus, in our work we employed AAO template assisted electrochemical method to fabricate hierarchical and supported NSs nanostructures. An example of AAO template is shown in Figure 2.2.

In this type of synthesis, one side of the template is made conductive by attaching a metal to the surface of the membrane typically by sputtering or evaporation and is used as working electrode. Metal nanostructures are subsequently deposited by filling the porous template with an electrolytic solution of the metal to be reduced [3-8]. After getting the desired length of the nanostructures by electrodeposition the template is placed on a supporting substrate (in our case SiO_2 or steel) with the help of double sided non-conductive adhesive tape. Further, to expose the NSs the template is removed by immersing it in NaOH solution. For example, the process steps for preparing Pt metal NSs are schematically outlined in Figure. 2.3.

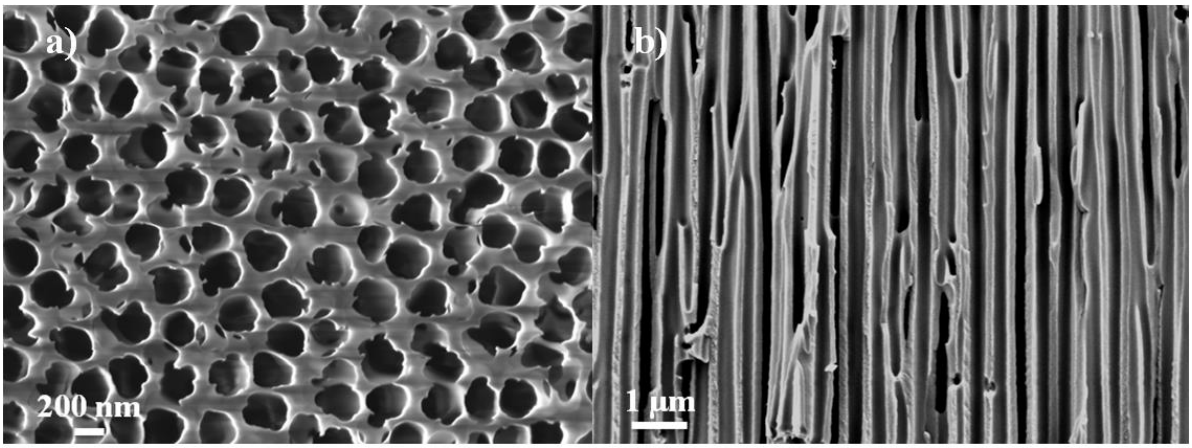

Figure 2.2: SEM image of top a) and cross sectional b) view of commercial AAO template.

The morphology and structure of the NSs grown by template aided electrodeposition technique is usually controlled by deposition conditions such as potential, pH value, additives and temperature [3,8-10]. However, in this work morphology is controlled by the time of

electrodeposition alone or together with annealing conditions such as annealing time and temperature while keeping the other deposition parameters constant. The fact that nucleation first starts at the pore walls of AAO template where conductive surface (sputtered Au) is available helped us manipulating the idea that if we stop electrodeposition at a judicious time, we can get a range of morphologies: thin wall NTs, thick wall NTs and NRs as shown schematically in Figure 2.4. Similarly multiwall NTs can be prepared by electrodepositing the second material inside the

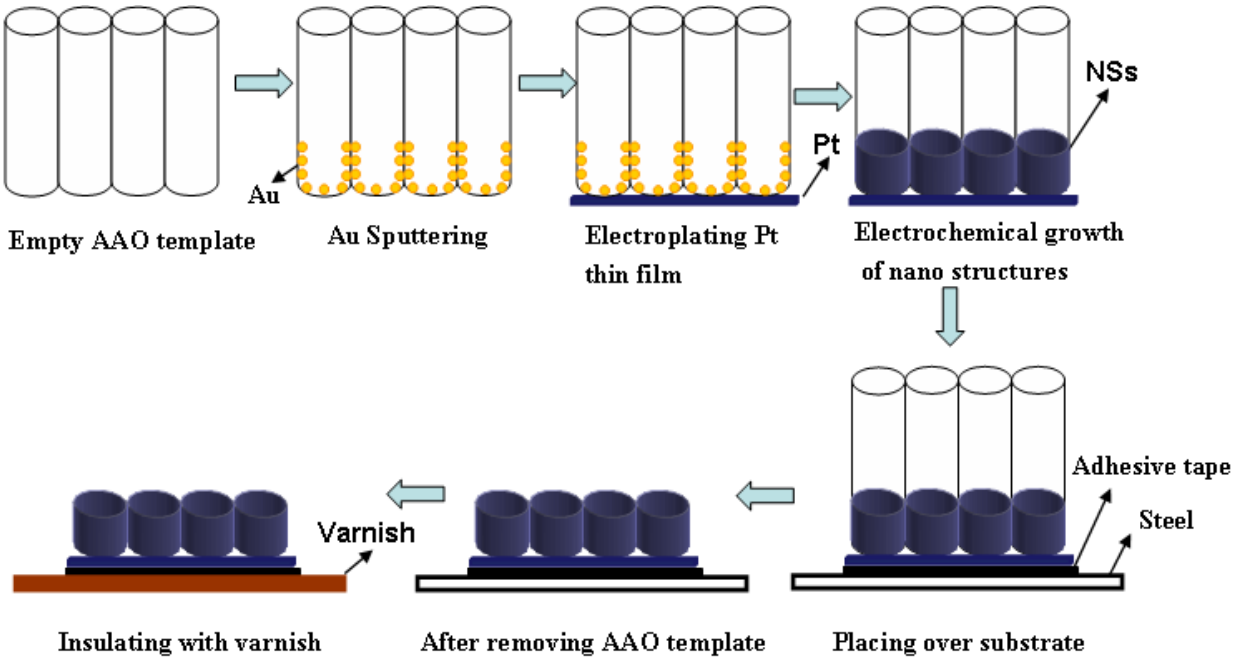

Figure 2.3: Schematic illustration shows the sequential preparation of Pt metal nanostructures. In order to have self-standing NSs, a Pt thin layer is electrodeposited on Au sputtered side of AAO template. In the last step an insulated varnish is applied on the substrate and on the areas other than NSs to utilize it as an electrode for electrochemical reaction. A similar approach is applied for all the nanostructures prepared in this dissertation [11] – Reproduced by permission of The Royal Society of Chemistry.

already prepared NTs and further third material can be electrodeposited inside the walls of the second material and so on. The AAO templates must not be removed when preparing multiwall NTs from single wall NTs to avoid the electrodeposition on the outside walls of the NTs.

Moreover, the idea can be further manipulated to prepare oxide nanostructures with controlled morphology through controlled annealing conditions. It can be achieved by first preparing the thin wall NTs by a suitable time of electrodeposition as mentioned above and then annealing the NTs to oxidize them. The annealing temperature and time of annealing are so selected to grow a desired thickness of the oxide layer on the inside walls of the NTs. To avoid the outside wall growth by oxidation, NTs must be annealed inside the AAO template. It means the AAO template must not be removed before annealing. Thus by judicious combination of annealing temperature and annealing time the morphology of NTs can be controlled from thin walls to thick walls and completely closed NRs (Figure 2.4).

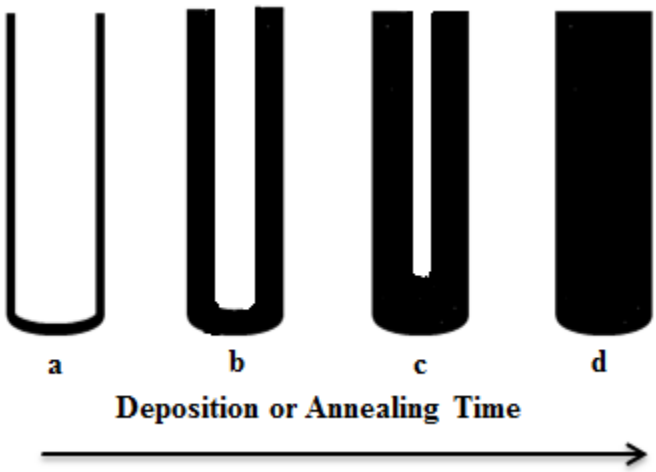

Figure 2.4: The wall thickness of NTs (a-c) increases with the electrodeposition or annealing time until NTs are completely closed to give NRs morphology (d).

2.3 Size and morphology effect on properties

Nanomaterials appear in a variety of forms such as nanoparticles, nanorods, nanotubes, nanofibers, nanoflowers, nanoporous films, etc. Their properties are known to be dominated by the structural parameters which include particle size, morphology structure and surface

composition. Thus properties of the nanomaterials can be engineered by controlling and manipulating these parameters. On the other hand, introduction of the second element on the surface of the nanomaterials modify their surface properties such as electrocatalysis by triggering bifunctional mechanism and ligand effect (explained in Chapter 5) [12-14]. Moreover, second element also influences the crystal structure and particle size if present during crystal growth [13].

By reducing the size of the materials, the percentage of the atoms on the surface relative to the bulk and the surface-to-volume ratio increase dramatically. For example, a particle with a size of 100 nm has less than 0.2% of atoms on the surface, 10 nm particle has 10% surface atoms and for 2 nm particle around 90% of the atoms are essentially on the surface [15]. The improved properties of small nanoscale materials can be explained by considering higher number of atoms taking part for example in a certain electrochemical reaction, as compared to larger particles with less number of atoms on the surface. Moreover, atoms on the surface may also have one or more dangling bonds which tend to reduce their energy by reacting or forming bonds with adjacent molecules and get stabilized. Thus increased reactivity of the surface atoms results in advantageous properties such as an increased chemical activity, lowered melting point, and higher solubility as compared to their bulk counterparts [16].

The morphology and structure is also an important parameter which plays an important role in defining the functional properties of the nanomaterials [17-19]. For example the capacitive performance of hematite, α-Fe_2O_3 nanotubes is much better than nanorods. The superior behavior can be assigned to the tubular morphology which tolerates the huge volume changes during charge-discharge cycles and the large surface area as compared to nanorods [20]. To argue structural effect, desorption of hydrogen by Pt from a sulphuric acid solution is an example, where (111) Pt surface is responsible for hydrogen desorption at higher potential as compared to (110) Pt surface at lower potential [21]. This behavior can be attributed to the different electronic and atomic arrangement of different Pt surfaces which leads to the different reactivity for the same reaction [22]

The surface composition also plays an important role in deciding the functional properties of the nanomaterials. As an example we know that addition of Ru to the Pt surface in the form of alloy

or bimetallic improves the electrochemical properties of Pt [23]. For instance the electrooxidation of methanol occurs more efficiently on Pt/Ru surface as compared to bare Pt. The addition of the Ru atoms to the surface of Pt triggers the bifunctional mechanism, that is, Ru helps in absorbing oxygen containing species to be oxidized by Pt.

2.4 Characterization techniques

2.4.1 Scanning electron microscopy

The scanning electron microscope (SEM) is widely used technique for morphology and structural analysis of the materials. SEM provides much higher resolution than what is possible with the light microscope, and therefore, is an important part of the materials science research laboratories. An electron beam is produced from a cathode and accelerated to a desired energy which is typically 1 to 50 KeV. The available range of the electron beam energy depends on the type of instrument. The electron beam is then focused on to the small area down to 1 nm on specimen with the help of lenses. Further area of interest in the specimen is then scanned by moving it underneath the electron beam. The images of the materials surface are obtained by detecting the electrical signals which arises from the interaction of the incident electron beam and specimen under investigation. There is range of electron-specimen interactions possible which allow the different analytical modes of operation for SEM as follows.

2.4.1.1 Electron solid interaction

When an electron beam is incident on the surface of a solid specimen, the electrons penetrates into the surface and interacts with its atoms as shown schematically in Figure 2.5 [24]. Elastic and inelastic scattering are the two main outcomes of the electron-specimen encounter. Elastic scattering is the one when almost no energy of the incident electrons is lost and electrons merely change their direction even up to an angle of 180°. This phenomenon occurs when incident electrons are back scattered from the nuclei of the specimen atoms. Due to heavy mass of the

nuclei as compared to the electrons no energy transfer takes place and most of the electrons are backscattered. On the other hand the interaction of incident electrons with the electrons of the atomic shells of the specimen is quite different. Here, incident electrons transfer their energy to the electrons of the atomic shells due to equal masses, and the process is called inelastic scattering. After collision incident electrons not only change their direction but also slow down due to lose of energy. The collision of incident electrons with atomic shell electrons can generate secondary electrons, x-rays and /or auger electrons. The secondary electron is emitted from or through the surface when incident electron beam has enough energy to overcome the binding energy of the inner atomic shell electrons with the nucleus. In this case electron is knocked out from its shell leaving a vacancy behind it. Now this ionized atom is at excited state and an electron from an orbit of higher energy level can fill this vacancy by either releasing a characteristic photon or auger electron. The process is repeated until atoms come back to its neutral ground state.

Due to these scattering events the focused electron beam is spread over a droplet shaped volume. The shape and size of this scattering volume depends upon the energy and direction (angle of incident) of the beam and atomic size of the specimen material. The shape and size of this scattering volume can be calculated theoretically with Monte Carlo simulation which also shows that backscattering occurs from a wider area as compared to incident electron beam spot size.

Both the secondary electrons and backscattered electrons signals are used for imaging the specimen in SEM. Both of these signals can also be used together to obtain complementary image.

However, due to different ranges of scattering the secondary electrons are used for surface topography while back scattered electrons are more useful for subsurface information of the specimen. It is important to note that backscattered electrons also create secondary electrons in their whole path within the specimen due to their high energy. The secondary electrons emitted in this way near the surface, that is, within the escape depth, form part of the secondary electron current, however they are not related to surface topography rather weaken the information part of the secondary electrons produced by primary incident electron beam [25].

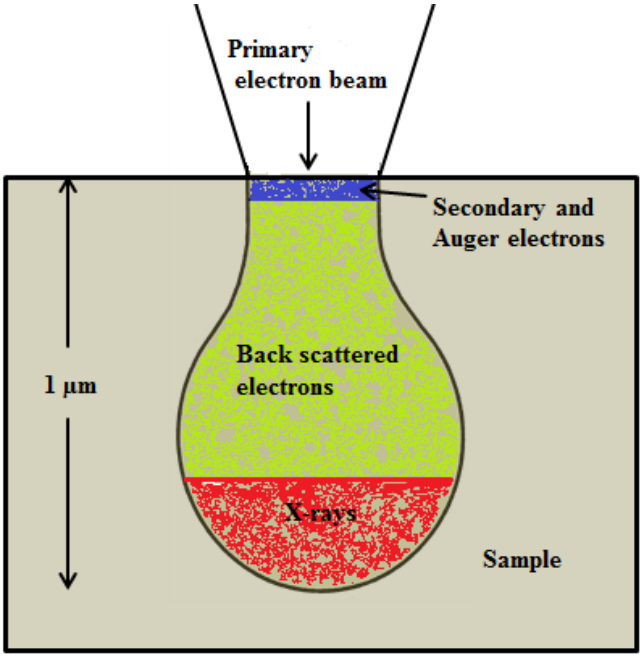

Figure 2.5: Schematic of the interaction between primary electron beam of the SEM and a sample.

Along with backscattered and secondary electrons, some of the electrons are transmitted through the specimen to the ground. According to the Kirchhoff's current law the incident beam electron current i_o is given by the following equation [26].

$$i_o = i_{BSE} + i_{SE} + i_G \tag{2.4.1}$$

where i_{BSE}, i_{SE} and i_G are the back scattered electron current, secondary electron current and transmitted electron current through the specimen to the ground.

2.4.1.2 Electron yield

The back scattered electron yield η and secondary electron yield Δ which refer to back scattered and secondary electrons emitted per incident beam electron i_o can be written as:

$$\eta = \frac{i_{BSE}}{i_o} \tag{2.4.2}$$

$$\Delta = \frac{i_{SE}}{i_o} \tag{2.4.3}$$

With the increase in incident beam current there is a corresponding increase in η and Δ. The total electron yield δ per incident beam electron is:

$$\delta = \eta + \Delta \tag{2.4.4}$$

If δ is drawn as a function of incident beam current energy a characteristics yield curve is obtained as shown in Figure 2.6 [25].

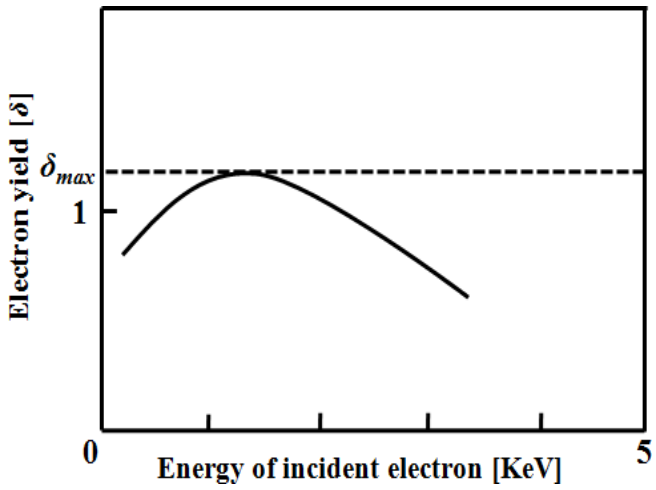

Figure 2.6: A characteristic curve representing the electron yield behavior dependence on the incident electron energy.

Initially δ increases with the incident beam energy, reaches a maximum value and then decline again. There are two opposing factors behind this behavior. With increasing energy of the incident electrons, the number of secondary electrons emitted increases. However, the penetration depth of incident electrons also increases with their increasing energy and after a

certain maximum energy $E_{max,}$ a proportion of secondary electrons generated too far beneath the surface of the specimen too escape from the surface. Therefore, δ decreases after reaching a maximum peak value (δ_{max}). The δ_{max} depends upon material, typical values are less than 2 for pure elements and 10 or more for compounds. The E_{max} which corresponds to δ_{max} also varies for different materials but generally lays around 1 KeV. Thus when higher voltages are used in scanning electron microscopy the δ is well below unity and reducing the voltage and working near E_{max} electron yield can be improved for imaging.

2.4.2 Energy dispersive X-ray spectroscopy

The chemical composition of the specimen under investigation can be determined by energy dispersive X-rays spectroscopy (EDS).

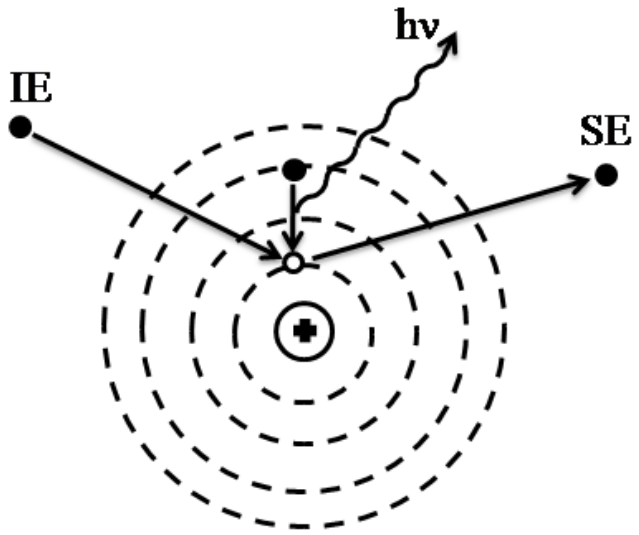

Figure 2.7: Schematic representation of X-rays production by electron solid interaction. Incident electron beam IE knocks out the secondary electron SE leaving behind a vacancy. A transition of electron takes place from higher energy level to fill the vacancy resulting in emission of characteristic X-rays (hv).

This technique utilizes the X-rays which are emitted when a solid specimen is bombarded with incident electron beam which ionizes the atoms by knocking out core shell electrons. To fill this vacancy a transition of electron from higher energy level takes place with the emission of characteristic X-rays (Figure 2.7) as stated in section 2.4.1.1, "Electron Solid Interaction".

The X-rays are characteristic of the elements by their wavelength λ or energy E and both are related with each other as follows:

$$E = \frac{hc}{\lambda} \tag{2.4.5}$$

Where h is Planck's constant and c is the velocity of light.

Because the wavelength or energy of the emitted X-rays depends upon the energy levels of the atom involve, therefore, spectrum of x-rays can be used to identify the elements in the specimen. Furthermore, the percentage composition of individual elements in the specimen can also be determined if intensity of these characteristic X-rays are analyzed. To knock out the electrons from a solid specimen Incident electron beam energy should be higher than binding energy of the core shell electrons. This binding energy between electrons of the core shell and nucleus increases with the increase of atomic number of the elements. Most of the elements have at least one X-rays emission line below 10 KeV and usual ideal incident beam energy is two to three times higher than excitation energy. In this work EDS was employed to identify and confirm the elements in bimetallic and trimetallic NSs. Moreover, successful removal of AAO template was also confirmed by EDS.

2.4.3 X-ray diffraction

X-rays are electromagnetic radiations which have high energies ranging from 100 eV to 10 MeV and are different from radio waves, light and gamma rays in their wavelength and energy. Each electromagnetic radiation or photon has energy proportional to its wavelength (equation 2.4.5). The inter atomic distance in crystals is typically about 0.2 nm thus useful wavelength range of X-rays diffraction analysis is 0.05 to 0.25 nm.

The X-rays are produced in X-ray tube where high voltage (several tens of KV) is applied between two electrodes and electrons with sufficient kinetic energy from the electron source electrode (cathode) come out and strike the target electrode (anode). The electrons slow down and scatter in all directions after collision with anode. The loss of kinetic energy of electrons appears in the form of continuous X-rays because losses of kinetic energy patterns vary with electrons scattering event. However most of the kinetic energy of the electrons is lost in producing heat after striking the anode and only less than 1 % turns into X-rays.

On the other hand when electrons have enough energy to knock out, for example inner K shell electrons of the target anode an electron vacancy is created in the K shell and neutral atom is excited. To regain its stable state an electron transition from outer shell (higher energy level) takes place, as explained in section 2.4.2, "Energy Dispersive X-ray spectroscopy". In this case characteristic X-rays having energy equal to the difference in electron energy levels of the transition shells are emitted. These characteristic X-rays are used for X-ray diffraction analysis.

Bragg demonstrated that X-rays show characteristic patterns after reflecting from crystalline materials. Schematic Figure 2.8 explains the Bragg reflection from two consecutive planes of a crystalline material. He formulated the conditions for this characteristic diffraction which is now called Bragg's Law.

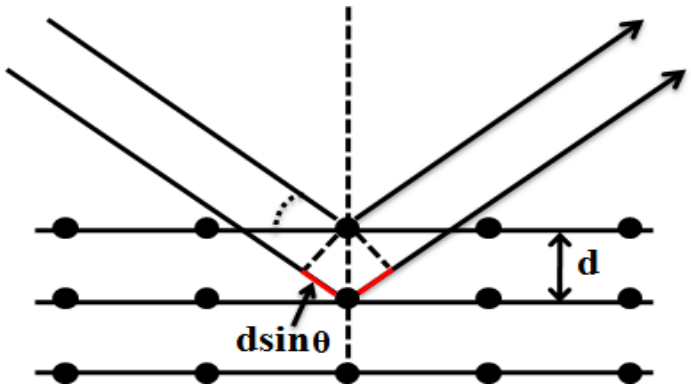

Figure 2.8: A schematic representation of Bragg's Law. Two X-ray diffracting from two consecutive planes of a crystalline material with an interatomic distance d.

$$n\lambda = 2d\sin\theta \qquad (2.4.6)$$

Where θ is the angle of incidence, d the inter planner distance, λ the wavelength of X-ray and n is the integer which is the order of reflection.

Because the diffraction pattern rely on inter planer distance d, individual crystalline materials in the specimen can be identified. Moreover, orientation and stresses in the crystals can also be determined by calculating the intensity and width of the diffracted X-rays signals respectively. In this work XRD was employed to identify the individual crystalline materials and their crystal structures.

2.4.4 Cyclic voltammetry

Cyclic voltammetry is an electrochemical technique to examine the preliminary mechanism of the electrochemical reactions. The technique involves sweeping the potential of the working electrode (WE) from a starting potential V_1 to a final potential V_2 at a known scan rate and measuring the resulting current. The V_2 is also called switching potential because after reaching V_2 sweep direction is reversed. When the potential of the WE is changed during potential sweep or scan, two different types of currents can arise: faradic current and capacitive current. Faradic current is related to oxidation and reduction reactions. Capacitive current arises when charge density at the electrode / electrolyte interface is changed due to the changing potential at the electrode. [27] The capacitive current is often called background current to the reaction of interest. The scan rate must be carefully selected to investigate for example oxidation or reduction reactions because at high scan rate capacitive current is also high and can overlap with faradic current of oxidation or reduction [27]. Cyclic Voltammetry has various applications such as studying the oxidation and reduction reactions, for example in this work oxidation of methanol and formic acid is examined, to study qualitative information such as presence of intermediates in oxidation-reduction reactions, the reversibility of a reaction. The real surface area of the electrodes can also be determined from hydrogen adsorption / desorption region in

cyclic voltammogram (CV), if charge density for monolayer of hydrogen adsorption on a specific surface is known. For example in this work real surface areas of Pt-NR electrodes were determined by performing a Cyclic Voltammetry (Figure 2.9) in an acidic media (0.5M H_2SO_4). It is achieved by dividing the integrated area of the hydrogen adsorption / desorption region in

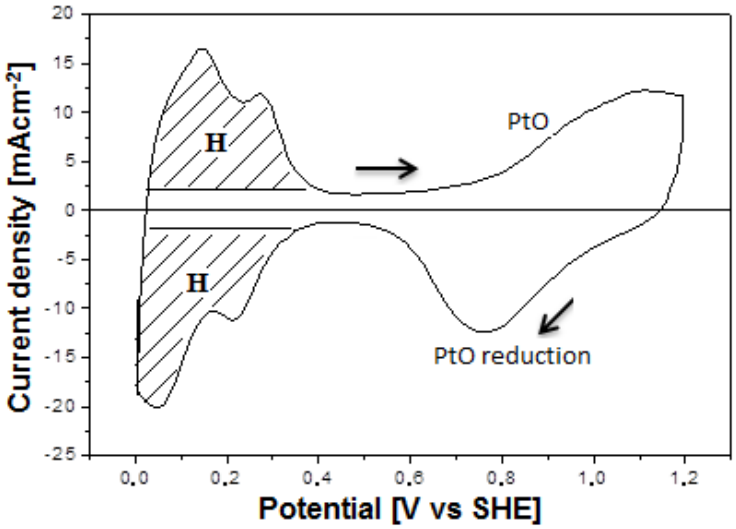

Figure 2.9: CV performed on a Pt-NR electrode in a 0.5M H_2SO_4 solution. The arrows pointing towards right and left represent forward and backward scan direction respectively. The start of Pt oxidation and reduction peak potentials is also shown. The shaded areas represent the H adsorption and desorption regions in backward and forward scans respectively. The area below the shaded area in forward scan represents the capacitive or background current which can also be observed in backward scan.

the CV with known value of charge density of monolayer hydrogen adsorption (210 µC cm^{-2}) on polycrystalline Pt surfaces [28].

2.4.5 Charge-discharge Test

Charging-discharging test is also an electrochemical technique to determine a number of properties such as capacitance and long term stability or cycle life of the capacitors. Charge

discharge tests are performed at constant current and in an appropriate potential window as an exemplary shown in Figure 2.10. However, for unknown systems CV is performed first to find out the potential range to avoid the damage to the capacitor electrode or electrolyte. After performing charge-discharge test at constant current the specific capacitance of the NiO can be calculated from the following expression:

$$C = \frac{I.t}{V.m} \tag{2.4.7}$$

where, C is the specific capacitance (Fg^{-1}), I the current (A), t the discharge time (s), V the potential window (V) and m the mass of the NiO (g).

The long term stability and capacity retention can be determined by performing the charge-discharge tests for considerably higher number of cycles as required or according to expected cycle life of the capacitor. It is done by calculating the capacity after certain number of cycles of charging and discharging and plotting it against the cycle number (see chapter 6).

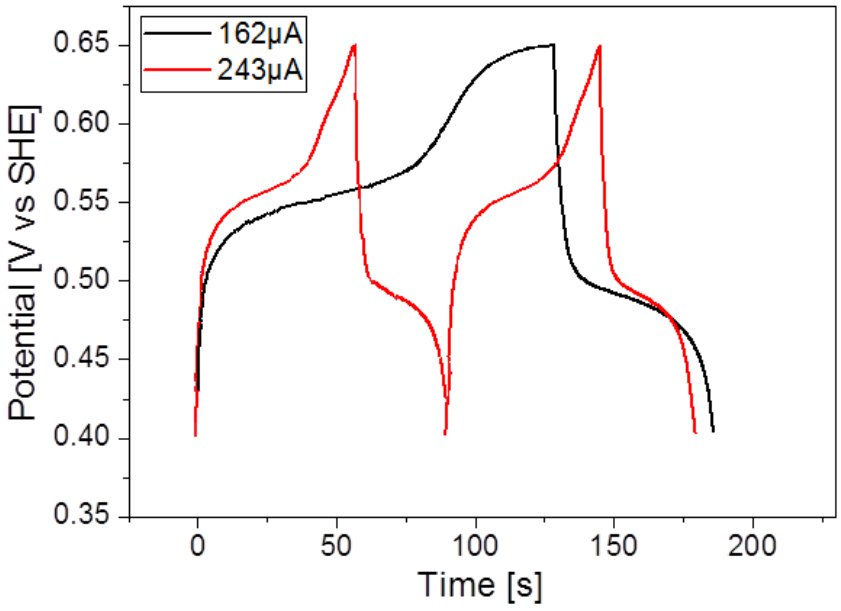

Figure 2.10: Charge-discharge tests performed on NiO-NTs electrode at constant current and in a potential window of 0.40 V to 0.65 V. The longer charging and discharging time can be noted for smaller current (162 μA) as compared to higher current (243 μA).

References

[1] Y. D. Gamburg and G. Zangari, *Theory and Practice of Metal Electrodeposition*, Springer, New York (2011).

[2] Cynthia G. Zoski, *Handbook of Electrochemistry*, Elsevier, Amsterdam (2007).

[3] J. G. Wang, M. L. Tian, N. Kumar and T. E. Mallouk, *Controllable Template Synthesis of Superconducting Zn Nanowires with Different Microstructures by Electrochemical Deposition*, Nano Lett. **5**(7), 1247–1253 (2005).

[4] G. Kartopu, S. Habouti and M. Es-Souni, *Synthesis of palladium nanowire arrays with controlled diameter and length*, Materials Chemistry and Physics **107**, 226–230 (2008).

[5] S. Habouti, M. Mátéfi-Tempfli, C. H. Solterbeck, M. Es-Souni, S. Mátéfi-Tempfli and M. Es-Souni, *On-substrate, self-standing Au-nanorod arrays showing morphology controlled properties*, Nano Today **6**, 12– 19 (2011).

[6] S. Habouti, M. Mátéfi-Tempfli, C. H. Solterbeck, M. Es-Souni, S. Mátéfi-Tempfli and M. Es-Souni, *Self-standing corrugated Ag and Au-nanorods for plasmonic applications*, J. Mater. Chem. **21**(17), 6269–6273 (2011).

[7] G. D. Sulka, A. Brzózka and L. Liu, *Fabrication of diameter-modulated and ultrathin porous nanowires in anodic aluminum oxide templates*, Electrochimica Acta **56**, 4972–4979 (2011).

[8] C. R. Martin, *Nanomaterials - A Membrane-Based Synthetic Approach*, Science **266**, 1961–1966 (1994).

[9] C. R. Martin, *Membrane-Based Synthesis of Nanomaterials*, Chem. Mater. **8**, 1739–1746 (1996).

[10] A. Huczko, *Template-based synthesis of nanomaterials*, Appl. Phys. A **70**, 365–376 (2000).

[11] F. I. Dar, S. Habouti, R. Minch, M. Dietze and M. Es-Souni, *Morphology control of 1D noble metal nano/heterostructures towards multi-functionality*, J. Mater. Chem. **22**, 8671–8679 (2012).

[12] S. Alayoglu and B. Eichhorn, *Rh−Pt Bimetallic Catalysts: Synthesis, Characterization, and Catalysis of Core−Shell, Alloy, and Monometallic Nanoparticles*, J. Am. Chem. Soc. **130**, 17479–17486 (2008).

[13] T-Y. Chen, Y-T. Liu, H-S. Chen, K-W. Wang, C-T. Yang, T-J. M. Luo, C-H. Lee and T-L. Lin, *Crystal growth of platinum–ruthenium bimetallic nanocrystallites and their methanol electrooxidation activity*, CrystEngComm. **15**, 3932–3942 (2013).

[14] J. C. Davies, J. Bonde, Á. Logadóttir, J. K. Nørskov and I. Chorkendorff, *The Ligand Effect: CO Desorption from Pt/Ru Catalysts*, Fuel Cells **5**(4), 429–435 (2005).

[15] C. Burda, X. Chen, R. Narayanan and M. A. El-Sayed, *Chemistry and Properties of Nanocrystals of Different Shapes*, Chem. Rev. **105**(4), 1025–1102 (2005).

[16] A. P. Alivisatos, *Perspectives on the Physical Chemistry of Semiconductor Nanocrystals*, J. Phys. Chem. **100**(31), 13226–13239 (1996).

[17] Z. Peng and H. Yang, *Designer platinum nanoparticles: Control of shape, composition in alloy, nanostructure and electrocatalytic property*, Nano Today **4**, 143–164 (2009).

[18] J. Solla-Gullón, F. J. Vidal-Iglesias and J. M. Feliu, *Shape dependent electrocatalysis*, Annu. Rep. Prog. Chem., Sect. C **107**, 263–297 (2011).

[19] T-D. Nguyen, *From formation mechanisms to synthetic methods toward shape-controlled oxide nanoparticles*, Nanoscale **5**, 9455–9482 (2013).

[20] L. Chen, H. Xu, L. Li, F. Wu, J. Yang and Y. Qian, *A comparative study of lithium-storage performances of hematite:Nanotubes versus nanorods*, Journal of Power Sources **245**, 429–435 (2014).

[21] N. Markovic, H. Gasteiger and P. N. Ross, *Kinetics of Oxygen Reduction on Pt(hkl) Electrodes: Implications for the Crystallite Size Effect with Supported Pt Electrocatalysts*, J. Electrochem. Soc. **144**, 1591–1597 (1997).

[22] V. R. Stamenkovic, B. Fowler, B. S. Mun, G. Wang, P. N. Ross, C.A. Lucas and N. M. Marković, *Improved oxygen reduction activity on Pt3Ni(111) via increased surface site availability*, Science **315**, 493–497 (2007).

[23] B. Habibi, M. H. Pournaghi-Azar, H. Abdolmohammad-Zadeh, H. Razmi, *Electrocatalytic oxidation of methanol on mono and bimetallic composite films: Pt and Pt–M (M = Ru, Ir and Sn) nano- particles in poly(o-aminophenol)*, International Journal of Hydrogen Energy **34**, 2882–2892 (2009).

[24] T. Peter, *Gas phase cluster aggregation and its application to the deposition of functional thin films*, doc. Thesis, Faculty of Engineering, Christian-Albrechts University of Kiel, (2013).

[25] Ian M. Watt, *The principles and practice of electron microscopy*, second edition, Cambridge University press, Cambridge (1997).

[26] C. R. Brundle, C. A. Evans and Jr. S. Wilson., *Encyclopedia of Materials Characterization*, Manning Publications Co., Greenwich (1992).

[27] C. H. Hamman, A. Hamnet and W. Vielstich, *Electrochemistry*, 2nd ed., Wiley-VCH, Weinheim (2007)

[28] T. Biegler, D. A. J. Rand and R. Woods, *Limiting oxygen coverage on platinized Platinum; relevance to determination of real platinum area by hydrogen adsorption*, J. Electroanal. Chem. **29**, 269 (1971).

3 Morphology Controlled Synthesis of Noble Metal Nanostructures

This chapter is mainly based on our paper [1] and describes the template aided electrochemical synthesis of noble metal nanostructures (NSs) with controlled morphology. Along with the mono-metallic NSs synthesis of Pt, Au and Pd, we also investigated if our approach could be extended to multi-metallic NSs. In this connection we successfully electrodeposited monometallic, bimetallic and trimetallic nanotubes inside the AAO template. As mentioned in the previous chapter (Theory) that the morphology and structure of the NSs grown by this technique is usually controlled by deposition conditions such as potential, pH value, additives and temperature, here in this chapter we demonstrate the morphology control of the NSs by controlling time of electrodeposition while keeping other deposition parameters constant.

3.1 Materials and methods

All the aqueous electrolytes used in this work were prepared from deionized water (≥ 18MΩ) and chemicals of analytical grade purity. The electrodeposition was conducted by electrochemical workstation, (ZAHNER IM6e, Germany). All the electrochemical experiments were executed at room temperature in a standard three electrode cell. A Ag/AgCl (saturated KCl) was used as reference electrode and Pt mesh as counter electrode while Au sputtered AAO

template was the working electrode. All the prepared electrolytes were saturated with nitrogen (N_2) before each electrochemical experiment. All the potentials in this work are referred to standard hydrogen electrode (SHE).

The microstructure, morphology and chemical composition of the NSs were examined with a high resolution scanning electron microscope (Ultra Plus, Zeiss, Germany). X-ray diffraction data was obtained on an X'pert Pro system (PANalytical, Holland) using monochromatic Cu Kα radiation (λ = 1.5418 Å).

3.2 Synthesis of nanostructures

The general process steps for preparing the NSs are schematically outlined in chapter 2 (Theory), Figure 2.3, and described below with necessary changes for all NSs.

3.2.1 Substrate preparation

The commercial (Whatman International) non-conductive AAO template with 200 nm pore size and 60 µm thickness is the sacrificial substrate to prepare nanostructures in this work. For electrodeposition of nanostructures, it is made conductive by sputtering a thin layer of 20 nm gold on its back side. The AAO template is handled with care because of its very brittle nature; a polymer ring attached across the commercial template is used for this purpose. Moreover, the AAO template is kept in clean glassware after the gold sputtering to avoid dust particles. A thin copper wire is attached to the Au sputtered side of the AAO template with silver (Ag) paste for electrical connection.

3.2.2 Synthesis of monometallic Pt, Au and Pd nanostructures

At first, a thin Pt support layer is electrodeposited by exposing the Au sputtered side of the AAO

template to the electrolyte containing 50 mM H_2PtCl_6. The metal support layer is required in order to synthesize the self-standing nanostructures and Pt support layer is electrodeposited for Pt and Au NSs samples only. It closed the Au sputtered side of the AAO template completely. Then Pt and Au NSs are grown electrochemically via bottom up approach from their respective electrolytes (50 mM H_2PtCl_6 and 50 mM $HAuCl_4.3H_2O$) under potentiostatic conditions at -0.1 V and 0.3 V for Pt and Au respectively. NTs of increasing wall thickness were reproducibly obtained by varying the deposition time, eventually until closure of the NTs and formation of NRs. The equations for reduction of $[PtCl_6]^{2-}$ and $[AuCl_4]^-$ complexes to Pt and Au respectively, are given below. The standard potentials for these reduction reactions are +0.74 V and +1.0 V for Pt and Au respectively.

$$\left[PtCl_6\right]^{2-} + 4e^- \rightarrow Pt + 6Cl^- \tag{3.2.1}$$

$$\left[AuCl_4\right]^- + 3e^- \rightarrow Au + 4Cl^- \tag{3.2.2}$$

The procedure for Pd nanostructures processing is similar to Pt and Au nanostructures except that Pd is electrodeposited as support layer in place of Pt. It is because, in this work, Pd nanotubes electrode is further analyzed for formic acid oxidation reaction and Pt is also active metal to formic acid oxidation. Thus to avoid any contribution in the oxidation reaction from Pt, its use as supporting layer is avoided. The Pd NTs are grown from electrolyte containing 70 mM K_2PdCl_4 + 20 mM H_2SO_4 at –0.2 V. The reduction equation of the complex $[PdCl_4]^{-2}$ to Pd can be written as follows. The standard potential of this reaction is +0.6 V.

$$\left[PdCl_4\right]^{2-} + 2e^- \rightarrow Pd + 4Cl^- \tag{3.2.3}$$

The reduction equations of Pt and Pd were further utilized in chapter 4 (Electrocatalysis of Pt and Pd nanostructures) to calculate the mass deposited by these metals during electrodeposition.

3.2.3 Synthesis of multi-metallic nanotubes

A similar approach is utilized to grow multi-metallic nanostructures inside the AAO template

containing at least one noble metal.

3.2.3.1 Bimetallic Pt-Cu NTs

In case of bimetallic Pt-Cu first of all a thin layer of Pt is deposited on Au sputtered side from an electrolyte containing 50 mM H_2PtCl_6 as stated above for Pt and Au NSs to close the pores, but it also forms Pt-NTs due to the presence of sputtered Au on inside walls of the AAO template. Further Cu is electrodeposited inside the Pt NTs by bottom up approach from an electrolyte containing 0.1 M $CuSO_4$ under potentiostatic conditions at –0.1 V for 60 s.

3.2.3.2 Trimetallic NTs

(1) Pt-Ni-Au

An approach, similar to bimetallic NTs as stated above is adopted. Briefly, Pt is electrodeposited from similar electrolyte (50 mM H_2PtCl_6) on Au sputtered side of AAO template. Electrodeposited Pt not only closed the Au sputtered side but also forms thin tube walls inside the template due to the presence of sputtered Au. Further, first Ni and then Au is electrodeposited by bottom up approach from 100 mM $NiSO_4.7H_2O$ and 50 mM $HAuClO_4.3H_2O$ respectively. The electrodeposition conditions are given in Table 3.1.

(2) Pt-Au-Cu

Here again similar to Pt-Ni-Au NTs, Pt is electrodeposited as support layer and then subsequently Au and Cu are electrodeposited inside the Pt NTs. The electrolytes used for Au and Cu are 50mM $HAuClO_4.3H_2O$ and 100 mM $CuSO_4$ under the potentiostatic deposition conditions given in Table 3.1.

Table 3.1 The deposition conditions for TMNTs are given for each metallic layer [1] – Adapted by permission of The Royal Society of Chemistry.

Nanostructures	Metals	Potential [V vs SHE]	Time of deposition [s]
Pt-Ni-Au TMNTs	Pt	–0.1	600
	Ni	–0.7	160
	Au	+0.3	40
Pt-Au-Cu TMNTs	Pt	–0.1	600
	Au	+0.3	120
	Cu	–0.1	180

To reveal the nanostructures the AAO templates containing nanostructures are first bonded to steel or SiO_2 support with double sided non-conductive adhesive tape and then immersed into 5% NaOH solution for 2 hours to remove the AAO templates for all nanostructures in this work. After template removal the samples are rinsed with distilled water several times and dried in air.

3.3 Structure and morphology

3.3.1 Monometallic nanostructures

The structure and morphology of the electrodeposited nanostructures inside the AAO template is dependent on deposition conditions such as pH value, temperature, potential and additives. However, a judicious concentration of electrolyte had to be found in combination with other parameters of deposition. It allowed us to control the morphology of the nanostructures through the deposition time. For example Figure 3.1 shows that morphology of the Pt NSs is controlled

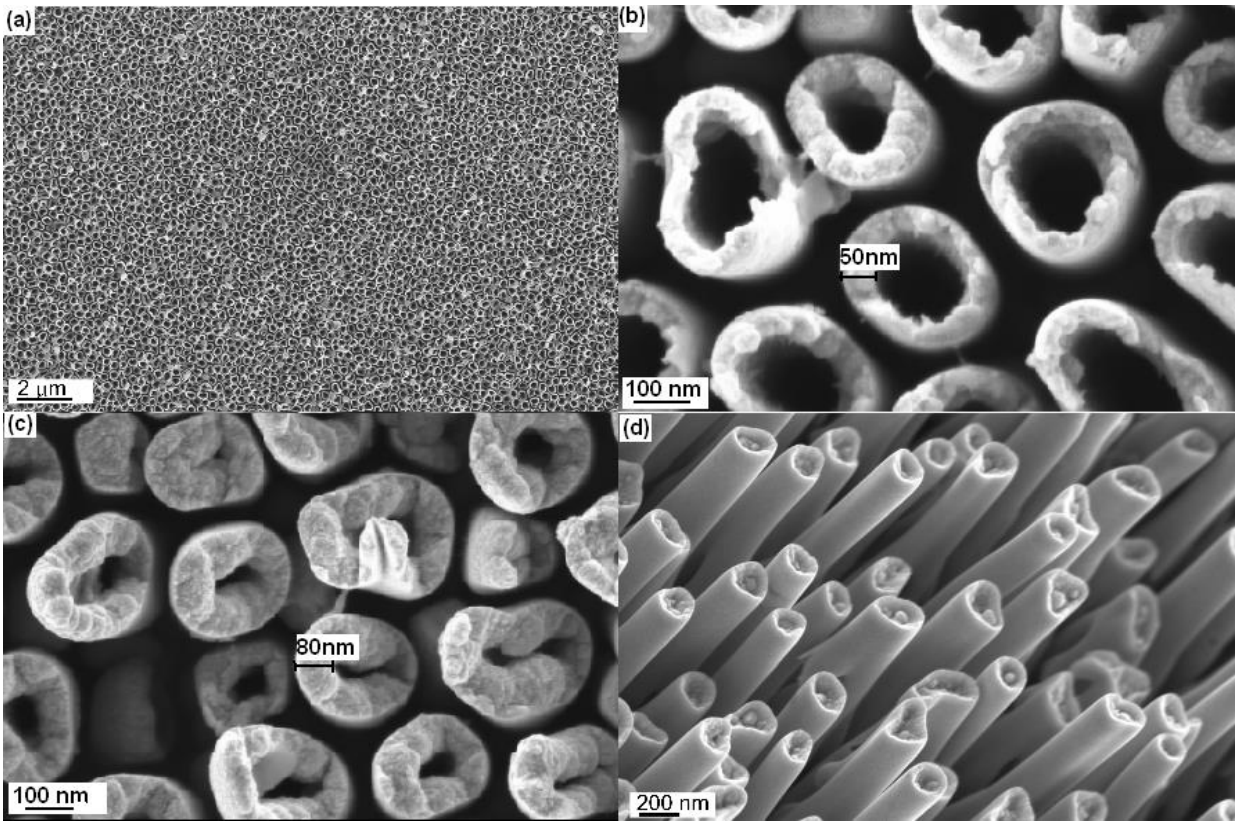

Figure 3.1: Secondary electron (SE) micrographs of 1D-Pt NSs obtained from the same electrolyte concentration and deposition voltage but with increasing deposition times from (a,b) to (d). (a) and (b) are for 100 s ((a) is a low magnification micrograph to show the homogeneous microstructure over a large deposition area); (c) 200 s deposition time showing wall thickening in comparison to (b); (d) 1200 s deposition time showing NRs [1] – Reproduced by permission of The Royal Society of Chemistry.

solely by varying the time of deposition and keeping constant all other deposition conditions including electrolyte concentration. For shorter deposition time (100 s), thin walled Pt-NTs are formed and gradually tube walls are started to thicken for longer deposition time (200 s), further longer time leads to complete filling of tubes and Pt NRs are formed. We try to explain this time dependent morphology control phenomenon with the support of current-time curve (Figure 3.2) recorded during electrodeposition as follows.

As we have sputtered Au on one side (bottom) of the AAO template and due to open pores the Au is penetrated into the pores to a depth of ~ 1 µm and condenses to the pore walls. Therefore,

at first Pt nucleates and grows on free surfaces that is, at the bottom and on the pore walls which results in the formation of Pt NTs in the beginning of the electroplating. The presence of Au probably promotes this fast nucleation and growth on pore walls. Consequently we can deduce that, if we stop deposition at a judicious time upon which the NTs had already acquired enough mechanical stability (to prevent their collapsing), it should be possible to obtain free-standing PT-NTs with tunable wall thickness. This time obviously depends on deposition conditions such as electrolyte and Pt^{4+} concentration, the deposition voltage and the template pore size, and is certainly a complex function of all these conditions. In our case a deposition time of 100s at a constant voltage of -0.1V and an electrolyte concentration of 50 mM did fulfill our requirement on NTs stability. Figure 3.2(a) is nicely informative in this respect where three different zones of deposition current can be identified. The first high current zone corresponds to the formation of NTs by fast kinetics at initial stages of deposition. The second diffusion-limited growth zone shows sharp decrease in current. This decrease in current arises due to the double layer charging which has also been observed for electrodeposition of different metals [2,3], that is $[H_3O]^+$ ions forms a positive layer on negative electrode (Au sputtered AAO template) followed by the

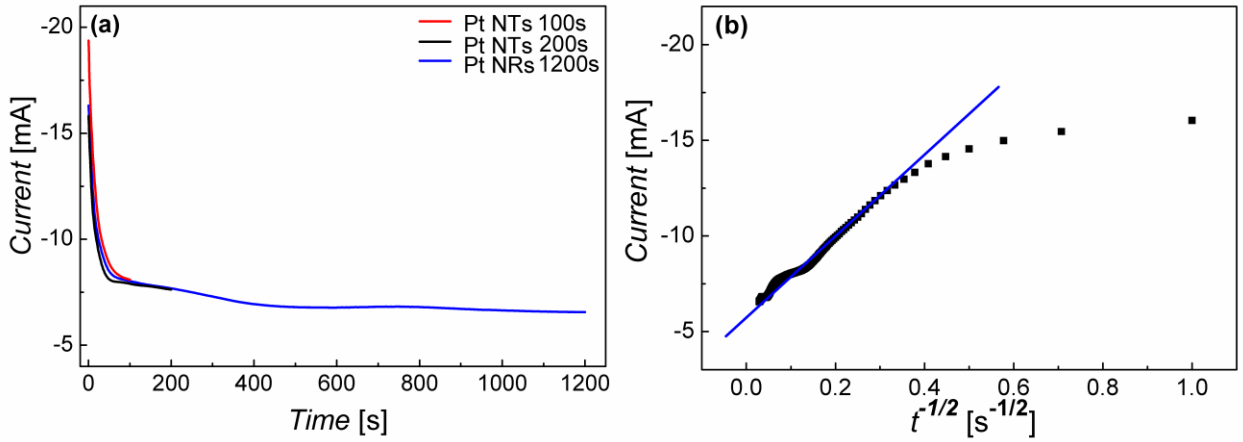

Figure 3.2: (a) The current–time curves of Pt-NSs showing the different deposition times from NTs to NRs. At the beginning higher currents show very fast nucleation and growth on sputtered Au which is present on the inside walls of the AAO template. (b) is the current versus $t^{-1/2}$ plot which shows linear relationship in diffusion control zone that is, sharp current decay part of curves in (a) [1] - Adapted by permission of The Royal Society of Chemistry.

negative $[PtCl_6]^{2-}$ ions. Now $[PtCl_6]^{2-}$ ions are reduced by accepting electrons from the negative electrode through the $[H_3O]^+$ ions layer as given by the equation 3.2.1 above.

Thus double layer charging makes the deposition process diffusion controlled and NTs walls formed in first high current zones start to thicken slowly in this diffusion limited zone. The third continuous current decay zone indicates a very slow decay in deposition current with the time where NTs are finally closed to give NRs morphology.

The current versus $t^{-1/2}$ plot shows linear relationship in diffusion controlled zone as shown in Figure 3.2(b). These features of potentiostatic current transient indicate that the electrodeposition is carried out by nucleation and growth mechanism through diffusion control [3,4].

In the continuous current decay zone the formation of NRs takes place which grow in upward direction with the time. The result is shown in Figure. 3.1(b) and (c), where the NTs have wall thicknesses of approximately 50 and 80 nm for 100 s and 200 s deposition times respectively, and despite some deformation, the NTs are self-standing and not collapsing.

Longer deposition times result in the progressive diffusion-limited filling of the NTs via multiple-site nucleation and growth, thus leading to the particular rough morphology of the NRs as shown in Figure 3.1(d).

Similarly wall thickness tuning of Au-NTs was also achieved using the same procedure, but understandably different deposition voltage and electrolyte concentration were used. The image sequence of Figure 3.3 shows that Au behaves similarly to Pt.

In case of Pd, electrodeposition was achieved directly on sputtered Au without the Pt-layer as used above to close the AAO template. In this way Pd nucleates on the Au sputtered inner wall of the AAO template to form a thin Pd-layer and subsequently thin wall Pd-NTs, shown in Figure 3.4 for a deposition time of 60s.

The process chosen here leads to polycrystalline 1D-NBNS as indicated exemplary by the XRD patterns of Pt-NTs and NRs shown in Figure 3.5, where reflections from the planes (111), (200), (220), (311) and (222) are present that are characteristic of the face centered cubic structure of polycrystalline Pt.

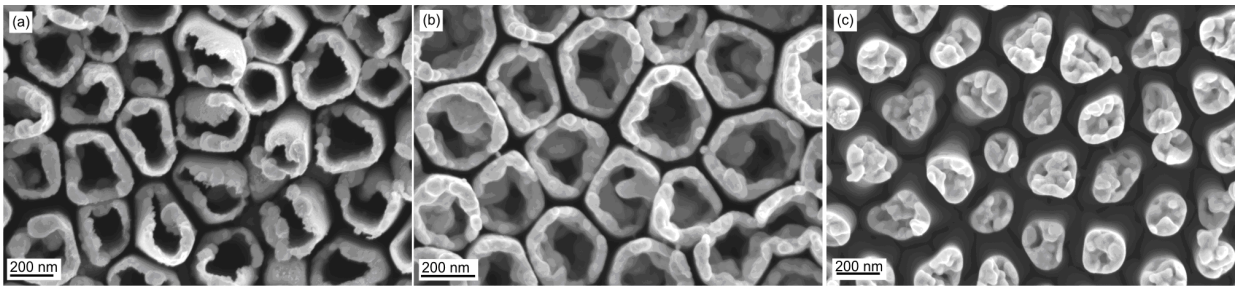

Figure 3.3: SE micrographs of 1D-Au-NSs obtained for increasing deposition times of (a) 120 s; (b) 160 s; (c) 300 s. Notice the growth morphology apparent in (b) where Au-particles nucleate on the inner NT-wall and grow towards the center of the NT to form the specific nanostructure of the NRs in (c) [1] - Reproduced by permission of The Royal Society of Chemistry.

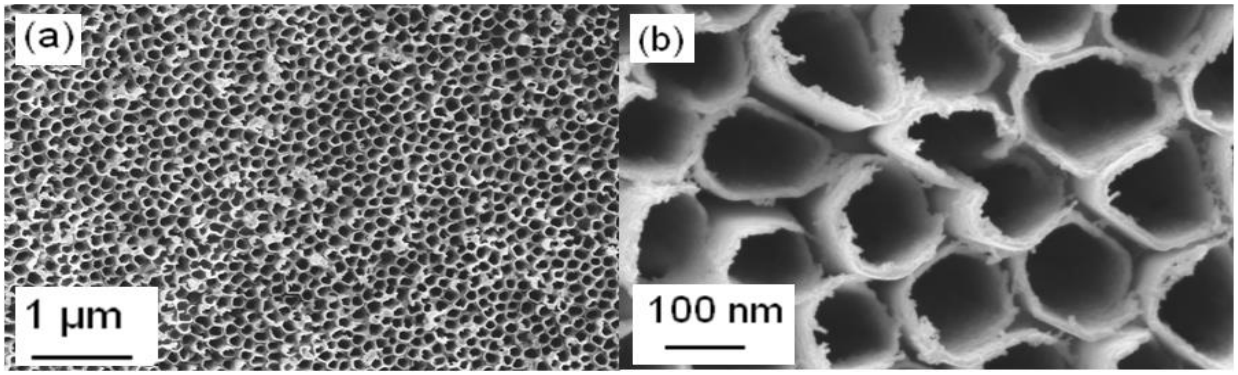

Figure 3.4: (a) Small and (b) higher magnification SE micrographs of the Pd NTs that were processed for the electrooxidation of formic acid [1] - Reproduced by permission of The Royal Society of Chemistry.

Thus by choosing an appropriate combination of deposition voltage and electrolyte concentration a high degree of morphology control of 1D NBNSs can be accessed via deposition time control. As the deposition current density varies with $t^{-1/2}$ in the diffusion-limited regime, morphology control with time appears to be easier for a selected set of experimental conditions.

Ponrouch et al. [5] did recently a systematic investigation of Pt-NTs and Pt-NWs in AAO using different deposition voltages and Pt^{4+} concentrations. The outcome of their results is that Pt-NTs

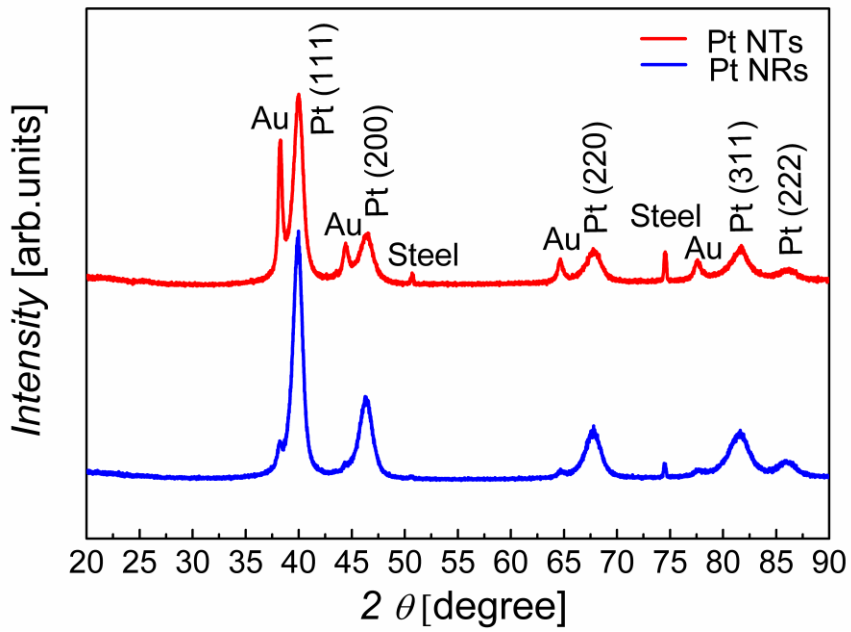

Figure 3.5: XRD patterns of the Pt NSs showing the polycrystalline nature of both the NTs and NRs. The patterns are shifted vertically for clarity. Steel denotes the peaks of the underlying stainless steel support [1] - Reproduced by permission of The Royal Society of Chemistry.

are obtained for small concentrations of Pt^{4+} in the range from 0.5 and 1.0 mM, and –0.15V in the absence of hydrogen. For higher concentrations (5mM) Pt-NWs form.

Our results show that Pt-NTs are obtained at a similar voltage, but with a Pt^{4+} concentration that is 2 orders of magnitude higher than the one they used. This stresses the importance the pore walls play in controlling the whole deposition process, i.e. electrolyte concentration gradient and deposition rate. In the case of Au-NSs extensive literature search didn't yield similar investigations to ours.

3.3.2 Multi-metallic nanostructures

The question has then arisen as to whether we can extend the approach above to the processing of layered multi-materials NTs. This could be interesting in a number of applications involving the tuning of optical properties [6], and also the processing of NT alloys.

3.3.2.1 Bimetallic

The morphology of the bimetallic nanotubes (BMNTs) Pt-Cu is shown in the Figure 3.6(a). The tubular structure is similar to Pt-NTs. The area scanned EDX spectrum shows the presence of both metals (Pt and Cu) along with sputtered Au (Figure 3.6(b). The Cu is present in very small amount (1.63 at. %) as compared to Pt (93 at. %) because of shorter deposition time (60 s).

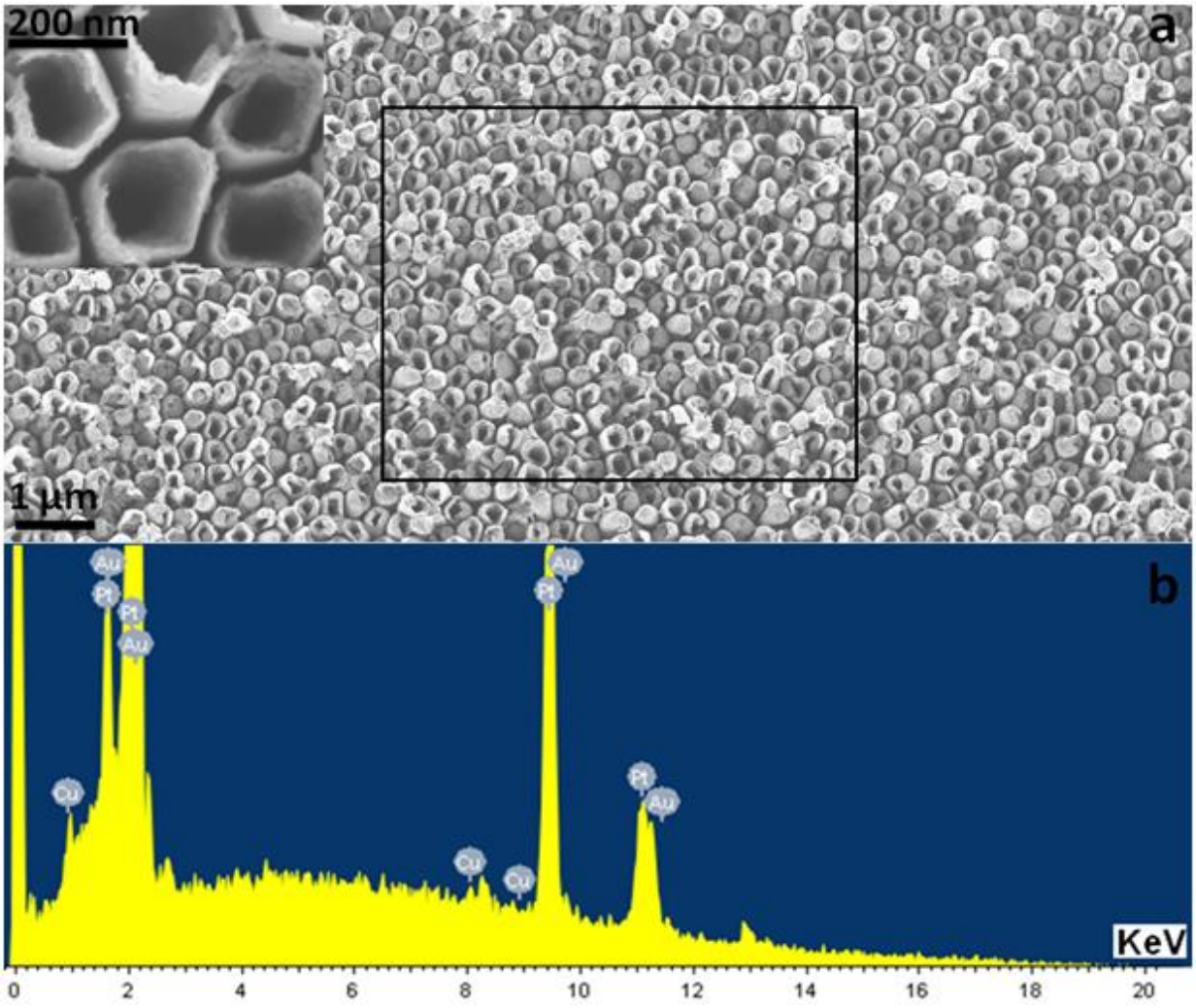

Figure 3.6: (a) is the SE micrograph of BMNTS of Pt-Cu (inset shows the high magnification image) and (b) is the EDX spectrum of scanned area shown with black lines in (a), it confirms the presence of both the metals Pt and Cu along with Sputtered Au.

Understandably amount of Cu can be increased by longer deposition times in the form of Pt-Cu NTs before it close and fill the NTs completely.

3.3.2.2 Trimetallic

Having achieved the bimetallic tubular structure, our interest developed to process and investigate the trimetallic nanotubes TMNTs using similar procedure.

Thus Pt-Ni-Au TMNTSs were processed with Pt-outer layer, Ni-sandwich layer and Au inner layer, as described in section 3.2.3 "Synthesis of multi-metallic nanotubes" by choosing the electrodeposition conditions outlined in Table 3.1. Figure. 3.7(a) shows the morphology of the Pt-Ni-Au-TMNTs that is in principle very similar to Au-NTs. The EDX spectrum of area scan and EDX profile of line scan on a TMNT in Figure 7(b) and (d) respectively confirms the presence of three elements.

Similarly Pt-Au-Cu TMNTSs were processed under the deposition conditions given in Table 3.1. The morphology and EDX spectrum are shown in Figure 3.8(a). It can be observed that TMNTs are of very rough morphology and EDX spectrum in Figure 3.8(b) indicates the presence of all the three metals (Pt, Au and Cu).

Thus self-standing TMNTs were successfully synthesized by employing appropriate electrodeposition conditions. Similar to monometallic NTs, time of electrodeposition was the key to control the morphology that is to keep them open in the form of NTs instead of completely filled and closed NRs. In all the multi-metallic NTs in this work, Pt supporting layer was electrodeposited at back side of the AAO template which also forms thin NTs walls due to the presence of sputtered Au on it. There was no bottom up filling by electrodeposition to strengthen the walls. It is in contrast to the monometallic NTs where Pt was electrodeposited by bottom up approach to strengthen the walls formed during electrodeposition of the supporting layer.

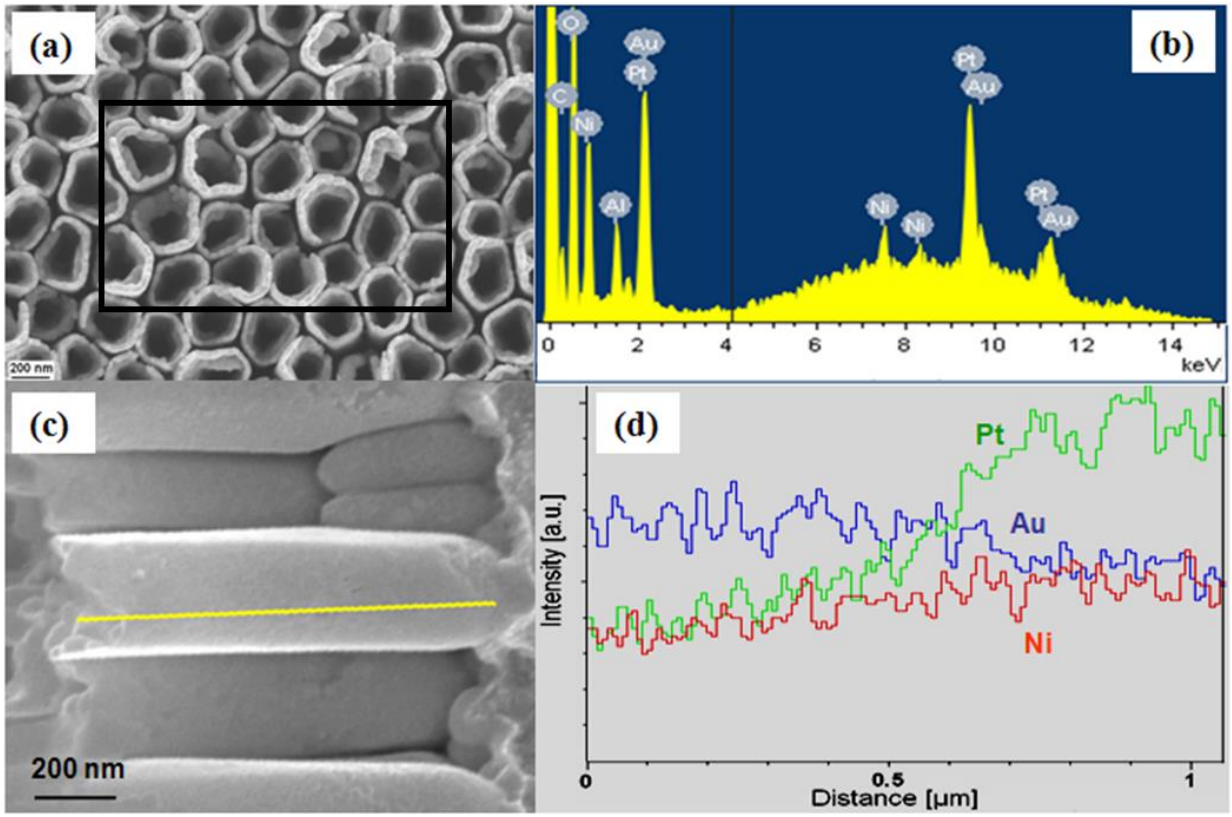

Figure 3.7: (a) and (c) are SE micrographs of the top and cross-sectional views of TMNTs obtained by sequential deposition of Pt, Ni and Au; (b) EDX spectrum of the area outlined in (a); (d) EDS line-scan obtained across the length of a TMNTs shown in (c). The EDS spectrum and profile confirm the presence of Pt, Ni and Au throughout the NT [1] - Reproduced by permission of The Royal Society of Chemistry.

The reason behind this is that the walls were to be further strengthened by the electrodeposition of second and or third metal layers. The time of electrodeposition of the second metal from its electrolyte was also carefully chosen after few attempts to avoid the complete closure of the NTs before electrodeposition of the third metal layer. Lastly, third metal is electrodeposited from its electrolyte again by a prudent choice of time to stop the thickening inner layer of NTs before it closes to form NRs. Extra care is required when a noble metal is electrodeposited on other metals with lower reduction potentials. It is because the noble metals ions in the solution will oxidize the already reduced/deposited metal if a favorable difference between reduction potentials is present between both the metals. For example, Au, Pt and Pd from their precursor solutions,

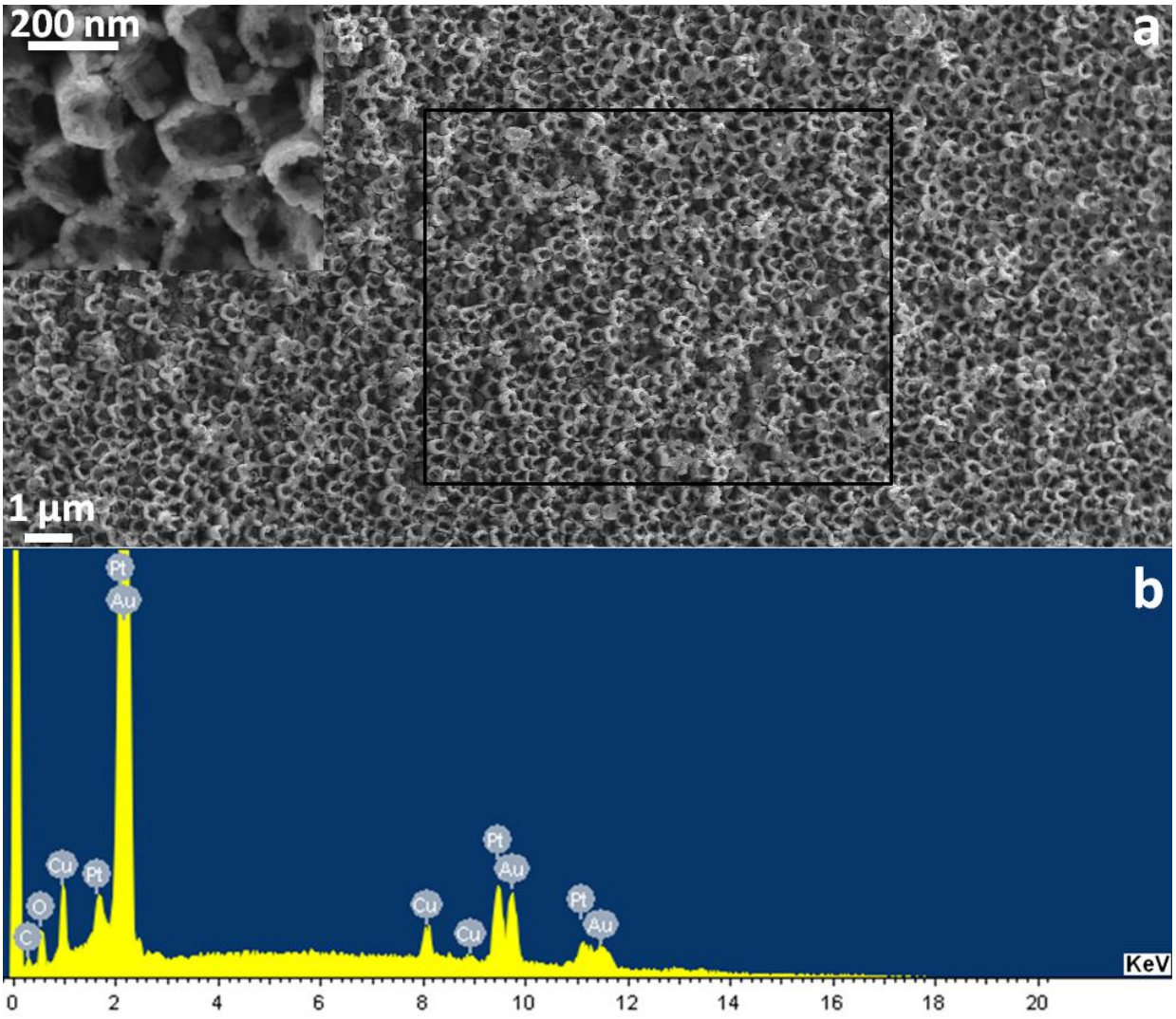

Figure 3.8: (a) is the SE micrograph of TMNTs of Pt-Au-Cu and (b) is the EDX spectrum of area scanned in (a). It confirms the presence of all the three metals. The inset shows the high magnification image of (a).

$HAuCl_4$, Na_2PtCl_4 and Na_2PdCl_4 respectively were deposited on the Ag nanostructure to form different hollow shaped noble metal nanostructures [7].

The oxidized metal will dissolve in the solution and noble metal ions (or any other metal ions with higher reduction potential) are reduced on the already existed metal. The phenomenon proceeds without supplying external current and is called galvanic replacement. It may etch

completely already electrodeposited thin metal layer if longer time is allowed to the process. Therefore, in the synthesis of Pt-Ni-Au NTs, time of deposition of Au on Ni is kept short that is 40 s to avoid the complete dissolution of already present Ni layer. We expect that galvanic replacement might have electrochemically etched some of the Ni in our case but have not replaced completely with Au and its presence is obvious in EDS spectrum as described earlier and shown in Figure 3.7(b) and (d).

We conclude that a similar approach can be applied to synthesize different multi-metallic NTs other than demonstrated in this work with different combination of metals. Furthermore, more than three metal layers should also be possible to form the walls of NTs by the same technique. Because this technique is based on electrodeposition, therefore, alloys should also be possible to form the layers of the walls of the NTs instead of or in combination with metals by electrodepositing them from their respective electrolytes. It is also obvious that by the same method, multi-metallic NRs with different layers can also be synthesized by closing the thickening NTs completely with the last metal by choosing appropriate time of electrodeposition.

References

[1] F. I. Dar, S. Habouti, R. Minch, M. Dietze and M. Es-Souni, *Morphology control of 1D noble metal nano/heterostructures towards multi-functionality*, J. Mater. Chem. **22**, 8671–8679 (2012).

[2] N. Taşaltın, S. Öztürk, N. Kılınç, H. Yüzer and Z. Z. Öztürk, *Fabrication of Pd–Fe nanowires with a high aspect ratio by AAO template-assisted electrodeposition*, Journal of Alloys and Compounds **509**, 3894–3898 (2011).

[3] H. Martín, P. Carro, A. Hernández Creus, S. González, R. C. Salvarezza, and A. J. Arvia, *Growth Mode Transition Involving a Potential-Dependent Isotropic to Anisotropic Surface Atom Diffusion Change. Gold Electrodeposition on HOPG followed by STM*, Langmuir **13**, 100–110 (1997).

[4] B. Scharifker and G. Hills, *Theoretical and experimental studies of multiple nucleation*, Electrochim. Acta **28**, 879–889 (1983).

[5] A. Ponrouch, S. Garbarino, S. Pronovost, P. L. Taberna, P. Simon and D. Guay, *Electrodeposition of Arrays of Ru, Pt, and PtRu Alloy 1D Metallic Nanostructures*, J. Electrochem. Soc. **157**(3), K59– K65 (2010).

[6] E. M. Prodan, C. Radloff, N. J. Halas and P. Nordlander, *A Hybridization Model for the Plasmon Response of Complex Nanostructures*, Science **302**, 419–422 (2003).

[7] S. E. Skrabalak, J. Chen, Y. Sun, X. Lu, L. Au, C. M. Cobley and Y. Xia, *Gold Nanocages: Synthesis, Properties, and Applications*, Acc. Chem. Res. **41**, 1587–1595 (2008).

4 Electrocatalysis of Pt and Pd Nanostructures

This chapter is also based on our paper [1] and presents the electrochemical characterization results of the synthesized Pt and Pd NSs which are used as catalyst electrodes. For this purpose, the electro-oxidation reactions on these NSs have been studied for applications in direct liquid fuel cells (DLFCs). Among the liquid fuels, methanol is preferred as electrochemical fuel in direct methanol fuel cells (DMFCs), because it is abundant and low cost fuel, easy to transport and store and have high theoretical energy density [2-4]. Among the catalysts Platinum is known to be an important and powerful catalyst for methanol electrooxidation reaction toward DMFCs [5,6]. Notwithstanding its high price that had triggered intense research activities to decrease its loading, for example via alloying [7-9], or composites [10,11] with other low cost elements, it remains in its pure form of critical importance due to its relatively high catalytic activity and long term stability [12,13].

A number of studies have shown that nanostructure morphology highly affects the electrocatalytic activity [14,15], and the results presented here corroborate these findings. Different Pt, Pd and Au nanostructure morphologies ranging mainly from nanoparticles of different shapes to occasionally nanodiscs, nanorods and nanotubes have been reviewed in literature for shape dependent electrocatalysis [16]. The previous studies clearly prove that electrocatalysis is strongly dependent on shape and consequently on crystal structure of the nanostructures [15,16]. For example, Pt nanoparticles of octahedral/tetrahedral shape showed better catalytic activity towards methanol electrooxidation than cubic shaped Pt nanoparticles in sulfuric acid [17]. The reason lies in the facets of the crystal structure of both the nanoparticles

[18]. A perfect cube has (100) facets which are more prone to poisoning than (111) facets of the octahedral/tetrahedral nanoparticles during electrooxidation of methanol [18]. In contrary to that, Pt nanocubes have been reported to exhibit higher electrocatalytic activity towards O_2 reduction reaction than polyhedral or truncated cubic nanoparticles dispersed in glassy carbon in 0.5 M H_2SO_4 [19,20]. This behavior is attributed to the difference in absorption ability of sulfate anions on Pt (100) and (111) facets. Similarly 1D nanostructures, such as unsupported Pt nanowires exhibit better electrochemical mass activity than the supported and unsupported Pt nanoparticle for methanol electrooxidation in highly Pt loaded catalyst [21]. The higher activity is attributed to the 1D morphology of Pt nanowires which improves the charge transfer by reducing particle interfaces as compared to nanoparticles. Furthermore, there is an efficient use of Pt due to the high aspect ratio of Pt nanowires in contrast to nanoparticles electrode where particles are prone to agglomeration that results in inefficient use of Pt.

In the same way, Pd nanostructures have shown morphology dependent electrocatalysis. For instance, cubic nanoparticles exhibited higher electrochemical activity towards formic acid oxidation than octahedral and cuboctahedral Pd nanoparticles [22]. The results agree with the previous findings of Pd (100) facets which are most active among Pd low index planes [23]. Pd nanothorns morphology has been reported to show 3 fold higher oxidation current than commercial Pd black for formic acid oxidation [24]. While Pd nanourchins, i.e. particles with sharp nanospikes, showed 4 times higher current density at 0.2 V than Pd black for formic acid electrooxidation reaction [25]. 1D Pd nanostructures also showed shape dependent electrocatalysis, e.g. Pd nanowires exhibited higher electrocatalytic activity and stability towards ethanol electrooxidation in potassium hydroxide as compared to Pd film mainly because of higher surface area of nanowires [26].

Thus, it is a well-known fact that electrocatalysis is strongly dependent on the shape of the nanostructures. It is mainly because the morphology and structure determines the factors such as surface area, surface energy, surface activity, poisoning ability, charge transport efficiency and efficient use of the electrocatalyst, which affect the electrocatalytic activity.

Therefore, in this work methanol electro-oxidation reaction on Pt NSs electrodes has been studied and compared with the different morphologies of NSs. While Pd NTs electrode prepared

in this work is studied for formic acid electro-oxidation because Pd-loaded electrocatalysts have been reported to be more powerful than Pt for the electro-oxidation of formic acid [27], although the mechanisms are similar. Formic acid in turns purportedly has lower cross over through the Nafion membrane [28] and higher kinetic activity than methanol. Direct formic acid fuel cells (DFAFCs) have higher power densities that should make them more appropriate than DMFCs for portable applications [29,30]. However, apart from few studies, essentially on commercial PdPt/C catalysts, only few reports were devoted to 1D Pd-nanostructures [31,32].

4.1 Sample preparation and experimental setup

Electrochemical experiments were performed on Pt and Pd NSs which were prepared and adhered to the steel substrate with the help of non-conductive double sided adhesive tape as described in chapter 3 (Morphology controlled synthesis of noble metal nanostructures). We used a silver paste to make an electrical contact to the NSs. To define the areas of NSs the exposed surfaces (steel, silver paste) not containing the NSs were electrically insulated with a non-conductive varnish. These samples with defined areas and electrical contact to NSs were used as working electrode for all electrochemical experiments. Deionized water was used to prepare aqueous solutions ($\geq$ 18MΩ). The Cyclic voltammograms (CVs) and chronoamperograms were conducted by the same electrochemical workstation, (ZAHNER IM6e, Germany) used for synthesis of NSs. All the electrochemical experiments were executed at room temperature in a standard three electrode cell. An Ag/AgCl (saturated KCl) was used as reference electrode and Pt mesh is used as counter electrode. All electrolytes were saturated with nitrogen (N_2) before each electrochemical experiment and all potentials are referred to standard hydrogen electrode (SHE). At first, the CVs for both NSs were recorded in 0.5 M H_2SO_4 at a scan rate 50 mVs^{-1} in the potential range between 0 to + 1.2 V and 0 to +1.4 V for Pt and Pd, respectively. The potential ranges selected in this work are based on two general factors, at first, it should include all the oxidation / reduction and hydrogen adsorption / desorption peaks regions of interest and secondly, it should not damage the electrode electrochemically. For this purpose, we run a several number of CVs on extra prepared samples in supporting electrolyte (0.5 M H_2SO_4) without the fuel (methanol or formic acid), to characterize the hydrogen interaction with

the electrode surfaces, and the typical oxidation and reduction peaks of electrodes. An optimum potential range is selected when stability of the electrode materials (Pt and Pd) is confirmed with in the CV cycles containing all the typical features of interest as mentioned above.

Pt-NSs (NRs and NTs) were tested for methanol and Pd-NTs for formic acid electrooxidation. The methanol electrooxidation on Pt-NSs was evaluated from the CVs recorded in an electrolyte containing 0.5 M H_2SO_4 and 0.5 M CH_3OH in the potential range between 0 and +1.2 V and chronoamperograms were recorded at 0.8 V for 1800 s in identical solutions. The formic acid electrooxidation on Pd-NTs was evaluated from the CVs performed in 0.5 M H_2SO_4 + 0.5 M HCOOH in the potential range between 0 and +1.2 V and chronoamperogram was recorded in identical solution at 0.25 V for 600 s. All CVs were recorded for several cycles until a stable curve is achieved. To compare the NRs and NTs with each other and with some of the results from literature all the currents in cyclic voltammograms and chronoamperograms are normalized with Pt or Pd (mg) loading.

The real surface area, *R* and the specific electrochemical active surface areas, *ECSA*, for both Pt and Pd NSs, were determined from the CVs recorded in 0.5 M H_2SO_4 as described in next two sections below. In the case of Pt-NSs the real surface area, *R* of the electrodes is calculated from the hydrogen desorption potential peaks, while for Pd-NTs, *R* was calculated from the charge required for the reduction of PdO. *R* and *ECSA* are important quantities that determine how active a catalytic surface is, and how it compares to other surfaces, taking into account the mass of deposited Pt (m_{Pt}) or Pd (m_{Pd}) metal.

4.2 Electrocatalytic oxidation of methanol on Pt nanostructures

Figure 4.1(a), shows CVs for the Pt NSs in an acid electrolyte (0.5 M H_2SO_4). The CVs exhibit typical Pt behavior under these conditions; different potential zones can be identified and correspond to the hydrogen adsorption and desorption region (0.05 to 0.4 V), double-layer plateau (0.4 to 0.7 V), and peaks for the formation of surface Pt oxides starting at 0.7 V and its

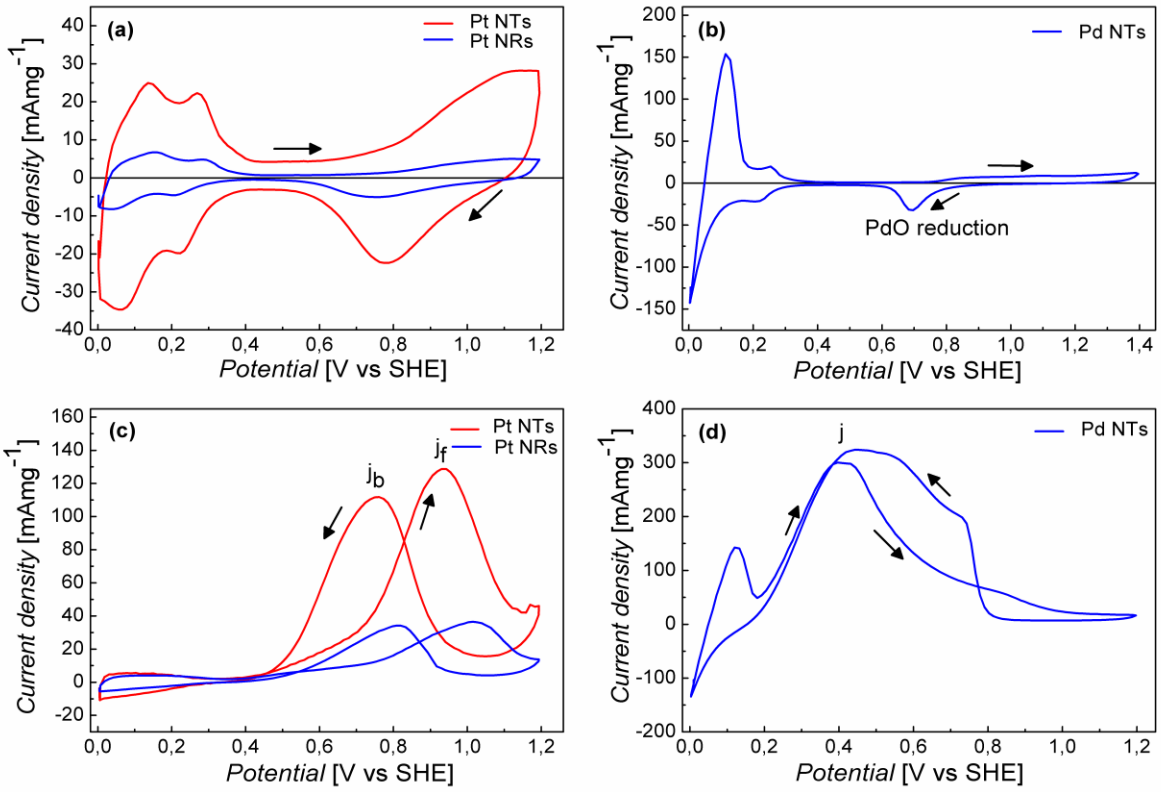

Figure 4.1: Cyclic voltammograms of NSs of Pt (a) (Pt-NTs red and Pt-NRs blue) and Pd (b) in 0.5 M H_2SO_4 aqueous solution at a scan rate of 50 mVs^{-1}. The electrocatalytic activity of Pt-NSs (c) and Pd-NTs (d) is shown by CVs recorded in aqueous solutions of 0.5 M H_2SO_4 + 0.5 M CH_3OH for Pt and 0.5 M H_2SO_4 + 0.5 M HCOOH for Pd at a scan rate of 50 mVs^{-1}. The hydrogen desorption region (0.05 to 0.4 V) in the forward scan was used to estimate the real surface area (R) for the Pt-NSs electrode (a); the PdO reduction peak region (0.57 to 0.86 V) in the backward scan was used to estimate *ECSA* for Pd (b). In (c) j_f and j_b are the peak current densities for forward and backward scans, respectively. j is the peak current density for the forward scan in (d) [1] – Reproduced by permission of The Royal Society of Chemistry.

reduction peak at 0.79 V [33], which suggests that our Pt NSs are active for the electro-oxidation without any substantial surface impurities.

The fine structure of the hydrogen desorption peaks in the potential range between 0.05 to 0.4 V in anodic direction has been attributed to microstructural effects related to specific Pt planes [34], that is, (111) Pt surface is responsible for hydrogen desorption at higher potential as compared to (110) Pt surface at lower potential due to difference in electronic and atomic arrangement of (111) and (110) Pt surfaces as explained with references in Chapter 2 "Theory", section 2.3 "Size and morphology effect on properties". The real surface areas, *R* of Pt-NTs and Pt-NRs were calculated from the hydrogen desorption region (0.05 to 0.4V in Figure 4.1(a) while excluding the double layer region using following equation (4.2.1).

$$R = \frac{Q_H}{vc} \tag{4.2.1}$$

Where Q_H denotes the integrated area of the hydrogen desorption region (expressed in units of V.A), v is the scan rate (Vs^{-1}) and c the charge density for monolayer hydrogen adsorption (210 μCcm^{-2}) on poly crystalline Pt [35]. The *ECSA* is then estimated using equation (4.2.2) in order to compare the performance of our NSs, and beyond this for comparison purposes with other structures reported in literature [7,36,37].

$$ECSA = \frac{R}{m_{Pt}} = \frac{RzF}{Q_d M} \tag{4.2.2}$$

Where m_{Pt} is the Pt loading (g), Q_d the charge (C) for Pt electrodeposition which is calculated from the integration of the current time curve recorded during Pt electrodeposition. M is the atomic weight of Pt ($gmol^{-1}$), z the number of transferred electrons and F the Faraday constant (96485.309 C mol^{-1}).

Table 4.1 summarizes the results obtained and compares them to those of other NSs from literature. Considering *ECSA* that is more appropriate for comparing the different NSs the value of 41 m^2g^{-1} obtained for the NTs is nearly fourfold that of the NRs (10.5 m^2g^{-1}). The higher surface to volume and surface to Pt loading ratio, are responsible for this behavior. In comparison to other NSs reported elsewhere the Pt-NTs surpass all other NSs, and are similar to porous Pt-Co-NWs (after 15h of de-alloying treatment) [7].

Table 4.1 Comparison of the electro-catalytic activities of Pt-NTs and NRs with literature data for Pt-NSs [7,36,37] *R* is the real surface area, *G* the geometrical surface area, *ECSA* the electrochemical active surface area, j_f and j_b stand for peak current density in forward and backward scan, respectively [1] – Adapted by permission of The Royal Society of Chemistry.

	Real surface area / Geometrical surface area	Specific electrochemical surface area	Peak current density	j_f / j_b
Electrode	*R / G*	*ECSA*		Resistance to poisoning
		m^2g^{-1}	$mAmg^{-1}$	
Pt-NRs	257.2	10.5	36.50	1.06
Pt-NTs	117.3	40.9	128.68	1.15
Pt-NRs[a]	57.65	11.26	60.57	0.81
Pt-NBs[a]	96	13.57	54.78	0.97
Pt-NTs[b]	40	25.6	166.4	1.2
Pt/C 30 (E-TEK)[c]	9.52	53.3	520	0.76
Pt-Co NWs[c]	7.74	46.4	2580	0.88

[a] Reference 36, [b] Reference 37, [c] Reference 7

The electro-catalytic activity was exemplary evaluated on methanol electrooxidation. It is generally well accepted that the electro-oxidation of methanol follows the sequences outlined in

reactions 4.2.3-5, where methanol first adsorbs on the surface of Pt, oxidizes to CO and finally to CO_2.

$$Pt + CH_3OH \rightarrow Pt - (CH_3OH)_{ads} \tag{4.2.3}$$

$$Pt - (CH_3OH)_{ads} \rightarrow Pt - (CO)_{ads} + 4H^+ + 4e^- \tag{4.2.4}$$

$$Pt - (CO)_{ads} + H_2O \rightarrow Pt + CO_2 + 2H^+ + 2e^- \tag{4.2.5}$$

The cumulative reaction equation can be written as follows:

$$Pt + CH_3OH + H_2O \rightarrow Pt + CO_2 + 6H^+ + 6e^- \tag{4.2.6}$$

Figure 4.1(c) shows that the overall catalysis output of Pt-NTs surpasses those of Pt-NRs, in terms of on-set potentials and peak current in forward scan, j_f, a result mainly amenable to higher energies at edges of the tube walls and their higher surface to volume ratio. Moreover the improved catalytic performance can be ascribed to the ordered hollow structure of NTs which provides a unidirectional electronic channel that reduce the effects of grain boundaries [38,39].

A direct comparison can be made with Pt-NSs that were processed using ZnO-NSs as sacrificial templates [36,37]. The performance in terms of peak current/Pt-loading ratio is overall better for our Pt-NTs except for hollow Pt-NTs that were processed using ZnO-NTs as template. Most probably the surface porosity on the thin walls of the Pt-NTs processed by ZnO-NSs as sacrificial template plays a role for its enhanced catalytic activity. In comparison to similar Pt-NSs, e.g. porous Pt-Co-NWs [7] which were processed with the help of AAO template, the performance of our NTs is still to be improved, though a direct comparison here is difficult to be made, as the size, and morphology of the NSs are quite different. For example Pt-Co-NWs [7] were processed with smaller pore diameter (28 nm) AAO template than ours (200 nm diameter) and final diameter of the wires after Co de-alloying treatment was down to 2 nm which is smaller than ours by a factor of 100. Moreover, these Pt-Co-NWs have very small pores (less than 1 nm to 5 nm) and a higher concentration (1 M) of methanol is used as compared to us (0.5 M) for catalytic activity measurements.

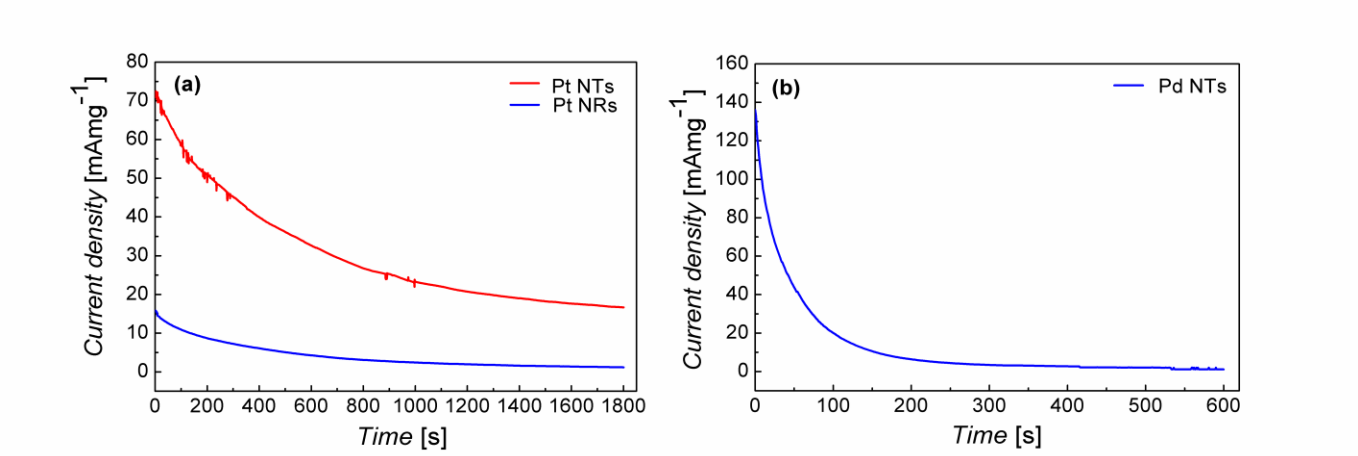

Figure 4.2: (a) Chronoamperograms of Pt-NSs (NTs red and NRs blue) at 0.8 V (vs. SHE) in 0.5 M H_2SO_4 + 0.5 M CH_3OH aqueous solution. (b) Chronoamperogram of Pd-NTs at 0.25 V (vs. SHE) in 0.5 M H_2SO_4 + 0.5 M HCOOH aqueous solution [1] – Reproduced by permission of The Royal Society of Chemistry.

In backward scan direction, a second anodic peak current, j_b, corresponds to the removal of incompletely oxidized carbonaceous species formed in forward scan and adsorbed on Pt surface [40]. For example, CO is one of the poisoning species formed during methanol oxidation on Pt surface in forward scan direction. It is electrochemically oxidized in backward potential sweep according to following reaction 4.2.7 [41,42].

$$Pt-OH + Pt-CO \rightarrow CO_2 + 2Pt + H^+ + e^- \qquad (4.2.7)$$

Usually the resistance to poisoning is estimated by the ratio, j_f / j_b, [43,44]. A lower (j_f / j_b) ratio indicates that methanol oxidation in forward scan is relatively inefficient, and poisonous species are accumulating on catalyst surface. A higher (j_f / j_b) ratio reflects that catalyst is better resistant and poisonous species are more effectively removed from the surface of the catalyst. Our results for resistance to poisoning (j_f / j_b) compare advantageously to other nanostructures [7,36,37], except for Pt-NTs [37].

Chronoamperometry is the method to evaluate the long term electrocatalysis performance of an electrode more realistically at a particular potential for a certain period of time. Therefore,

chronoamperograms (CA) were recorded in identical electrolytes (0.5 M H_2SO_4 + 0.5 M CH_3OH) for 1800 s by holding the potential at 0.8 V to test the long term performance of the Pt-NS electrodes, and are compared in Figure 4.2(a). Methanol was oxidized continuously at this potential and current was recorded against time. The initial parts of the CA curves in Figure 4.2(a) show relatively sharp decay in current as compared to lateral part of the curves which starts to stabilize near the end point of the time selected here (1800 s). It is because during the electrooxidation process, methanol is first oxidized to CO (equation 4.2.4) which poisons the electrode and hinders the further adsorbance and subsequent electrooxidation of the methanol on the surface of the electrode. Therefore, CO needs to be immediately further oxidized to CO_2 to complete the oxidation process (equation 4.2.5). However, the poisonous CO would accumulate on the surface of the Pt if the kinetics of its oxidative removal cannot keep pace with methanol electrooxidation reaction. The sharp decay in current indicates the accumulation and poisoning effect of the electrode surface with CO. Furthermore, the current during electrooxidation of methanol on electrode surface follows the Cottrell equation (chapter 2 equation 2.1.6) that is, current decreases with $t^{-1/2}$ and being a diffusion controlled process it again points out the importance of effective and immediate oxidative removal of the poisonous CO to allow further methanol molecules to access the electrode surface. Hence, slower decay in the polarization current indicates the better resistance to poisoning [45]. The starting current density for the Pt-NTs (72 $mAmg^{-1}$) is more than 4 times higher than that of the Pt-NRs (15.8 $mAmg^{-1}$) which agrees with the CV results obtained for both the Pt NSs in identical electrolytes (Figure 4.1 (c)). Moreover, current decay was slower for the Pt-NTs: the current density is reduced to 23.12 % (16.65 $mAmg^{-1}$) of its original value in comparison to 7.48 % (1.83 $mAmg^{-1}$) for the Pt-NRs. It means that CO is more efficiently being oxidized to CO_2 on Pt-NTs as compared to Pt-NRs and hence, Pt-NTs show more resistance to poisoning than Pt-NRs. It concludes that long term electrocatalytic performance of Pt-NTs is much better than Pt-NRs which again stresses the effects of morphology on the catalytic properties of Pt-NSs. Again direct comparison of our CA results is difficult to be made not only because of the factors described earlier in this section but also due to difference in potential selected for electrooxidation in CA measurements. However, an estimated comparison of the long term performance can be made by calculating the percentage of current decay after same period of time. Our CA results for Pt-NTs (current density reduced to ~ 23 % of its original value) showed better performance than, Pt-Co NWs

(current density reduced to ~ 15 % of its original value at applied potential of 0.85 V) [7] and Pt-NRs (current density reduced to ~ 19 % of its original value at applied potential of 0.72 V) [36] and are comparable to Pt-NBs (current density reduced to ~ 25 % of its original value at applied potential of 0.72 V) [36] after 1800 s.

4.3 Electrocatalytic oxidation of formic acid on Pd nanostructures

Pd shows a differentiated behavior from Pt-based electrocatalysts because of its ability to absorb hydrogen electrochemically from basic or acidic aqueous solutions at a suitable potential [46]. The absorption of hydrogen into the Pd lattice follows the so called "dissolution adsorption mechanism" in which first H^+ ions adsorb onto the Pd surface and are subsequently reduced to adsorbed hydrogen atoms. Finally these adsorbed hydrogen atoms diffuse into bulk Pd. These diffused hydrogen atoms residing underneath first few atomic layers of Pd form absorbed hydrogen [47,48]. The adsorption and absorption behavior of hydrogen on Pd hinders the determination of active surface area from hydrogen adsorption / desorption peaks region in the CVs as explained below.

In a similar way to Pt we first examine the CV curve recorded in 0.5 M H_2SO_4 aqueous solution in order to determine the catalyst active surface area (Fig. 4.1(b)). Multiple peaks are obtained in hydrogen adsorption / desorption regions between 0 and 0.35 V. The two anodic peaks, the first large one at 0.12 V and the second small peak at 0.26 V have been reported earlier with different interpretations [49-52] The first peak is attributed to the oxidation of absorbed hydrogen alone or adsorbed and absorbed hydrogen together on Pd surface. The second anodic peak at 0.26 V is exclusively attributed to the oxidation of adsorbed hydrogen [52]. The two distinct peaks for oxidation of adsorbed and absorbed hydrogen are exhibited exclusively by Pd nanostructures [53-56], while bulk Pd has a single broad peak for oxidation of adsorbed and absorbed hydrogen [55,56]. This marked feature is attributed to the large number of surface sites available for adsorption of hydrogen on Pd NSs. The surface oxidation of Pd to PdO begins at 0.8 V, indicated by the increase in current in forward scan direction while the peak at 0.7 V in reverse scan,

correspond to the reduction of PdO formed in forward scan. As mentioned above, the active surface area of Pd NSs cannot be determined reliably from hydrogen adsorption / desorption; this is why we employed the most common and convenient method to determine *ECSA*. In this method the quantity of charge used for PdO reduction was calculated by integrating the PdO reduction peak region (between 0.57 and 0.86 V). This charge was then used for the estimation of *ECSA* using the following equation [57].

$$ECSA = \frac{Q_0}{vcm} \tag{4.3.1}$$

Where Q_o is the integrated charge of PdO reduction, υ the scan rate (Vs^{-1}) c the charge density 424μCcm^{-2} associated with reduction of one monolayer of PdO [58]. The *ECSA* value, 55.8 mCmg^{-1} obtained for Pd NTs is comparable to the recent work from literature [59] listed in Table 4.2.

The electro-catalytic activity was evaluated from CV in 0.5 M H_2SO_4 + 0.5 M HCOOH solution as shown in (Fig. 4.1(d)). It displays the general characteristic behavior of Pd voltammogram [60-65]. The oxidation of formic acid on Pd mainly follows direct pathways as compared to Pt where oxidation follows both direct and indirect CO pathways [49,66] and is given by the following equation.

$$Pd + HCOOH \rightarrow Pd + CO_2 + 2H^+ + 2e^- \tag{4.3.2}$$

In forward scan the small peak at about 0.12 V corresponds to hydrogen oxidation [61]. The broad anodic peak at 0.4 V corresponds to the HCOOH oxidation. A small hump between 0.8 and 0.9 V corresponds to the oxidation of Pd [67]. In reverse scan the shoulder at ~0.75 V indicates the oxidation of HCOOH at freshly exposed Pd-surface upon reduction of PdO that was formed in forward scan [68,69]. Although HCOOH electrooxidation on Pd surface is believed to follow mainly direct pathways as mentioned above, there are still substantial amount of poisonous species produced in this process. For example, in the reverse scan main oxidation peak is slightly higher than the oxidation peak in forward scan.

Table 4.2 *ECSA* values and peak current densities of Pd-NTs in comparison to literature data of different Pd-NSs [1] – Reproduced by permission of The Royal Society of Chemistry.

Electrode	Specific electrochemical surface area *ECSA* $mCmg^{-1}$	Peak current density J $mAmg^{-1}$
Pd NTs	55.8	300.3
Pd/C[a]	54.7	~700
$Pd_{25}Ni_{75}$ alloy NRs[a]	15.1	~310
$Pd_{57}Ni_{43}$ alloy porous NRs[a]	58.4	~850

a Reference [59]

This behavior is similar to commercial Pd/C catalyst [61] and indicates the poor tolerance for poisoning by CO. It makes HCOOH oxidation on Pd similar to methanol oxidation process on Pt surface. The oxidation of HCOOH is evaluated from the peak current in forward scan. The peak current density at 0.4 V is 300.3 $mAmg^{-1}$ in forward scan direction is comparable to $Pd_{25}Ni_{75}$ alloy NRs, but inferior to both Pd/C and porous $Pd_{57}Ni_{43}$ NRs [59]. On one hand, the superior electrooxidation results by porous structure of $Pd_{57}Ni_{43}$ NRs [59] are attributed to the increase in active surface area caused by de-alloying of Ni which improves the electrooxidation of HCOOH. On the other hand, modification of electronic structure of Pd due to Ni, that is, transfer of electron from Ni to Pd causes the negative shift in the binding energy of Pd by ~ 0.2 eV [59], and is believed to enhance the oxidation and effective removal of CO [70] which also leads to better electrocatalytic performance of the porous $Pd_{57}Ni_{43}$ NRs for HCOOH. However a thorough

comparison is difficult because in literature a certain amount of loose NWs is fixed on typical carbon supports for fuel cells, e.g. Vulcan X-72, whereas in our experiment the NSs are supported on a metallic film. Among the many factors that influence the performance of a noble metal catalyst carbon supports are certainly not to be neglected [71], which play an important role in making the electrooxidation reaction efficient because of its high electrical conductivity. Notwithstanding the difference in the experimental conditions further optimization of our structures is still needed.

Similar to Pt-NSs the catalytic long term stability of the Pd-NTs electrode is tested from the CA curves recorded by holding a potential at 0.25 V for 600 s (Figure. 4.2(b)). The polarization current initially falls steeply (from 130 $mAmg^{-1}$) due to the formation of poisonous CO which accumulate at the surface of the Pd-NTs electrode and then reaches to a steady-state value (1.1 $mAmg^{-1}$) in the first 250 s. It indicates the detrimental effect of the presence of poisonous CO on the catalyst and stresses the importance of its effective removal.

At first, our synthesized Pt and Pd NSs electrodes established that they are highly active for electrochemical experiments by depicting all the typical features of Pt and Pd when CVs were performed in 0.5 M H_2SO_4 on individual electrodes before electrochemical oxidation. It negates the possibility of passivation of electrodes or presence of sizable impurities on the surface of electrodes, the absence of which is important for an efficient electrooxidation reaction. The electrochemical active surface area (*ECSA*) which is one of the important factors that determine the amount of electrooxidation reaction, was calculated from the same CVs in 0.5 M H_2SO_4 and showed a strong dependence on morphology of NSs electrodes that is, Pt-NTs electrode showed higher *ECSA* value as compared to Pt-NRs electrode. When compared with some of the similar work from literature our NTs electrodes of Pt and Pd showed higher *ECSA* values in most of the cases, and comparable or lower value in some of the cases.

Similarly, electrocatalytic performance of our Pt and Pd NSs evaluated in methanol and formic acid fuels, respectively, showed very strong dependence on morphology of NSs. The Pt-NTs electrode showed substantially higher electrocatalytic performance in comparison to Pt-NRs electrode both in terms of peak current density and long term stability. Again, our Pt-NTs electrode showed better or comparable electrocatalytic performance in comparison to similar

work from literature. However, our Pd-NTs electrode exhibited comparable or inferior performance in terms of current density when compared with published work [59], it, nevertheless, still need further optimization because it is prone to poisoning by intermediate products such as CO.

The superior electrocatalysis performance by porous alloy structures from literature once again highlights the important role of structure and morphology in the electrooxidation reactions on Pd and Pt surfaces. We nevertheless may state that our results are quite encouraging and competitive, especially for Pt-NTs.

References

[1] F. I. Dar, S. Habouti, R. Minch, M. Dietze and M. Es-Souni, *Morphology control of 1D noble metal nano/heterostructures towards multi-functionality*, J. Mater. Chem. **22**, 8671–8679 (2012).

[2] C. Lamy, A. Lima, V. LeRhun, F. Delime, C. Coutanceau and J.M. Léger, *Recent advances in the development of direct alcohol fuel cells (DAFC)*, J. Power Sources **105**, 283–296 (2002).

[3] E. Reddington, A. Sapienza, B. Gurau, R. Viswanathan, S. Sarangapani, E.S. Smotkin and T.E. Mallouk, *Combinatorial Electrochemistry: A Highly Parallel, Optical Screening Method for Discovery of Better Electrocatalysts*, Science **280**, 1735–1737 (1998).

[4] M. Winter, R. J. Brodd, *What* a*re batteries, fuel cells, and supercapacitors?*, Chem. Rev. **140**, 4245–4269 (2004).

[5] W. Chrzanowski and A. Wieckowski in *Interfacial Electrochemistry*, Ed: Marcel Dekker, New York, p 937 (1999).

[6] T. Iwasita in *Handbook of Fuel Cells: Fundamentals, Technology and Applications*, Vol. 2, Eds: W. Vielstich, A. Lamm and H. A. Gasteiger, John Wiley & Sons: Chichester, p 603 (2003).

[7] L. Liu, E. Pippel, R. Scholz and U. Gösele, *Nanoporous pt-co alloy nanowires: fabrication, characterization, and electrocatalytic properties*, Nano Lett., **9**(12), 4352–4358 (2009).

[8] T.-Y. Jeon, K.-S. Lee, S. J. Yoo, Y.-H. Cho, S. H. Kang and Y.-E. Sung, *Effect of Surface Segregation on the Methanol Oxidation Reaction in Carbon-Supported Pt-Ru Alloy Nanoparticles*, Langmuir **26**(11), 9123–9129 (2010).

[9] C. Xu, Q. Li, Y. Liu, J. Wang, and H. Geng, *Hierarchical Nanoporous PtFe Alloy with Multimodal Size Distributions and Its Catalytic Performance toward Methanol Electrooxidation*, Langmuir, **28**(3), 1886–1892 (2012).

[10] Y. Li, L. Tang and J. Li, *Preparation and electrochemical performance for methanol oxidation of pt/graphene nanocomposites*, Electrochemistry Communications **11**, 846–849 (2009).

[11] W. Zhou, Y. Du, F. Ren, C. Wang, J. Xu and P. Yang, *High efficient electrocatalytic oxidation of methanol on Pt/polyindoles composite catalysts*, International journal of hydrogen energy **35**, 3270–3279 (2010).

[12] Z. Li, L. Zhang, X. Huang, L. Ye and S. Lin, *Shape-controlled synthesis of Pt nanoparticles via integration of graphene and β-cyclodextrin and using as a noval electrocatalyst for methanol oxidation*, Electrochimica Acta **121**, 215–222 (2014).

[13] H.-Y. Lee, W. Vogel and P. P.-J. Chu, *Nanostructure and Surface Composition of Pt and Ru Binary Catalysts on Polyaniline-Functionalized Carbon Nanotubes*, Langmuir **27**, 14654–14661 (2011).

[14] C. J. Zhong, J. Luo, B. Fang, B. N. Wanjala, P. N. Njoki, R. Loukrakpam and J. Yin, *Nanostructured catalysts in fuel cells*, Nanotechnology **21**, 062001 (2010).

[15] J. S.-Gullón, F. J. V. Iglesias, A. L. Cudero, E. Garnier, J. M. Feliu and A. Aldaz, *Shape-dependent electrocatalysis: methanol and formic acid electrooxidation on preferentially oriented Pt nanoparticles*, Phys. Chem. Chem. Phys. **10**, 3689–3698 (2008).

[16] J. Solla-Gullo´n, F. J. Vidal-Iglesias and J. M. Feliu, *Shape dependent electrocatalysis*, Annu. Rep. Prog. Chem., Sect. C **107**, 263–297 (2011).

[17] C. Susut, G. B. Chapman, G. Samjeske´, M. Osawa and Y. Tong, Phys. Chem. Chem. Phys., *An unexpected enhancement in methanol electro-oxidation on an ensemble of Pt (111) nanofacets: a case of nanoscale single crystal ensemble electrocatalysis* **10**, 3712–3721 (2008).

[18] E. Herrero, K. Franaszczuk and A. Wieckowski, *Electrochemistry of Methanol at Low Index Crystal Planes of Platinum: An Integrated Voltammetric and Chronoamperometric Study*, J. Phys. Chem. B **98**, 5074–5083 (1994).

[19] C. Wang, H. Daimon, Y. Lee, J. Kim and S. Sun, *Synthesis of Monodisperse Pt Nanocubes and Their Enhanced Catalysis for Oxygen Reduction*, J. Am. Chem. Soc. **129**, 6974 (2007).

[20] C. Wang, H. Daimon, T. Onodera, T. Koda and S. Sun, *A General Approach to Size and Shape Controlled Synthesis of Pt Nanoparticles and Their Catalysis for Oxygen Reduction Reaction*, Angew. Chem. Int. Ed. **47**, 3588 (2008).

[21] S. M. Choi, J. H. Kim, J. Y. Jung, E. Y. Yoon and W. B. Kim, *Pt nanowires prepared via a polymer template method: Its promise toward high Pt-loaded electrocatalysts for methanol oxidation*, Electrochimica Acta **53**, 5804–5811 (2008).

[22] S. E. Habas, H. Lee, V. Radmilovic, G. A. Somorjai and P. Yang, *Shaping binary metal nanocrystals through epitaxial seeded growth*, Nat. Mater. **6**, 692–697 (2007).

[23] N. Hoshi, K. Kida, M. Nakamura, M. Nakade and K. Osada, *Structural Effects of Electrochemical Oxidation of Formic Acid on Single Crystal Electrodes of Palladium*, J. Phys. Chem. B 110, 12480–12484 (2006).

[24] H. Meng, S. Sun, J. P. Masse and J. P. Dodelet, *Electrosynthesis of Pd Single-Crystal Nanothorns and Their Application in the Oxidation of Formic Acid*, Chem. Mater. **20**, 6998–7002 (2008).

[25] Y. Fang, S. Guo, C. Zhu, S. Dong and E. Wang, *Twenty Second Synthesis of Pd Nanourchins with High Electrochemical Activity through an Electrochemical Route*, Langmuir **26**, 17816–17820 (2010).

[26] H. Wang, C. Xu, F. Cheng and S. Jiang, *Pd nanowire arrays as electrocatalysts for ethanol electrooxidation*, Electrochem. Commun. **9**, 1212–1216 (2007).

[27] Z. Liu, L. Hong, M. P. Tham, T. H. Lim and H. Jiang, *Nanostructured Pt/C and Pd/C catalysts for direct formic acid fuel cells*, Journal of Power Sources **161**, 831–835 (2006).

[28] Y.-W. Rhee, S. Y. Ha and R. I. Masel, *Crossover of formic acid through Nafion membranes*, Journal of Power Sources **117**, 35–38 (2003).

[29] X. Yu and P. G. Pickup, *Recent advances in direct formic acid fuel cells (DFAFC)*, Journal of Power Sources **182**, 124–132 (2008).

[30] U. B. Demirci, *Direct liquid-feed fuel cells: Thermodynamic and environmental concerns*, Journal of Power Sources **169**, 239–246 (2007).

[31] H. Meng, S. Sun, J.-P. Masse and J.-P. Dodelet, *Electrosynthesis of Pd Single-Crystal Nanothorns and Their Application in the Oxidation of Formic Acid*, Chem. Mater. **20**, 6998–7002 (2008).

[32] J. Wang, Y. Chen, H. Liu, R. Li and X. Sun, *Synthesis of Pd nanowire networks by a simple template-free and surfactant-free method and their application in formic acid electrooxidation*, Electrochemistry Communications **12**, 219–222 (2010).

[33] C. H. Hamann, A. Hamnett and W. Vielstich, *Electrochemistry*, 2nd ed., Wiley–VCH, Weinheim, Chapter 4, (1998).

[34] A. V. Tripkovic, S. LJ. Gojkovic, K. DJ. Popovic and J. D. Lovic, *Methanol oxidation at platinum electrodes in acid solution: Comparison between model and real catalysts*, J. Serb. Chem. Soc. **71**(12), 1333–1343 (2006).

[35] T. Biegler, D. A. J. Rand and R. Woods, *Limiting oxygen coverage on platinized platinum; Relevance to determination of real platinum area by hydrogen adsorption*, J. Electroanal. Chem. **29**, 269–277 (1971).

[36] R. Minch and M. Es-Souni, *A versatile approach to processing of high active area pillar coral- and sponge-like Pt-nanostructures. Application to electrocatalysis*, J. Mater. Chem. **21**, 4182–4188 (2011).

[37] R. Minch and M. Es-Souni, *On substrate, self-standing hollow-wall Pt and PtRu-nanotubes and their electrocatalytic behavior*, Chem. Commun. **47**, 6284–6286 (2011).

[38] L. Xing, J. Jia, Y. Wang, B. Zhang and S. Dong, *Pt modified TiO2 nanotubes electrode: Preparation and electrocatalytic application for methanol oxidation*, International Journal of hydrogen energy **35**, 12169–12173 (2010).

[39] Q. Zheng, B. X. Zhou, J. Bai, L. H. Li, Z. J. Jin, J. L. Zhang, J. H. Li, Y. B. Liu, W. M. Cai and X. Y. Zhu, *Self-organized TiO_2 nanotube array sensor for the determination of chemical oxygen demand*, Adv. Mater. **20**, 1044–1049 (2008).

[40] R. Manoharan and J. B. Goodenough, *Methanol Oxidation in Acid on NiTi*, J. Mater. Chem. **2**(8), 875–887 (1992).

[41] J. H. Kim, S. M. Choi, S. H. Nam, M. H. Seo, S. H. Choi and W. B. Kim, *Influence of Sn content on PtSn/C catalysts for electrooxidation of C1–C3 alcohols: Synthesis, characterization, and electrocatalytic activity*, Appl. Catal. B: Environ. **82**, 89–102 (2008).

[42] Z. Chen, L. Xu, W. Li, M. Waje and Y. Yan, *Polyaniline nanofibre supported platinum nanoelectrocatalysts for direct methanol fuel cells*, Nanotechnology **17**, 5254–5259 (2006).

[43] E. Yoo, T. Okata, T. Akita, M. Kohyama, J. Nakamura and I. Honma, *Enhanced electrocatalytic activity of Pt subnanoclusters on graphene nanosheet surface*, Nano Lett. **9**(6), 2255–2259 (2009).

[44] Y. Mu, H. Liang, J. Hu, L. Jiang, L. Wan, *Controllable Pt Nanoparticle Deposition on Carbon Nanotubes as an Anode Catalyst for Direct Methanol Fuel Cells*, J. Phys. Chem. B **109**, 22212-22216 (2005).

[45] B. Liu, J. H. Chen, X. X. Zhong, K. Z. Cui, H. H. Zhou and Y. F. Kuang, *Preparation and electrocatalytic properties of Pt–SiO2 nanocatalysts for ethanol electrooxidation*, J. Colloid Interface Sci. **307**, 139–144 (2007).

[46] G. Jerkiewicz, *Hydrogen sorption ATIN electrodes*, Prog. Surf. Sci. **57**, 137–186 (1998).

[47] M. W. Breiter, *Dissolution and adsorption of hydrogen at smooth Pd wires at potentials of the alpha phase in sulfuric acid solution*, J. Electroanal. Chem. **81**, 275–284 (1977).

[48] G. Mengoli, M. Fabrizio, C. Manduchi and G. Zannoni, *Surface and bulk effects in the extraction of hydrogen from highly loaded Pd sheet electrodes*, J. Electroanal. Chem. **350**, 57–72 (1993).

[49] X-M. Wang and Y-Y. Xia, *Synthesis, characterization and catalytic activity of an ultrafine Pd/C catalyst for formic acid electrooxidation*, Electrochimica Acta **54**, 7525–7530 (2009).

[50] A. Czerwiński, R. Marassi and S. Zamponi, *The absorption of hydrogen and deuterium in thin palladium electrodes: Part I. Acidic solutions*, J. Electroanal. Chem. **316**, 211–221 (1991).

[51] A. Czerwiński, *The adsorption of carbon oxides on a palladium electrode from acidic solution*, J. Electroanal. Chem. 379, 487–493 (1994).

[52] A. N. Correia, L. H. Mascaro, S. A. S. Machado and L. A. Avaca, *Active surface area determination of Pd-Si alloys by H-adsorption*, Electrochim. Acta **42**, 493–495 (1997).

[53] H.-P. Liang, N. S. Lawrence, T. G. J. Jones, C. E. Banks and C. Ducati, *Nanoscale Tunable Proton/Hydrogen Sensing: Evidence for Surface-Adsorbed Hydrogen Atom on Architectured Palladium Nanoparticles*, J. Am. Chem. Soc. **129**, 6068–6069 (2007).

[54] Y. Gimeno, A. H. Creus, S. Gonzalas, R. C. Salvarezza and A. J. Arvia, *Preparation of 100−160-nm-Sized Branched Palladium Islands with Enhanced Electrocatalytic Properties on HOPG*, Chem. Mater. **13**, 1857–1864 (2001).

[55] W. Pan, X. Zhang, H. Ma and J. Zhang, Electrochemical Synthesis, *Voltammetric Behavior, and Electrocatalytic Activity of Pd Nanoparticles*, J. Phys. Chem. C **112**, 2456–2461 (2008).

[56] R. K. Pandey and V. Lakshminarayanan, *Electro-Oxidation of Formic Acid, Methanol, and Ethanol on Electrodeposited Pd-Polyaniline Nanofiber Films in Acidic and Alkaline Medium*, J. Phys. Chem. C **113**, 21596–21603 (2009).

[57] M. Grden, M. Lukaszewski, G. Jerkiewicz, A. Czerwinski, *Electrochemical Behaviour of Palladium Electrode: Oxidation, Electrodissolution and Ionic Adsorption*, Electrochim. Acta **53**, 7583–7598 (2008).

[58] D. A. J. Rand, R. J. Woods, *The nature of adsorbed oxygen on rhodium, palladium and gold electrodes*, J. Electroanal. Chem. **31**, 29–38 (1970).

[59] C. Du, M. Chen, W. Wang and G. Yin, *Nanoporous PdNi Alloy Nanowires As Highly Active Catalysts for the Electro-Oxidation of Formic Acid*, Appl. Mater. Interfaces **3**, 105–109 (2011).

[60] A. B. A. Nassr, A. Quetschke, E. Koslowski and M. Bron, *Electrocatalytic oxidation of formic acid on Pd/MWCNTs nanocatalysts prepared by the polyol method*, Electrochimica Acta **102**, 202–211 (2013).

[61] T. Maiyalagan, A. B. A. Nassr, T. O. Alaje, M. Bron and K. Scott, *Three-dimensional cubic ordered mesoporous carbon (CMK-8) as highly efficient stable Pd electro-catalyst support for formic acid oxidation*, Journal of Power Sources **211**, 147–153 (2012).

[62] W. Zhou and J. Y. Lee, *Particle Size Effects in Pd-Catalyzed Electrooxidation of Formic Acid*, Journal of Physical Chemistry C **112**, 3789–3793 (2008).

[63] J. Ge, W. Xing, X. Xue, C. Liu, T. Lu, and J. Liao, *Controllable Synthesis of Pd Nanocatalysts for Direct Formic Acid Fuel Cell (DFAFC) Application: From Pd Hollow Nanospheres to Pd Nanoparticle*, J. Phys. Chem. C **111**, 17305–17310 (2007).

[64] V. Celorrio, M. G. Montes de Oca, D. Plana, R. Moliner, M. J. Lázaro, and D. J. Fermín, *Effect of Carbon Supports on Electrocatalytic Reactivity of Au–Pd Core–Shell Nanoparticles*, J. Phys. Chem. C **116** (10), 6275–6282 (2012).

[65] M. Baldauf and D. M. Kolb, *Formic Acid Oxidation on Ultrathin Pd Films on Au(hkl) and Pt(hkl) Electrodes*, J. Phys. Chem. **100**, 11375–11381 (1996).

[66] C. Rice, S. Ha, R. I. Masel, P. Waszczuk, A. Wieckowski, and T. Barnard, *Direct formic acid fuel cells*, J. Power Sources **111**, 83–89 (2002).

[67] H. Meng, S. Sun, J-P. Masse and J-P. Dodelet, *Electrosynthesis of Pd Single-Crystal Nanothorns and Their Application in the Oxidation of Formic Acid*, Chem. Mater. **20**, 6998–7002 (2008).

[68] N. Hoshi, K. Kida, M. Nakamura, M. Nakada and K. Osada, *Structural effects of electrochemical oxidation of formic acid on single crystal electrodes of palladium*, J. Phys. Chem. B **110**, 12480–12484 (2006).

[69] R. K. Pandey and V. Lakshminarayanan, *Electro-Oxidation of Formic Acid, Methanol, and Ethanol on Electrodeposited Pd-Polyaniline Nanofiber Films in Acidic and Alkaline Medium*, J. Phys. Chem. C **113**, 21596–21603 (2009).

[70] K.W. Park, J. H. Choi, B. K. Kwon, S. A. Lee, Y. E. Sung, H. Y. Ha, S. A. Hong, H. H. Kim, and A. Wieckowski, *Chemical and Electronic Effects of Ni in Pt/Ni and Pt/Ru/Ni Alloy Nanoparticles in Methanol Electrooxidation*, J. Phys. Chem. B **106**, 1869–1877 (2002).

[71] A. L. Dicks, *The role of carbon in fuel cells*, Journal of Power Sources **156**, 128–141 (2006).

5 Synthesis and Electrocatalysis of Pt Nanotubes Modified with Ru and Sn

Pt is the most active among metallic catalysts for methanol electrooxidation as described in the previous chapter. However, in addition to its prohibitive costs, Pt is also easily poisoned with CO; an intermediate of methanol oxidation product that adsorbs on the Pt active surface sites, thus diminishing its activity. Hence, for better performance of Pt catalysts, the adsorption of CO needs to be impeded. The addition of Ru to Pt catalyst has been reported to be very effective for diminishing the tendency of Pt to poisoning [1,2]. Furthermore, the addition of Ru allows operating DMFCs at lower potential because Ru in Pt catalyst shifts the onset potential towards lower values [3,4]. A similar effect has been also reported for Sn additions [3-5]. The superior properties of Pt-Ru and Pt-Sn catalysts were attributed to the bi-functional mechanism of methanol oxidation. According to this mechanism oxygen-containing species adsorb on Ru and Sn sites at lower potentials (for example oxygen adsorbs on Ru at 0.2–0.3 V that is lower than on pure Pt surface while on Sn it adsorbs at even lower potentials), and preferentially oxidize the carbonaceous species (CO) adsorbed on Pt sites [6]. Both Ru and Sn promote the oxidation of CO on Pt sites, with Ru being more effective at higher potentials while Sn is more suitable at lower potentials [7]. Moreover, CO oxidation at lower potentials by Ru and Sn is responsible for the lowering of the onset potential of methanol electrooxidation on Pt [6-10]. It has also been postulated that the improved catalytic activity of Ru and Sn modified Pt could lie in the modification of the electronic properties of Pt by these elements which leads to weakening of the

Pt-CO bond [11,12]. The set of reactions describing the bi-functional mechanism can be written as follows [4]:

$$Pt + CH_3OH \rightarrow PtCO_{ads} + 4H^+ + 4e^- \quad (5.1)$$

$$Ru + H_2O \rightarrow RuOH_{ads} + H^+ + e^- \quad (5.2)$$

$$CO_{ads} + OH_{ads} \rightarrow CO_2 + H^+ + e^- \quad (5.3)$$

Although Pt-based binary electrodes, Pt-Ru [3-5,13-21] and Pt-Sn [3-5,21-23] were widely studied for methanol electrooxidation, there are only few reports on the modification of Pt with Ru and Sn submonolayer [4,24,25]. To the best of our knowledge, there are no earlier reports on Ru and Sn modified 1D-Pt nanostructures in the literature.

In present work we employ Pt-NTs electrodes, since they have higher surface area and show better electrocatalytic performance than either platinum nanorods [26] or their thin film analogue [27]. The surface of Pt-NTs electrodes, were subsequently modified with an electrodeposited submonolayers of either Ru or, Sn and we have also investigated a mixture of them. Herein, we report on the effects of these submonolayers on the electrocatalytic activity of the modified Pt-NTs towards methanol electrooxidation.

5.1 Materials and measurement methods

Similar to noble metal nanostructure synthesis in chapter 3, 60 µm thick commercial AAO templates with pore size 200 nm were used to grow Pt-NTs. Again deionized water (R ≥18 MΩ) and chemicals of analytical grade purity were used to prepare electrolytes. All the electrochemical experiments were performed at room temperature with the same electrochemical workstation, IM6e (ZAHNER, Germany) in a standard three electrode cell setup. A Pt mesh and Ag/AgCl (saturated KCl) were used as counter and reference electrodes, respectively. All electrolytes were saturated with nitrogen (N_2) before each electrochemical experiment and all

potentials are referred to the standard hydrogen electrode (SHE). The real surface area (R) of the Pt/Ru-NTs electrode was also determined using the Cu under potential deposition technique [28] for the sake of comparison of the specific activity with some of the results from the literature [16,19]. At first a reference voltammogram was recorded in 0.1 M H_2SO_4 between 0 and 0.95 V at a scan rate of 10 mVs^{-1} and then the same Pt/Ru-NTs electrode was polarized at 0.3 V in an electrolyte containing 0.1 M H_2SO_4 and 2 mM $CuSO_4$ for 150 s to deposit a monolayer of Cu. Finally, a linear voltammetric scan between 0.3 and 0.95 V was performed at 10 mVs^{-1} in the same electrolyte to remove the underpotentially deposited monolayer of Cu. R, the real surface area, was then determined from the following equation:

$$R = \frac{Q}{vc} \tag{5.4.1}$$

Where Q is the integrated area (in V.A) of the Cu stripping peak after subtracting the reference scan in the same potential range, v is the scan rate and c = 420 μCcm^{-2} is the charge density corresponding to the adsorption of a single Cu atom on a surface metal atom [29]. The value of R is 19.25 cm^2 for Pt/Ru-NTs electrode, as determined by this method.

The microstructures of the NTs were examined with a high resolution scanning electron microscope (Ultra Plus, Zeiss, Germany).

5.2 Synthesis of Pt nanotubes modified with Ru, Sn and Ru/Sn

First of all Pt-NTs were electrodeposited in the AAO template as described in chapter 3 and our paper [26]. Briefly, the back side of the AAO template was made conductive by sputtering 20 nm of gold (Au), and then a thin Pt-layer was electroplated from a Pt electrolyte (50 mM H_2PtCl_6) on the sputtered Au to close the template completely. Then Pt-NTs were grown electrochemically from 50 mM H_2PtCl_6 under potentiostatic conditions at –0.1 V for 50 s inside the AAO template and further modification of these Pt-NTs with Ru, Sn and Ru/Sn adatoms was done by following procedure.

The AAO templates containing the Pt-NTs were first bonded to a supporting silicon oxide substrate with an adhesive double sided tape and then NTs were exposed by dissolving AAO template into NaOH (5 %); the samples were subsequently rinsed with distilled water and dried in air. The modification of the Pt-NTs electrodes with submonolayers requires very few ad-atoms to be deposited on the surface of Pt. It is possible by electrodepositing at considerably lower potential that is just above or lower than the standard reduction potentials of the ions (under potential electrodeposition). Therefore, the modified Pt-NTs electrodes were obtained by electrodeposition of submonolayers of Ru and Sn at 0.62 V and 0.1 V respectively. The aqueous electrolytes used for electrodeposition of Ru and Sn are 5 mM $RuCl_3$ and 0.1 mM $SnCl_4.5H_2O$ respectively, each dissolved in 0.5 M H_2SO_4. The time of deposition was 10 and 3 minutes for Ru and Sn respectively. To modify the Pt NTs together with Ru and Sn (Ru/Sn), first Ru and then Sn were deposited on Pt-NTs under the same respective electrodeposition conditions as described above.

Although Ru is electrodeposited in a very small amount (submonolayers), it may be interesting to know its exact mass deposition and coverage, because it is one of the precious metals. However, during the electrodeposition of Ru at a potential positive than 0.60 V, the charge consumed is not exclusively used to deposit the submonolayers of Ru but also due to other side reactions such as the formation of surface Pt-O and underpotential partial reduction of $RuCl_5^{2-}$; which take place under these conditions. Thus, only a small part of the deposition charge is consumed for Ru deposition and exact coverage of Ru ad-atoms cannot be estimated [4].

5.3 Morphology

The morphology of Pt-NTs is illustrated in Figure 5.1. A 50s deposition time was enough to grow self-standing tubular structure inside the AAO template. The tubular morphology forms via nucleation and growth of Pt at the bottom and on the walls of the AAO template that contains sputtered Au to a depth of ~1 μm as described in chapter 3.

Attempts were made to reveal Ru and Sn, via X-ray photoelectron spectroscopy as other methods such as energy dispersive x-ray analysis, did not yield any significant results.

Despite the former method being very sensitive to variations in the surface chemistry, the specific morphology of the nanotubes prevented any meaningful analysis. An indirect proof of the existence of Ru and Sn can therefore be obtained from the electrochemical behavior of the modified nanostructures in comparison to the unmodified Pt-NTs in the following section 5.4.

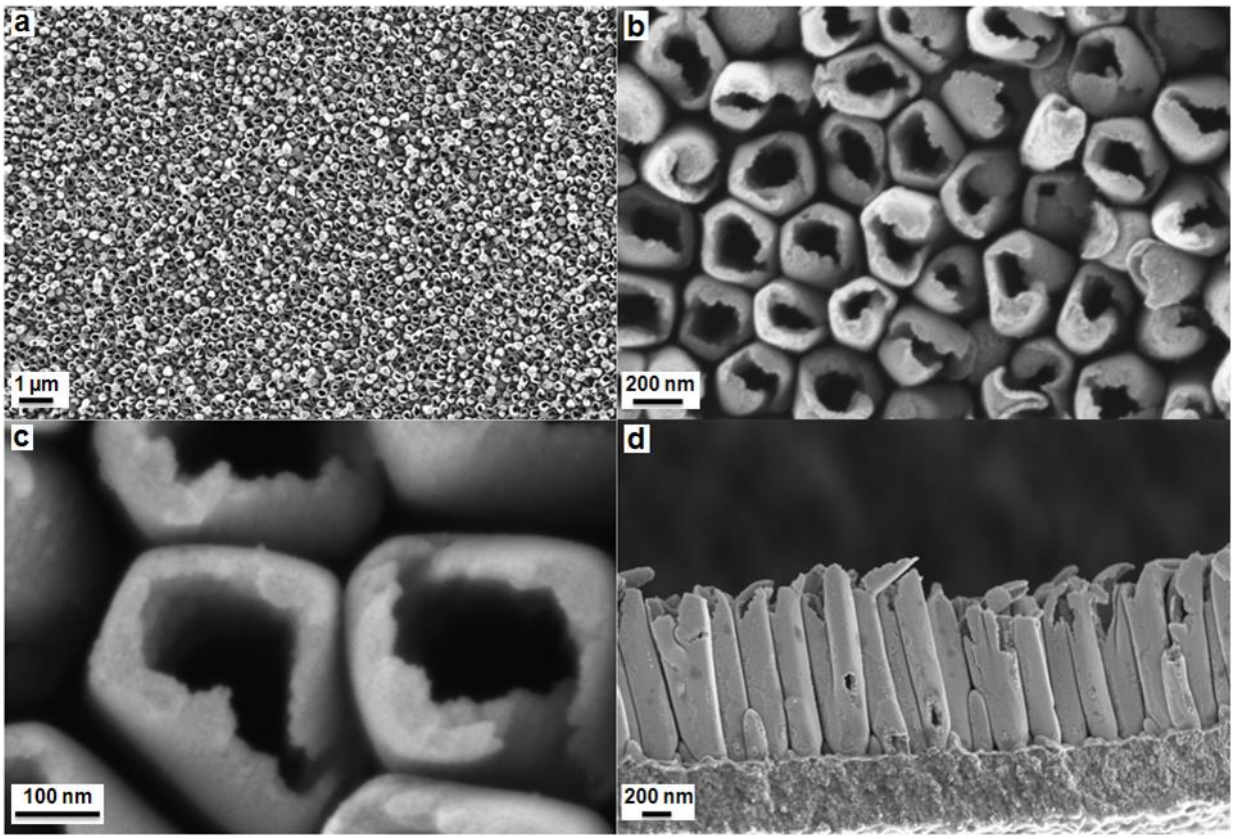

Figure 5.1: SEM images of the Pt-NTs at different magnifications after removal of the AAO template. a, b, c and d represent top and cross-sectional view respectively. These self-standing Pt-NTs electrodes are used further for monolayers deposition of Ru, Sn and Ru/Sn together.

5.4 Electrocatalytic oxidation of methanol on modified and unmodified electrodes

At first, the cyclic voltammograms (CVs) of the electrodes modified with Ru (Pt/Ru-NTs), Sn (Pt/Sn-NTs), and unmodified (Pt-NTs) electrode were obtained in 0.5 M H_2SO_4 at a scan rate 50 mVs^{-1} and shown in Figure 5.2. The peaks between 0 and 0.4 V has been attributed to adsorption/desorption of hydrogen on specific planes of polycrystalline Pt [30]. The hydrogen adsorption/desorption peaks regions (between 0 and 0.4 V) are diminished in the presence of Ru and Sn as shown in Figure 5.2 (dotted lines). This attenuation indicates the presence of ad-atoms of a second metal [4,31,32]. The currents in CVs and chronoamperograms are normalized by the geometrical surface areas of the electrodes.

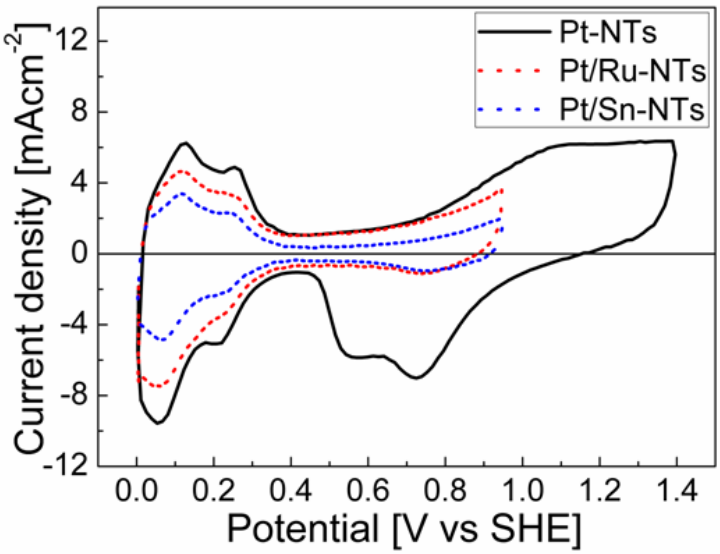

Figure 5.2: CVs obtained in 0.5M H_2SO_4 at a scan rate 50mVs^{-1} of Ru and Sn modified electrodes (red and blue dotted lines), and unmodified Pt-NTs electrode (solid line). The hydrogen adsorption/desorption peaks regions (between 0 and 0.4 V) are diminished in case of modified electrodes which indicates the presence of Ru and Sn.

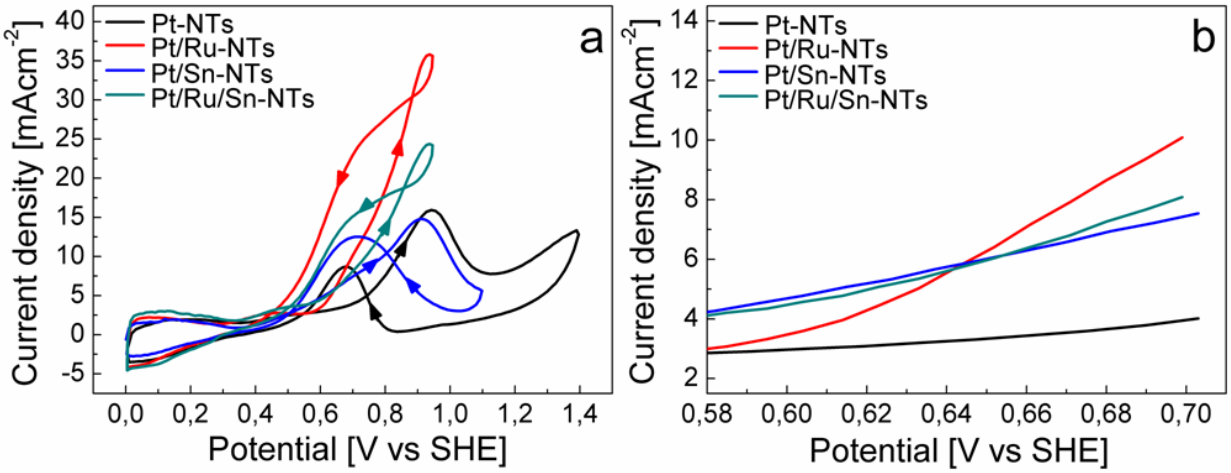

Figure 5.3: (a) CVs obtained in 0.5 M H_2SO_4 + 0.5 M CH_3OH electrolyte at a scan rate of 50 mVs^{-1} show the activity of four electrodes Pt-NTs (black line), Pt/Ru-NTs (red line), Pt/Sn-NTs (blue line) and Pt/Ru/Sn-NTs (green line). (b), is the potential window of (a) between 0.58 and 0.7 V. The currents are normalized by the geometrical surface area of electrodes.

The catalytic activity of ruthenium, tin and ruthenium/tin modified Pt-NTs electrodes are assessed in acidic media and are compared with pure Pt-NTs electrode (Figure 5.3(a) along with some literature results (Table 5.1) on similar systems. This was done by recording CV scans for all the four electrodes in 0.5 M H_2SO_4 + 0.5 M CH_3OH electrolyte at a scan rate 50 mVs^{-1}. The anodic limit for Ru modified electrodes is set to 0.95 V to prevent its dissolution [8]. In forward scan, the peak current represents the oxidation of methanol on the electrode surface while in reverse scan it indicates the oxidation and removal of incompletely oxidized carbonaceous species [33,34].

In terms of maximum peak current density (J_{max}), the Pt/Ru-NTs electrode is superior to all other electrodes with a maximum current density of 36 $mAcm^{-2}$ at 0.93 V, followed by Pt/Ru/Sn-NTs (24 $mAcm^{-2}$ at 0.93 V) and Pt-NTs (16 $mAcm^{-2}$ at 0.94 V), and finally Pt/Sn-NTs (15 $mAcm^{-2}$ at 0.91 V). The onset potential is observed to decrease from 0.74 V for pure Pt-NTs to 0.44 V for Pt/Sn-NTs with intermediate values for Pt/Ru-NTs (0.62 V) and Pt/Ru/Sn-NTs (0.59 V). The shift in the onset potential is more drastic in case of the Pt/Sn-NTs electrode which shows the usefulness of this electrode at lower potentials. Since lower operating potential is favorable for

direct methanol fuel cells (DMFC), a comparison of the activity of the electrodes near the onset potential is depicted in Figure 5.3(b). Up to ~0.64 V the Sn-modified electrodes are superior to the other electrodes in terms of catalytic activity. However, at higher potentials the Pt/Ru-NTs electrode shows substantially higher activity than all the electrodes examined here. These results clearly indicate not only the presence of Ru and Sn but also show that modified Pt-NTs electrodes possess enhanced electrocatalytic activity for methanol oxidation in different potential ranges.

A comparison of Pt/Ru-NTs with similar work from literature [13,16,19] is shown in Table 5.1. Platinum–ruthenium alloy nanowire networks (Pt–Ru NWNs) synthesized by a surfactant assisted soft template method and Pt–Ru black [13] show a somewhat lower activity (in terms of current density J_{geo}, normalized by geometrical surface area) than our Pt/Ru-NTs at the same potential of 0.9 V, although the electrolytes were different (0.1 M $HClO_4$ + 1 M CH_3OH as compared to 0.5 M H_2SO_4 + 0.5 M CH_3OH in our case). Electrodes made of a platinum–ruthenium (Ru 12 atomic %) alloy supported on acid (HNO_3) functionalized carbon (Pt-Ru/C) [16] show superior activity (in terms of current density J_R, normalized by R) than ours at 0.8 V, but our results are better than those obtained on a PtRu alloy (Ru 17 atomic %) NTs, (PtRu-NTs) prepared by electrodeposition on ZnO-NTs sacrificial templates [19], particularly at 0.95 V. The comparison above should, however, be taken cautiously because the results from the literature are for Pt-Ru alloys, and we are dealing with monolayers of Ru adsorbed on Pt. Also the use of carbon to support the active noble metals may have a substantial effect on improving the electrocatalytic properties [35]. Nevertheless the results obtained in this work are highly promising.

To test the long term stability of the modified electrodes corresponding chronoamperograms (current density vs. time at a fixed voltage) were recorded near the onset potential of Pt/Ru-NTs, i.e. at 0.72 V for 1800 s, and are shown in Figure 5.4. Chronoamperogram of unmodified Pt-NTs was not recorded at this potential because of its higher onset potential. All the modified electrodes show a gradual decrease in current density as the methanol is oxidized, and there is no steep decrease which is a good indication of long term stability.

Table 5.1 A comparison of activity made between Pt/Ru-NTs electrode and some recent similar work from literature at different potentials.

Electrode	J_{geo} at 0.9 V [$mAcm^{-2}$]	J_R at 0.8 V [$mAcm^{-2}$]	J_R at 0.95 V [$mAcm^{-2}$]
Pt/Ru-NTs	33	0.41	0.78
Pt-Ru NWNs[a]	30.95	-	-
Pt–Ru black[a]	23.5	-	-
Pt-Ru/C)[b]	-	0.75	-
PtRu-NTs[c]	-	0.38	0.5

[a] Reference [13], [b] Reference [16], [c] Reference [19]

Comparison of the modified electrodes clearly shows that the Pt/Ru-NTs electrode not only has the highest initial current density but also remain superior to the other electrodes for longer time before it converges to the value of Pt/Ru/Sn-NT.

Our results, at the first place indicate that the electrochemical active surface area of Pt-NTs is reduced with the adatoms of Ru and Sn on the surface, which is consistent with the previous literature studies on modification of bulk Pt electrodes with submonolayers of Ru and Sn. Thus, it confirms that the surface modification idea can be applied to nanoscale Pt electrodes. The reduction in surface area was more prominent in case of Sn modified Pt-NTs electrode as compared to Ru modified electrode. Subsequently, these modified Pt-NTs electrodes exhibited differentiated electrocatalytic performance from pure Pt-NTs for methanol electrooxidation in acidic media. The Ru and Sn adatoms affected the electrocatalysis of Pt-NTs in two ways; by changes in peak currents and onset potentials of electrooxidation. Maximum peak current was

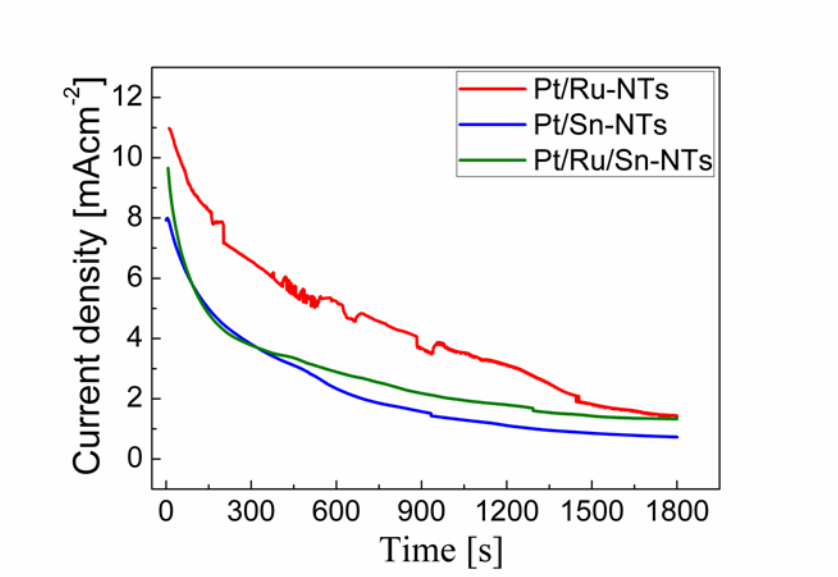

Figure 5.4: Chronoamperograms of Pt/Ru-NTs, Pt/Sn-NTs and Pt/Ru/Sn-NTs electrodes at 0.72 V obtained in 0.5 M H_2SO_4 + 0.5 M CH_3OH for 1800 s. Pt/Ru-NTs electrode shows clearly best performance amongst all the modified electrodes at this potential. The currents are normalized by geometrical surface area of the electrodes.

exhibited by Ru modified Pt-NTs electrode while Sn modified electrode showed minimum peak current during electrooxidation CV cycling. Similarly long term electrocatalytic performance of Ru modified Pt-NTs electrode was best among the tested electrodes in this work. On the other hand, Sn modified Pt-NTs electrode exhibited maximum reduction in the onset potential. Moreover, our modified Pt-NTs exhibited comparable or better current density than similar works from literature, at different potentials. Therefore, we conclude that modified Pt-NTs electrodes have varying catalysis behavior in different potential ranges which are controlled by adatoms of Ru and Sn.

References

[1] S. Mylswamy, C. Y. Wang, R. S. Liu, J. F. Lee, M. J. Tang, J. J. Lee and B. J. Weng, *Anode catalysts for enhanced methanol oxidation: An in situ XANES study of PtRu/C and PtMo/C catalysts*, Chem. Phys. Lett. **412**, 444–448 (2005).

[2] C. Bock, M. A. Blakely and B. MacDougall, *Characteristics of adsorbed CO and CH_3OH oxidation reactions for complex Pt/Ru catalyst systems*, Electrochim. Acta **50**, 2401–2414 (2005).

[3] Y. Morimoto and E. B. Yeager, *Comparison of methanol oxidations on Pt, Pt|Ru and Pt|Sn electrodes*, J. Electroanal. Chem. **444**, 95–100 (1998).

[4] Z. D. Wei, L. L. Li, Y. H. Luo, C. Yan, C. X. Sun, G. Z. Yin and P. K. Shen, *Electrooxidation of Methanol on upd-Ru and upd-Sn Modified Pt Electrodes*, J. Phys. Chem. B **110**, 26055–26061 (2006).

[5] W. T. Napporn, H. Laborde, J. M. lager and C. Lamy, *Electro-oxidation of C1 molecules at Pt-based catalysts highly dispersed into a polymer matrix: effect of the method of preparation*, J. Electroanal. Chem. **404**, 153–159 (1996).

[6] S. Wasmus and A. Küver, *Methanol oxidation and direct methanol fuel cells: a selective review*, J. Electroanal. Chem. **461**, 14–31 (1999).

[7] Y. Morimoto and E. B. Yeager, *CO oxidation on smooth and high area Pt, Pt-Ru and Pt-Sn electrodes*, J. Electroanal. Chem. **441**, 77–81 (1998).

[8] O. A. Petrii, *Pt–Ru electrocatalysts for fuel cells: a representative review*, J. Solid State Electrochem. **12**, 609–642 (2008).

[9] H. A. Gasteiger, N. Markovic´, P. N. Ross, Jr and E. J. Cairns, *Methanol electrooxidation on well-characterized platinum-ruthenium bulk alloys*, J. Phys. Chem. **97**, 12020–12029 (1993).

[10] M. Watanabe and S. Motoo, *Electrocatalysis by ad-atoms: Part II. Enhancement of the oxidation of methanol on platinum by ruthenium ad-atoms*, J. Electroanal. Chem. **60**, 267–273 (1975).

[11] T. Iwasita, F. C. Nart and W. Vielstich, *Over-oxidation of polypyrrole in propylene carbonate, an in situ FTIR study*, Ber. Bunsenges. Phys. Chem. **94**, 1030 (1990).

[12] S. Tillmann, G. Samjeske´, K. A. Friedrich and H. Baltruschat, *The adsorption of Sn on Pt(1 1 1) and its influence on CO adsorption as studied by XPS and FTIR***,** Electrochim. Acta **49**, 73–83 (2003).

[13] B. Li, D. C. Higgins, S. Zhu, H. Li, H. Wang, J. Ma and Z. Chen, *Highly active Pt–Ru nanowire network catalysts for the methanol oxidation reaction*, Catalysis Communications **18**, 51–54 (2012).

[14] H. Wang, L. R. Alden, F. J. DiSalvo, and H. D. Abruna, *Methanol Electrooxidation on PtRu Bulk Alloys and Carbon-Supported PtRu Nanoparticle Catalysts: A Quantitative DEMS Study*, Langmuir **25**, 7725–7735 (2009).

[15] E. Lee, A. Murthy and A. Manthiram, *Comparison of the stabilities and activities of Pt–Ru/C and Pt_3–Sn/C electrocatalysts synthesized by the polyol method for methanol electro-oxidation reaction*, J. Electroanal. Chem. **659**, 168–175 (2011).

[16] J. R. C. Salgado, J. C. S. Fernandes, A. M. Botelho do Rego, A. M. Ferraria, R. G. Duarte and M. G. S. Ferreira, *Pt–Ru nanoparticles supported on functionalized carbon as electrocatalysts for the methanol oxidation*, Electrochim. Acta **56**, 8509–8518 (2011).

[17] P. Waszczuk, A. Wieckowski, P. Zelenay, S. Gottesfeld, C. Coutanceau, J. M. Leger and C. Lamy, *Adsorption of CO poison on fuel cell nanoparticle electrodes from methanol solutions: a radioactive labeling study*, J. Electroanal. Chem. **511**, 55–64 (2001).

[18] T. Iwasita, H. Hoster, A. John-Anacker, W. F. Lin and W. Vielstich, *Methanol Oxidation on PtRu Electrodes. Influence of Surface Structure and Pt−Ru Atom Distribution*, Langmuir **16**, 522–529 (2000).

[19] R. Minch and M. Es-Souni, *On-substrate, self-standing hollow-wall Pt and PtRu-nanotubes and their electrocatalytic behavior*, Chem. Commun. **47**, 6284–6286 (2011).

[20] H. Laborde, J-M. Leger and C. Lamy, *Electrocatalytic oxidation of methanol and C1 molecules on highly dispersed electrodes Part II: Platinum-ruthenium in polyaniline*, J. Appl. Electrochem. **24**, 1019–1027 (1994).

[21] K. Wang, H. A. Gasteiger, N. M. Markovic and P. N. Ross Jr, *On the reaction pathway for methanol and carbon monoxide electrooxidation on Pt-Sn alloy versus Pt-Ru alloy surfaces*, Electrochim. Acta **41**, 2587–2593 (1996).

[22] E. Antolinia and E. R. Gonzalez, *Effect of synthesis method and structural characteristics of Pt–Sn fuel cell catalysts on the electro-oxidation of CH_3OH and CH_3CH_2OH in acid medium*, Catalysis Today **160**, 28–38 (2011).

[23] A. O. Neto, R. R. Dias, M. M. Tusi, M. Linardi and E. V. Spinace, *Electro-oxidation of methanol and ethanol using PtRu/C, PtSn/C and PtSnRu/C electrocatalysts prepared by an alcohol-reduction process*, J. Power Sources **166**, 87–91 (2007).

[24] Y. Ishikawa, M-S. Liao and C. R. Cabrera, *Oxidation of methanol on platinum, ruthenium and mixed Pt–M metals (M= Ru, Sn): a theoretical study*, Surf. Sci. **463**, 66–80 (2000).

[25] M. Watanabe, Y. Furuuchi and S. Motoo, *Electrocatalysis by AD-atoms: Part XIII. Preparation of ad-electrodes with tin ad-atoms for methanol, formaldehyde and formic acid fuel cells*, J. Electroanal. Chem. **191**, 367–375 (1985).

[26] F. I. Dar, S. Habouti, R. Minch, M. Dietze and M. Es-Souni, *Morphology control of 1D noble metal nano/heterostructures towards multi-functionality*, J. Mater. Chem. **22**, 8671–8679 (2012).

[27] J. N. Tiwari, F. M. Pan and K-L. Lin, *Facile approach to the synthesis of 3D platinum nanoflowers and their electrochemical characteristics*, New J. Chem. **33**, 1482–1485 (2009).

[28] C. L. Green and A. Kucernak, *Determination of the platinum and ruthenium surface areas in platinum-ruthenium alloy electrocatalysts by underpotential deposition of copper. I. Unsupported catalysts*, J. Phys. Chem. B **106**, 1036–1047 (2002).

[29] S. A. S. Machado, A. A. Tanaka and E. R. Gonzalez, *Underpotential deposition of copper and its influence in the oxygen reduction on platinum*, Electrochim. Acta **36**, 1325–1331 (1991).

[30] K. Yamamoto, D. M. Kolb, R. Kötz and G. Lehmpfuhl, *Hydrogen adsorption and oxide formation on platinum single crystal electrodes*, J. Electroanal. Chem. **96**, 233–239 (1979).

[31] A-C. Boucher and N. Alonso-Vante, *Structural and Electrochemical Studies of Pt−Sn Nanoparticulate Catalysts*, Langmuir **19**, 10885–10891 (2003).

[32] D. M. Dos Anjos, F. Hahn, J –M. Leger, K. B. Kokoh and G. Tremiliosi-Filho, *Ethanol Electrooxidation on Pt-Sn and Pt-Sn-W Bulk Alloys*, J. Braz. Chem. Soc. **19**, 795–802 (2008).

[33] J. Prabhuram and R. Manoharan, *Investigation of methanol oxidation on unsupported platinum electrodes in strong alkali and strong acid*, J. Power Sources **74**, 54–61 (1998).

[34] R. Manoharan and J. B. Goodenough, *Methanol oxidation in acid on ordered NiTi*, J. Mater. Chem. **2**, 875–887 (1992).

[35] A. L. Dicks, *The role of carbon in fuel cells*, J. Power Sources **156**, 128–141 (2006).

6 Morphology Controlled Synthesis and Supercapacitance of 1D NiO Nanostructures

This chapter is based on our published article [1] in which we aim at showing that the concept developed above, for morphology and chemistry control of 1D nanostructures (NSs) to enhance their electrocatalysis performance can easily be extended to other NSs and devices. To remain in the domain of energy materials we present in the following our work on controlling the pseudocapacitance performance of NiO via morphology control.

Electrochemical capacitors are also called supercapacitors and depending upon their energy storage modes; can be categorized as electrical double layer capacitors and redox or pseudocapacitors. The electrical double layer is formed due to charge separation on both sides of the interface in electrical double layer capacitors and current arises because of the rearrangement of the charges when voltage is applied [2,3]. While in pseudocapacitors, the source of charge is the fast and reversible reduction and oxidation (redox) reaction at the interface of the electrode and electrolyte which arises due to the change in oxidation state of the capacitor material [4-6]. The redox capacitors have superior supercapacitance properties than the double layer capacitors [7].

NiO-based NSs and thin films have frequently found their application as electrode material for electrochemical power sources that is, in lithium ion batteries and fuel cells [8-10], electrochromic films [11,12], gas sensors [13] and supercapacitors (pseudocapacitors) [11,14].

NiO is a low cost material as compare to RuO_2, furthermore it is environmentally benign and can be processed easily with different methods. Therefore, it constantly attracts notable research interests for high performance pseudocapacitor applications [11,14-16].

Factors such as ion diffusion kinetics and electronic conductivity determines the rate capability (charge-discharge) of the pseudocapacitors [17], therefore, the electrode materials made of nano/micro hierarchical porous structures are considered most appropriate in energy storage devices. The 1D NSs are even more suitable because of their available short transport pathways for charges [18,19], making them very good candidate for supercapacitor applications. The easy diffusion paths for charges are critical for better performance, which are efficiently provided by the high aspect ratio of 1D NSs, while on the other hand good mechanical stability is achieved by low aspect ratio NSs [20]. Thus morphology of the NSs plays a crucial role in determining the supercapacitance performance of the electrode.

This chapter presents the template assisted synthesis of 1D-NiO supported nanostructures (NSs) starting from Ni-nanotubes (NT) that are oxidized to yield 1D NiO-NSs. We demonstrate here the morphology control of NiO-NSs through annealing time, instead of electrodeposition time as was done for noble metal nanostructures in this work. By judicious choice of annealing temperature and time the morphology of Ni-NT could be tuned from NiO-NT to NiO-NR thus allowing investigating morphological effects on energy storage capability (supercapacitance).

6.1 Materials and measurement methods

Again similar to noble metal nanostructures a commercial AAO template (60 µm thick with 200 nm pore size) was used as sacrificial template for synthesis of NiO nanostructures and chemicals of analytical grade purity were used together with de-ionized water ($\geq 18\mathrm{M}\Omega$) to prepare aqueous solutions. The electrochemical experiments were performed at room temperature in a standard three electrode cell. The electrodeposition and CVs were made by electrochemical workstation, (ZAHNER IM6e, Germany) and charging-discharging tests were performed by Source Meter, 2400 (KEITHLEY). Before each electrochemical experiment, N_2 was bubbled in

the electrolyte for 15 minutes. The electrochemical experiments were conducted on a minimum of 3 to 5 samples each. A Pt mesh and Hydroflex (H_2 reference electrode) were used as counter and reference electrodes, respectively. All potentials are referred to the standard hydrogen electrode (SHE). The microstructure and morphology of the nanostructures were characterized with the same high resolution scanning electron microscope used for noble metal nanostructures in this work. X-ray diffraction data was obtained in grazing incident geometry with fixed angle of 1.5° and 0.05° step using monochromatic Cu $K\alpha$ radiation ($\lambda = 1.5418$Å).

6.2 Synthesis of NiO nanostructures

The NiO-NSs are prepared by two steps. At first Ni-NTs are synthesized with the help of AAO template by electrodeposition and then in the second step these Ni-NTs are annealed inside the AAO template. The controlled annealing not only oxidized the Ni to NiO but also defined and controlled the morphology from NTs to NRs. The two steps synthesis of NiO-NTs and NiO-NRs is described below.

6.2.1 Synthesis of Ni nanotubes

The process steps and schematics for preparing the nanostructures with the help of AAO template by electrochemical method are detailed in our paper [21] and chapter 3; and are described briefly below with necessary changes of electrolyte and electrodeposition conditions.

One side of the AAO template was sputtered with 20 nm Au to make it conductive. Subsequently a 350 nm thick Ni-layer was electroplated on the sputtered Au to close the AAO template completely and to provide support to NSs to be built on it, from an electrolyte containing; 310 gL^{-1} $NiSO_4.7H_2O$, 50 gL^{-1} $NiCl_2.6H_2O$ and 40 gL^{-1} H_3BO_3. Then Ni nanotubes (Ni-NTs) were grown electrochemically from the identical electrolyte (310 gL^{-1} $NiSO_4.7H_2O$, 50 gL^{-1} $NiCl_2.6H_2O$ and 40 gL^{-1} H_3BO_3) via bottom up approach under potentiostatic conditions at -0.9 V for 50s. The selected deposition conditions allowed the processing of Ni-NTs. These

synthesized Ni-NTs contained in AAO templates, were washed several times with distilled water and dried in air. Three cracks free Ni-NTs samples (samples 1, 2 and 3) were selected for further processing (annealing) and electrochemical experiments, out of the several samples prepared by the procedure described above.

6.2.2 Synthesis of NiO nanotubes and nanorods

Out of the three samples prepared above (samples 1, 2 and 3), sample 1 was kept at room temperature (~ 20 °C) without annealing it. Sample 2 and 3 were annealed in air within the AAO template, from room temperature to 450 °C. The heating rate was 400 K per hour and both the

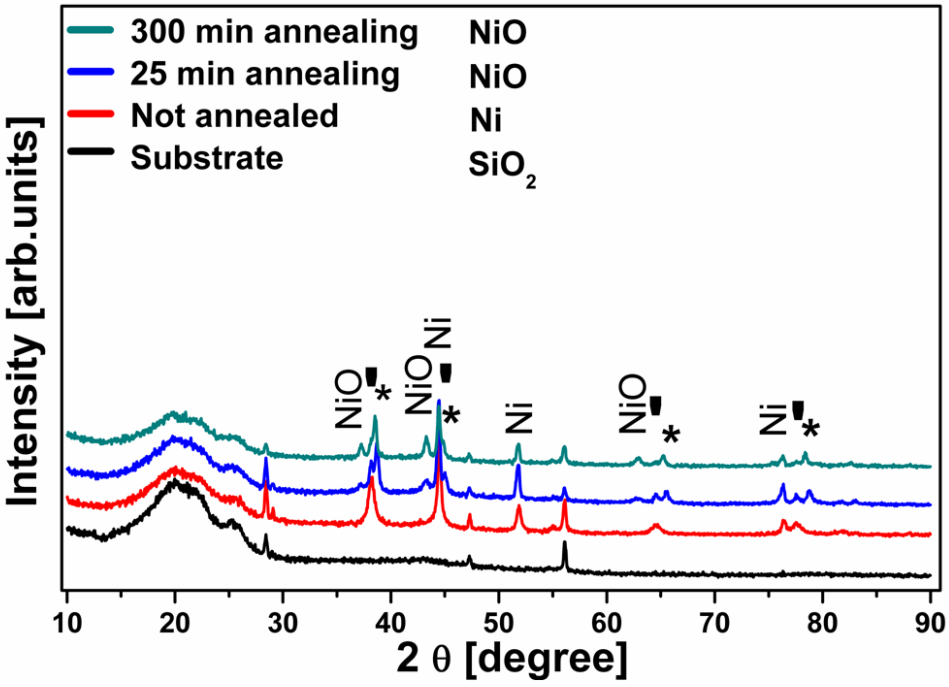

Figure 6.1: XRD patterns of the non-annealed (sample 1) and annealed samples (samples 2 and 3). The patterns are shifted vertically for clarity. The annealed samples show the presence of NiO peaks. The reflexes of Ni are still observed and arise from the incomplete oxidation of the Ni supporting layer. The stars and tick marks denote the Au-Ni alloy and Au, respectively [1] - Reproduced by permission of SpringerOpen.

samples (2 and 3) were kept at final temperature (450 °C) for 25 and 300 min respectively. Both of the annealed samples were cooled down to room temperature in air and out of the furnace. Subsequently all the three samples were glued to SiO_2 supporting substrate with non-conductive and double sided adhesion tape, before dissolving the AAO template with 5% NaOH.

A Ni film sample was also prepared to estimate the contribution of the supporting Ni layer to the capacitance of NSs, For this purpose Ni is electrodeposited on Au sputtered SiO_2 substrate under the identical electrodeposition and annealing conditions.

6.3 Structure and morphology

Figure 6.1 shows the XRD patterns of the non-annealed sample 1 (Ni) and annealed samples 2 and 3 (NiO) NSs synthesized and annealed under the procedure described above. The NiO (cubic, NaCl structure) peaks for annealed NiO NSs (sample 2 and 3) become more prominent with increased annealing time. The reason behind this is the increasing oxide thickness along with enhanced crystal orientation, with the increasing annealing time. The mean grain sizes calculated using the Scherrer equation and the (200) reflection at 43.3°, are 12.8 and 19.4 nm for sample 2 and sample 3, respectively. Ni together with sputtered Au forms Au-Ni binary alloy at the annealing temperature (450 °C) which is indicated by the peaks with star (*). To estimate the chemical composition of this Au-Ni alloy, Vegard's law was applied using the peak positions and lattice constants of a = 4.0789 Å for Au and a = 3.5238 Å for Ni. It shows that the Au-Ni alloy in sample 2 (25 min annealing) is composed of 90 at. % Au-10 at. % Ni and sample 3 (300 min annealing) has alloy with 93 at. % Au-7 at. % Ni.

6.3.1 Magnitude of oxidation

From the XRD spectrum, it is clear that metallic Ni dominates; therefore, it is necessary to estimate the magnitude of oxidation. For this purpose we utilized the already published Ni oxidation data, which shows a parabolic law in a wide range of temperatures [22]. Through

extrapolation and considering the surface area of 1D morphology, the magnitude of oxidation is calculated as follows from our work [1] - Reproduced by permission of SpringerOpen.

"The Ni follows a parabolic growth law of oxidation which is expressed by the following Equation:

$$M^2 = K_p \times \Theta \tag{6.3.1}$$

Where M is the weight gain per unit area, Θ the time of exposure (s) and K_p the parabolic rate constant usually given in $g^2\ cm^{-4}\ s^{-1}$.

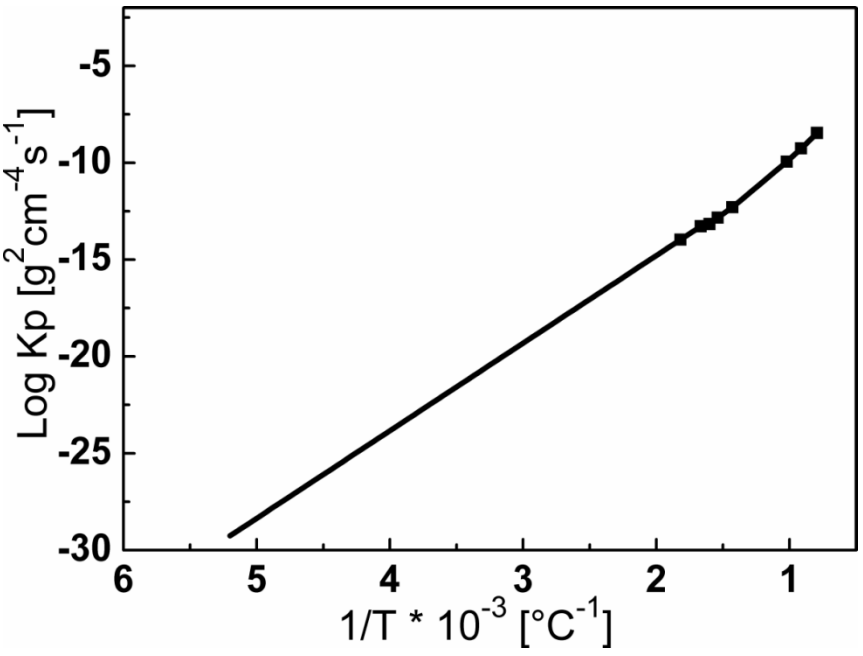

Figure 6.2: The plot of Log K_p versus 1/T (T is temperature in °C). The K_p values for the temperature range from 1260 to 550 °C have been taken from literature [22] and we extrapolate them to 190 °C [1] - Reproduced by permission of SpringerOpen.

The magnitude of oxidation is estimated by extrapolating the oxidation data for high purity Ni (> 99.95%) given in reference [22] to our temperature, in Figure 6.2.

The K_p values for the temperature range from 1260 to 550 °C have been taken from reference [22] and we extrapolate them to 190 °C. From this plot the K_p value at 450 °C is 1.616×10^{-16} $g^2cm^{-4}s^{-1}$.

As sample 2 is oxidized for 1500 s (25 min) at 450 °C thus $K_p \times \Theta$ is 2.424×10^{-13} g^2cm^{-4}. And the value of M is 4.924×10^{-7} gcm^{-2}.

Similarly, for sample 3, oxidized for 18000 s (300 min) at the same temperature, the calculated value of M is 1.706×10^{-6} gcm^{-2}.

Moreover, we also calculated the M values for temperature range from 200 to 445°C because we gradually heated the furnace at a heating rate of 400 K per hour to reach 450 °C after placing the samples in the furnace. For this purpose the M values are calculated at temperatures, 445, 440, 435, 430, 425, 420, 415, 410, 405, 400, 395, 390, 385, 380, 350, 320, 290, 250 and 200 °C for the corresponding times which is required to reach the next temperature as shown in Table 6.1. Below 200 °C the contribution of M values in oxidation is negligible. The sum of M values in the temperature range 445 to 200 °C (5.195×10^{-7} gcm^{-2}) is added to the corresponding M value for oxidation at 450 °C for sample 2 and 3.

Table 6.1 Weight gain per unit surface area (M) calculated by parabolic growth law at temperatures between 445 and 200 °C [1] - Reproduced by permission of SpringerOpen.

Temperature [°C]	Time [s]	M [gcm^{-2}]
445	45	8.445×10^{-8}
440	45	6.864×10^{-8}
435	45	6.786×10^{-8}
430	45	5.328×10^{-8}

425	45	4.2324×10^{-8}
420	45	3.686×10^{-8}
415	45	3.316×10^{-8}
410	45	2.868×10^{-8}
405	45	2.435×10^{-8}
400	45	1.935×10^{-8}
395	45	1.665×10^{-8}
390	45	1.468×10^{-8}
385	45	1.221×10^{-8}
380	45	9.922×10^{-9}
350	270	7.339×10^{-9}
320	270	1.899×10^{-9}
290	270	3.594×10^{-10}
250	360	2.388×10^{-11}
200	450	1.338×10^{-13}

Thus total calculated weight gain per unit area (M_c) is 1.012×10^{-6} gcm^{-2} for sample 2 and 2.225×10^{-6} gcm^{-2} for sample 3.

The mass of Ni and surface area of both the samples described above were calculated to find the weight gain per unit area considering theoretical 100% oxidation (M_t). The mass of Ni is calculated from the charge deposited during electrodeposition of nanostructures, thus mass of

sample 2 is 18.551 × 10^{-6} g for 0.22 cm^2 geometrical area (G) and sample 3 has mass of 16.141 × 10^{-6} g for 0.20 cm^2 geometrical area.

The surface area (S) of the cylindrically shaped nanostructure electrode is calculated as follows:

$$S = \left(2\pi Rh + 2\pi rh + 2\pi R^2\right) \times G \times D \tag{6.3.2}$$

Where, D is the density of the AAO pores, 1 × 10^9 cm^{-2}, G is the geometrical area, R the outer radius of AAO pores, 125 nm (average outer diameter is 250 nm), r the inner radius, 75 nm (Initial average wall thickness of nanostructures after deposition is 50 nm, thus inner diameter is 150 nm) and h the average height of the nanostructures, 1000 nm.

The calculated S for sample 2 and 3 are 2.981 and 2.710 cm^2 respectively. The weight of Ni per unit area is 6.223 × 10^{-6} gcm^{-2} for sample 2 and 5.956 × 10^{-6} gcm^{-2} for sample 3.

Assuming a 100 % oxidation of Ni in sample 2 and sample 3, the total weight gain (M_t) is calculated as follows:

Number of moles of NiO after oxidation = Number of moles of Ni before oxidation

$$\text{Weight of NiO} = \frac{\text{weight of Ni (g)} \times \text{Molecular weight of NiO } (74.71\ \text{g mole}^{-1})}{\text{Atomic weight of Ni } (58.71\ \text{g mole}^{-1})} \tag{6.3.3}$$

The total weights of NiO in sample 2 and 3 are 23.607 × 10^{-6} and 20.540 × 10^{-6} g respectively and the weight gains for sample 2 and 3 are 5.056 × 10^{-6} and 4.399 × 10^{-6} g respectively for theoretical 100 % oxidation. It follows that the weight gain per unit surface area S should be 1.696 × 10^{-6} and 1.623 × 10^{-6} gcm^{-2} for sample 2 and 3, respectively. The above calculated value of M_c is 60% of M_t for sample 2 and M_c for sample 3 is higher than M_t which let us infer that it is completely oxidized. The mass of active material (NiO) is calculated from this percentage oxidation values. Thus masses of active material (NiO) in sample 2 and 3 are 14.131 and 20.539 µg respectively. Similarly, calculated NiO mass in supporting film is 15.655 µg."

The morphology of the nanostructures obtained is shown in Figure 6.3. The non-annealed Sample 1 (Figure 6.3a and b) shows Ni-NTs. These form via nucleation and growth at the pore

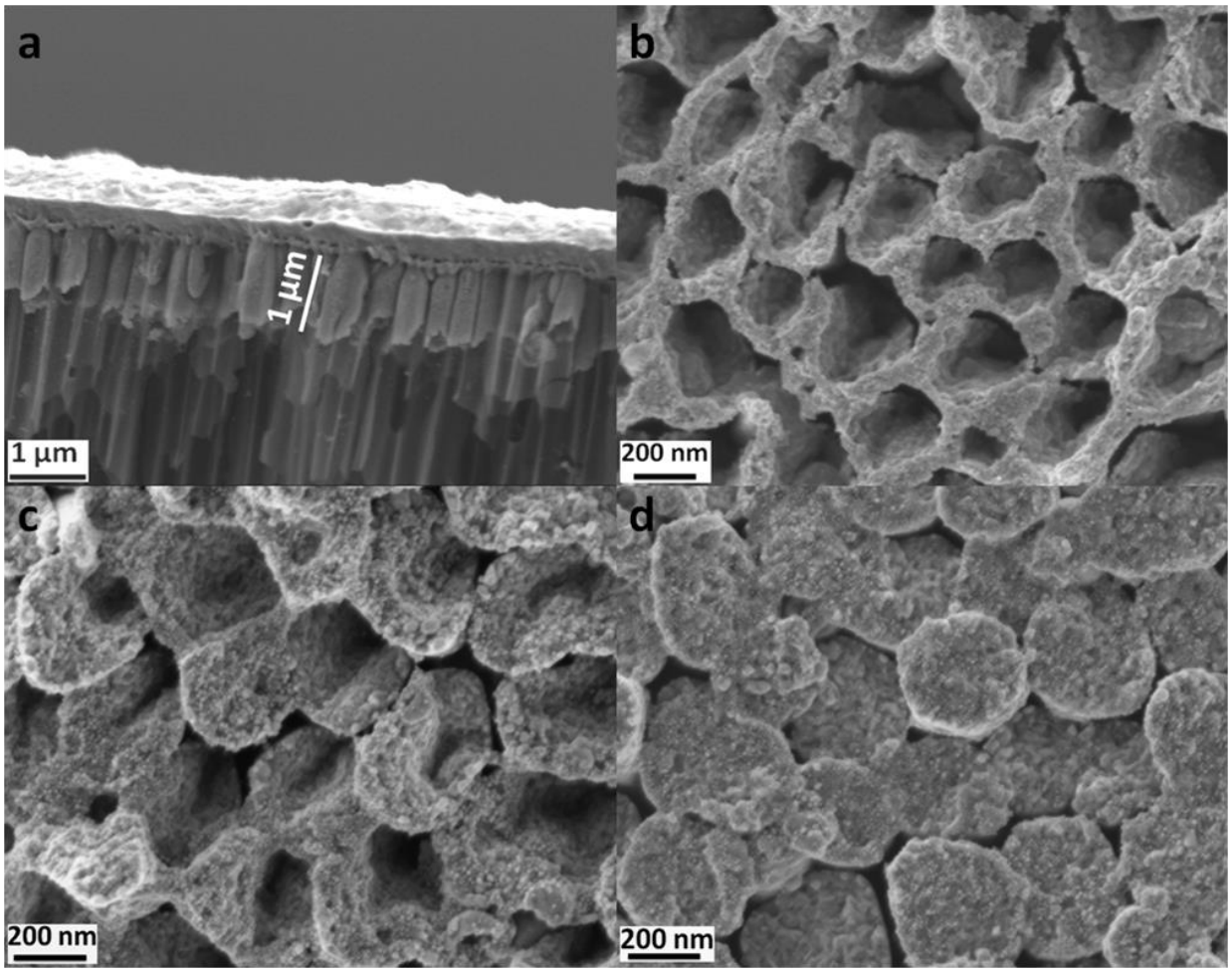

Figure 6.3: SEM images of (a) Cross-sectional (inside AAO template) and (b) top views of the as-prepared Ni-NTs (non-annealed sample 1). (c) Wall thickening after 25-min annealing (sample 2). (d) The complete closure of walls yielding NRs morphology after 300-min annealing (sample 3) [1] - Reproduced by permission of SpringerOpen.

walls because of the presence of an extremely thin Au-layer (see the experimental section of previous chapter and our paper [21]). Ni is optimally deposited for 50s.

Annealing oxidizes the Ni to NiO, however, oxide layer only nucleates and grows on exposed inside walls, in contrast to non-exposed outside walls (covered with AAO template) where oxide growth is not expected. The advancing oxide layer thickens the walls in the direction of the inner tube diameter which suggests that Ni species diffuses outside towards oxygen ions. Complete

oxidation of Ni requires longer time, therefore, shorter time leads to formation of oxide scale on non- oxidized Ni inner layer (see also the XRD results and magnitude of oxidation above in this section).

Sample 2 is the case of incomplete oxidation (Figure 6.3c; 25 min annealing). In case of sample 3 (300 min annealing), longer annealing time causes complete closure of the NTs, that is NRs morphology is formed because of the advancing oxide layer volume, as shown in Figure 6.3d.

6.4 Electrochemical characterization

To measure the pseudocapacitance of the NiO NT and NR electrodes, cyclic voltammograms (CVs) were recorded in an aqueous electrolyte containing 1 M KOH between 0.35 and 0.85 V at different scan rates. Charge-discharge behavior at different current densities and long term cycling stability were tested in 1M KOH. The measured capacitances of the electrodes were then compared with each other to analyze the effect of morphology on the performance and with some results of similar work from literature.

6.4.1 CV curves of NiO nanostructures

Figure 6.4 shows the CV curves of the NiO-NSs (NiO-NT and NiO-NR) that were recorded at various scan rates (5, 10, 25, 50 and 100 mVs^{-1}) in a potential window of 0.5 V (between 0.35 and 0.85 V) in 1 M KOH aqueous solution. The two strong peaks in anodic and cathodic direction correspond to the faradic redox reaction taking place at the NiO/electrolyte interface. The redox reaction involves ionic and electronic transport, expressed as follows [23,24]:

$$NiO + OH^- \leftrightarrow NiOOH + e^- \tag{6.4.1}$$

Although intensity of the peaks changes with the scan rates but shapes of the anodic and cathodic curves remains similar and profile of the CVs indicates that the redox reaction is reversible [25].

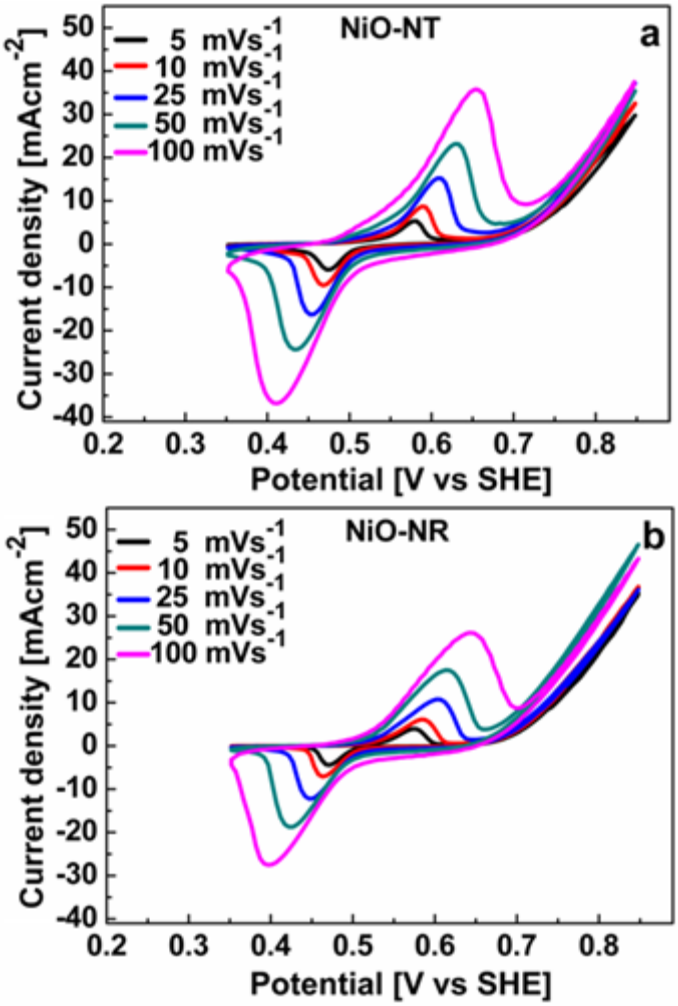

Figure 6.4: CVs of nanostructures. (a) NiO-NT and (b) NiO-NR electrodes in 1 M KOH at different scan rates in a potential window of 0.5 V [1] - Reproduced by permission of SpringerOpen.

The increase in peak current density with the scan rate is due to the diffusion limited nature of the redox reaction and efficiency of the reaction kinetic and transport rate is curtailed at higher scan rate. In redox reaction (equation 6.4.1) there is an exchange of anions with the interface of electrolyte and electrode which is a slow and rate limiting process, and at higher scan rate diffusion layer thickness is smaller [26]. In this way, electrode surface is not fully utilized that brings down the resistivity and increases the current density which also implies the pseudocapacitive behavior of the NiO-nanostructures [25].

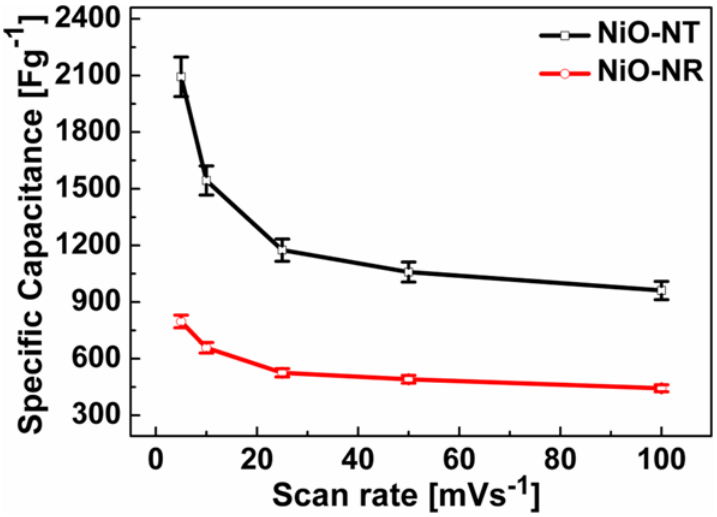

Figure 6.5: The plot of the specific capacitance versus scan rate. The dependence of the specific capacitance on the scan rate is shown for the NiO-NT and NiO-NR electrodes [1] - Reproduced by permission of SpringerOpen.

There is a shift in the position of the anodic and cathodic peaks towards higher and lower potentials, respectively, with increasing scan rates (Figure 6.4). It again indicates the inefficiency of diffusion rate to keep pace with electronic neutralization in the redox reaction [27].

The specific capacitances were calculated from the CVs using the following equation [28,29]:

$$C = \frac{I}{2.V.s.m} \tag{6.4.2}$$

where C is the specific capacitance (Fg^{-1}), I the integrated area (VA) of the CV curve in one complete cycle, V the potential window (V), s the scan rate (Vs^{-1}) and m is the mass (g) of NiO, which is calculated using the oxidized Ni-mass % described above, i.e. 60 % for the NT and 100 % for the NR (See section 6.3.1; "Magnitude of oxidation").

Figure 6.5 shows clearly the strong dependence of the capacitance on the scan rate, that is, it decreases with the increasing scan rate as discussed above. The error bars corresponds to the standard deviation in the mass; 5 % (0.935 µg) and 4.2 % (0.854 µg) for NiO-NT and NiO-NR respectively.

Table 6.2 shows the comparison of specific capacitances of our NSs with one of the recent literature work [16] under similar conditions of scan rates and electrolyte (1 M KOH). The specific capacitances values given here are the ones obtained at slower scan rate, because it represents the maximum (nearly complete) utilization of the electrode [30] through better penetration of ions that is diffusion limited [31]. The comparison in Table 6.2 shows that our NiO-NT sample has highest specific capacitance with mean value of 2093 Fg^{-1} at 5 mVs^{-1}, on the other hand, our NiO-NR sample is characterized with smaller specific capacitance than NiO nano-porous films [16], except at 100 mVs^{-1}. The specific capacitance of the NiO-NT sample not only tops the compared NSs but is also highest among the literature reports for NiO NSs so far, and reaches near the theoretical value of approximately 2584 F/g [32]. This is attributed to the nano crystallinity of the NiO structure synthesized in our work and the high surface area of the 1D NT structure which makes sure the efficient contact with the electrolyte.

6.4.1.1 CV curves of NiO-Film

Obviously one can imagine that the Ni supporting layer would also have oxidized along with Ni nanostructures and question can arise about its contribution to the measured capacitance of the NiO-NSs. However, we do not expect any substantial contribution from supporting NiO layer, because a negligible fraction of the Ni-supporting layer can be thought to be oxidized due to very small exposed area available in between the high density of the NSs including the AAO template; Moreover, even if the completely oxidized layer is present, the most of its area is covered with NSs and not available to electrolyte.

To measure and estimate the maximum contribution to capacitance from the underlying supporting NiO-Film, we electrodeposited a Ni layer of the same thickness on Au sputtered SiO_2 and subsequently annealed it under the same conditions as for NiO-NSs. The magnitude of oxidation for this NiO-Film is determined by using the same procedure as for Ni-NSs above. The CVs of the NiO-Film are made in similar electrolyte (1 M KOH) and redox parts of the CV curves are shown in the inset in Figure 6.6. The capacitances calculated from CVs are also shown at different scan rates as main part of the Figure 6.6. These specific capacitances were

Table 6.2 Comparison of capacitance. The NiO-NT and NiO-NR prepared in our work are compared with one of the literature works [16] recently published, [1] - Reproduced by permission of SpringerOpen.

Scan rate [mVs^{-1}]	Specific Capacitance [Fg^{-1}]		
	NiO- NR	NiO-NT	NiO-Nano porous film[a]
5	797	2093	1208
10	658	1544	940
25	526	1175	748
50	491	1059	590
100	443	961	417

[a] [Reference 16]

used to estimate the maximum contribution of the underlying supporting NiO-layer to the capacitance of the nanostructures.

The effective exposed area (to the electrolyte) of the supporting layer is very small, that is ~2 % (calculated from average distance of ~50 nm between two consecutive AAO channels) of the nanostructures considering the average diameter (250 nm) and density (1×10^9 cm^{-2}) of the pores. Further, only a small fraction of NiO (0.37%) is calculated for the Ni-Film. It means negligible amount of the underlying Ni-layer is oxidized, which explains the dominance of the Ni peaks in the XRD patterns. The maximum capacitance of the NiO-film was found to be 223 Fg^{-1} at 5 mVs^{-1} scan rate (Figure 6.6). This value of specific capacitance is for fully utilized surface of NiO-Film. But as outlined above only a small fraction of the film is contributing to

capacitance. It let us infer that the capacitances measured capacitances represents only the contribution of our 1D NSs.

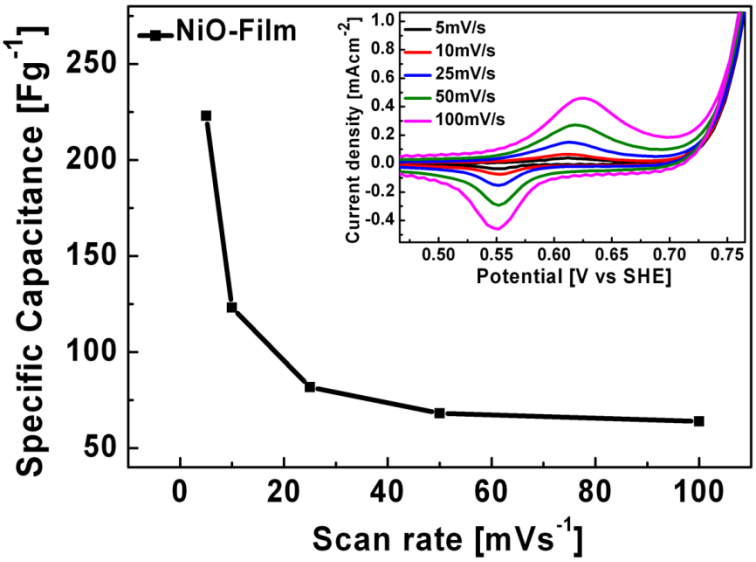

Figure 6.6: Specific capacitance of the bare NiO-film at different scan rates. The inset shows the redox part of the CV curves made in 1 M KOH [1] - Reproduced by permission of SpringerOpen.

6.4.2 Galvanostatic charging-discharging tests of NiO nanostructures

Figure 6.7a and b displays the galvanostatic charging-discharging examined at different constant current densities for both the NiO-NSs samples (NT and NR) synthesized in this work. The non-linearity of the charge-discharge curves of both NiO-NSs points out again their pseudocapacitive behavior [6].

The cyclic charging-discharging tests were further extended for longer period, because long-term stability is a significant feature of a capacitor structure. Thus, 500 cycles were performed on NiO-NT and NiO-NR samples at constant current densities of 125 Ag^{-1} and 80 Ag^{-1}, respectively as shown in Figure 6.8. Capacity retention of nearly 100% is exhibited by both the NiO-NSs.

Our NSs exhibited splendid supercapacitor properties such as high capacitance value and long term capacity retention. Particularly, NiO-NT structure excels the reported results so far on NiO supercapacitors. For example the maximum specific capacitance values, attained by different morphologies of NiO-NSs, such as nanofibers [33], nanoflowers [34], nanoflakes [15], porous structures [35], nanoporous film [16] and nanorod arrays [36], lie between 336 to 2018 Fg^{-1} (the latter value is for NiO-NR arrays on Ni foam, and is quite higher than achieved for our NiO-NR due to difference in structural dimensions).

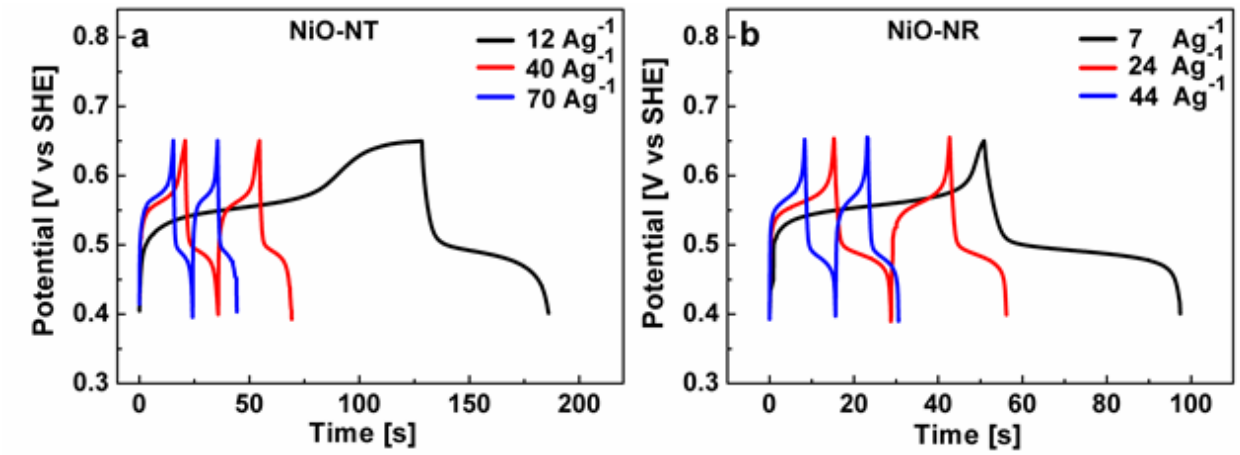

Figure 6.7: The charge–discharge tests of (a) NiO-NT and (b) NiO-NR electrodes in 1 M KOH at different constant current densities, are shown [1] - Reproduced by permission of SpringerOpen.

As described above that the contributing factors for efficient redox reaction and hence pseudocapacitor performance, are nanocrystalline grain size and high surface area of the tubular structure of the NiO-NT sample which enables an intimate contact between electrode and electrolyte and provides a large density of necessary OH^- ions for redox reaction. Moreover, long term stability in charging-discharging cycles is due to chemical stability and robust nature of the NiO-NSs synthesized here in this work.

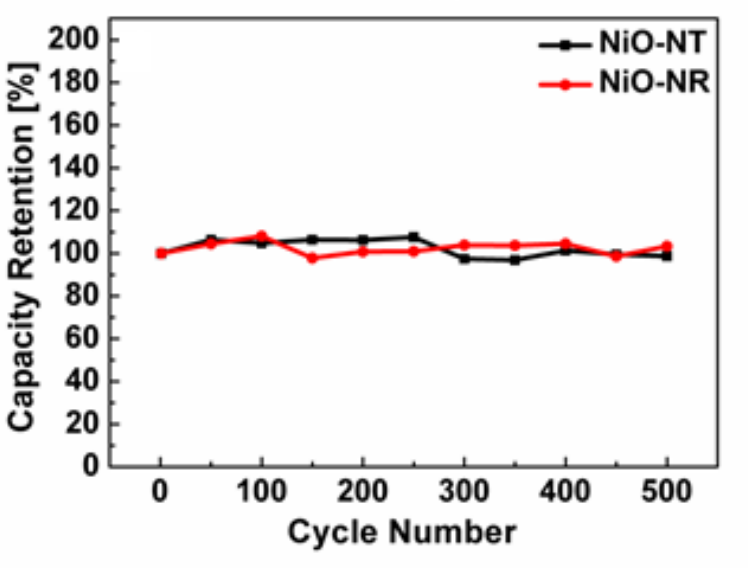

Figure 6.8: The long-term cycling test (500 cycles) at a current density of 125 and 80 A/g for NiO-NT and NiO-NR, respectively are shown. Both nanostructures show stable cycling performance [1] - Reproduced by permission of SpringerOpen.

The idea of morphology control through time of deposition and oxidation is successfully demonstrated here by controlling the morphology from NTs to NRs of Ni/NiO. The pseudocapacitive performance of the synthesized NiO-NSs clearly showed a strong dependence on the morphology which once again strengthens the concept shown in the previous chapters. The NiO-NTs exhibited higher supercapacitance than NiO-NRs at all the scan rates tested here in KOH. Our results for NiO-NTs showed one of the highest values of supercapacitance achievable with NiO nanostructures when compared with literature results for different nanostructure morphologies. The long term performance of our both synthesized NiO-NSs exhibited almost 100 % capacity retention during 500 cycles which indicates the stability of the NSs.

References

[1] F. I. Dar, K. R. Moonoosawmy and M. Es-Souni, *Morphology and property control of NiO nanostructures for supercapacitor applications*, Nanoscale Research Letters **8**, 363 (2013).

[2] G. Lota, T. A. Centeno, E. Frackowiak and F. Stoeckli, *Improvement of the structural and chemical properties of a commercial activated carbon for its application in electrochemical capacitors*, Electrochimica Acta **53**, 2210–2216 (2008).

[3] B. Fang and L. Binder, *A modified activated carbon aerogel for high-energy storage in electric double layer capacitors*, Journal of Power Sources **163**, 616–622 (2006).

[4] B. E. Conway, *Transition from "Supercapacitor" to "Battery" Behavior in Electrochemical Energy Storage*, J. Electrochem. Soc. **138**, 1539–1548 (1991).

[5] S. Sarangapani, B. V. Tilak and C-P. Chen, *Materials for Electrochemical Capacitors Theoretical and Experimental Constraints*, J. Electrochem. Soc. **143**, 3791–3799 (1996).

[6] B. E. Conway, *Electrochemical Supercapacitors: Scientific Fundamentals and Technological Applications*, Plenum Pub Corp, New York (1999).

[7] J. P. Zheng, P. J. Cygan and T. R. Jow, *Hydrous Ruthenium Oxide as an Electrode Material for Electrochemical Capacitors*, J. Electrochem. Soc. **142**, 2699–2703 (1995).

[8] P. Poizot, S. Laruelle, S. Grugeon, L. Dupont and J. M. Tarascon, *Nano-sized transition-metal oxides as negative-electrode materials for lithium-ion batteries*, Nature **407**, 496–499 (2000).

[9] M. Mamak, N. Coombs and G. A. Ozin, *Mesoporous Nickel−Yttria−Zirconia Fuel Cell Materials*, Chem. Mater. **13**, 3564–3570 (2001).

[10] X. Wang, J. Song, L. Gao, J. Jin, H. Zheng and Z. Zhang, *Optical and electrochemical properties of nanosized NiO via thermal decomposition of nickel oxalate nanofibres*, Nanotechnology **16**, 37–39 (2005).

[11] J. Karlsson and A. Roos, *Angle-resolved optical characterisation of an electrochromic device*, Sol. Energy **68**, 493–497 (2000).

[12] M. C. A. Fantini, F. F. Ferreira and A. Gorenstein, *Theoretical and experimental results on Au-NiO and Au-CoO electrochromic composite films*, Solid State Ionics **152**, 867–872 (2002).

[13] E. Makiak and Z. Opilaski, *Transition metal oxides covered Pd film for optical H_2 gas detection*, Thin Solid Films **515**, 8351–8355 (2007).

[14] E. L. Miller and R. E. Rocheleau, *Electrochemical Behavior of Reactively Sputtered Iron-Doped Nickel Oxide*, J. Electrochem. Soc. **144**, 3072–3077 (1997).

[15] J. W. Lang, L. B. Kong, W. J. Wu, Y. C. Luo and L. Kang, *Facile approach to prepare loose-packed NiO nano-flakes materials for supercapacitors*, Chem. Commun. 4213–4215 (2008).

[16] K. Liang, X. Tang and W. Hu, *High-performance three-dimensional nanoporous NiO film as a supercapacitor electrode*, J. Mater. Chem. **22**, 11062–11067 (2012).

[17] Y. Hou, Y. W. Cheng, T. Hobson and J. Liu, *Design and Synthesis of Hierarchical MnO_2 Nanospheres/Carbon Nanotubes/Conducting Polymer Ternary Composite for High Performance Electrochemical Electrodes*, Nano Lett. **10**, 2727–2733 (2010).

[18] H. Jiang, T. Zhao, J. Ma, C. Y. Yan and C. Z. Li, *Ultrafine manganese dioxide nanowire network for high-performance supercapacitors*, Chem. Commun. **47**, 1264–1266 (2011).

[19] A. L. M. Reddy, M. M. Shaijumon, S. R. Gowda and P. M. Ajayan, *Coaxial MnO_2/Carbon Nanotube Array Electrodes for High-Performance Lithium Batteries*, Nano Lett. **9**, 1002–1006 (2009).

[20] Y. G. Guo, J. S. Hu and L. J. Wan, *Nanostructured Materials for Electrochemical Energy Conversion and Storage Devices*, Adv. Mater. **20**, 2878–2887 (2008).

[21] F. I. Dar, S. Habouti, R. Minch, M. Dietze and M. Es. Souni, *Morphology control of 1D noble metal nano/heterostructures towards multi-functionality*, J. Mater. Chem. **22**, 8671–8679 (2012).

[22] G. E. Zima, *Some high temperature oxidation characteristics of Nickel with Chromium additions,* Pasadena California, Office of Naval Research (US Government); 1956. 92p, Seventh technical report. Contract No. N6onr-24430.

[23] V. Srinivasan and J. W. Weidner, *An Electrochemical Route for Making Porous Nickel Oxide Electrochemical Capacitors*, J. Electrochem. Soc. **144**, L210–L213 (1997).

[24] K. W. Nam, W. S. Yoon and K. B. Kim, *X-ray absorption spectroscopy studies of nickel oxide thin film electrodes for supercapacitors*. Electrochimica Acta **47**, 3201–3209 (2002).

[25] J. H. Kim, K. Zhu, Y. Yan, C. L. Perkins and A. J. Frank, *Microstructure and Pseudocapacitive Properties of Electrodes Constructed of Oriented NiO-TiO_2 Nanotube Arrays*, Nano Lett. **10**, 4099–4104 (2010).

[26] R. G. Compton and C. E. Banks, In *Understanding Voltammetry: Chapter 4 Cyclic voltammetry at Macroelectrodes*, World Scientific publishing Co. Pte. Ltd., Singapore, 111–120 (2007).

[27] X. Li, S. Xiong, J. Li, J. Bai and Y. Qian, *Mesoporous NiO ultrathin nanowire networks topotactically transformed from a-$Ni(OH)_2$ hierarchical microspheres and their superior electrochemical capacitance properties and excellent capability for water treatment*, J. Mater. Chem. **22**, 14276–14283 (2012).

[28] K. W. Nam and K. B. Kim, *A Study of the Preparation of NiO_x Electrode via Electrochemical Route for Supercapacitor Applications and Their Charge Storage Mechanism*, J. Electrochem. Soc. **149**, A346–A354 (2002).

[29] S. C. Pang, M. A. Anderson and T. W. Chapman, *Novel Electrode Materials for Thin-Film Ultracapacitors: Comparison of Electrochemical Properties of Sol-Gel-Derived and Electrodeposited Manganese Dioxide*, J. Electrochem. Soc. **147**, 444–450 (2000).

[30] U. M. Patil, R. R. Salunkhe, K. V. Gurav and C. D. Lokhande, *Chemically deposited nanocrystalline NiO thin films for supercapacitor application*, Applied Surface Science, **255**, 2603–2607 (2008).

[31] R. A. Huggins, *Supercapacitors and electrochemical pulse sources*. Sol. Stat. Ionics, **134**, 179–195 (2000).

[32] D. S. Kong, J. M. Wang, H. B. Shao, J. Q. Zhang and C. N. Cao, *Electrochemical fabrication of a porous nanostructured nickel hydroxide film electrode with superior pseudocapacitive performance*, J. Alloys Compd. **509**, 5611–5616 (2011).

[33] B. Ren, M. Fan, Q. Liu, J. Wang, D. Song and X. Bai, *Hollow NiO nanofibres modified by citric acid and the performances as supercapacitor electrod*, Electrochimica Acta, **92**, 197–204 (2013).

[34] S-I. Kim, J-S. Lee, H-J. Ahn, H-K. Song and J-H. Jang, *Facile Route to an Efficient NiO Supercapacitor with a Three-Dimensional Nanonetwork Morphology*, Appl. Mater. Interfaces **5**, 1596–1603 (2013).

[35] M. Liu, J. Chang, J. Sun and L. Gao, *Synthesis of porous NiO using $NaBH_4$ dissolved in ethylene glycol as precipitant for high-performance supercapacitor*, Electrochimica Acta **107**, 9–15 **(**2013).

[36] Z. Lu, Z. Chang, J. Liu and X. Sun, *Stable ultrahigh specific capacitance of NiO nanorod arrays*, Nano Research **4**, 658–665 (2011).

7 Summary and Outlook

Nanomaterials owing to their unique physiochemical properties are receiving remarkable amount of attention in scientific community. In this connection, different materials are being synthesized on nanoscales which are resulting in interesting, enhanced and astonishing properties which not only differ significantly from other materials but also from their bulk counter parts. Along with other structural parameters like shape and dimension, morphology also plays an important role in controlling and defining the properties of these nanomaterials. Therefore, we see a variety of shapes and morphologies of nanomaterials in literature, ranging from nanoparticles, nanoflakes, nanoflowers to self-standing nanorods (NRs) and nanotubes (NTs). To control the morphology of these nanomaterials different approaches and synthesis techniques have been applied. It is however, a challenge to synthesis the nanomaterials in a less complex, cost effective and in a way to easily integrate into the final device. Template aided synthesis is one of the simplest techniques, comparatively it has low processing cost, it provides self-standing and supported nanostructures (NSs) which ensures an easy integration of synthesized nanomaterials into devices. It also provides highly ordered NSs having large effective surface area which is required in certain applications. Moreover, templates allow controlling the dimension and morphology of the nanomaterials depending upon their size and shape.

A lot of different metals, alloys, oxides and organic materials have been synthesized with the help of different templates in literature, among them most common are commercially available anodized aluminum oxide (AAO) and track etched polycarbonate membranes. The different techniques which have employed these templates are sol-gel, layer by layer assembly and

electrodeposition. Among these techniques, electrodeposition is the most suitable one for the deposition of metal oxide and semiconductor nanostructures. Thus in our work we synthesized one-dimensional metal NSs, that is NTs and NRs, with the help of AAO as sacrificial template by employing electrodeposition technique. AAO template is preferred over polycarbonate membranes because it is easy to remove after synthesizing NSs inside it. We readily synthesized monometallic NRs and NTs of Pt, Pd and Au, layered multimetallic (bimetallic Pt-Cu and trimetallic Pt-Ni-Au, Pt-Au-Cu) NTs, surface modified (with add atoms of Ru and Sn) Pt-NTs (Pt-Ru, Pt-Sn and Pt-Ru-Sn) and Nickle oxide (NiO) NTs and NRs. We processed and controlled the morphology of NSs from thin wall and thick wall NTs to NRs under appropriate electrodeposition and annealing conditions. In case of metallic NSs the wall thickness tuning was achieved by controlling the time of electrodeposition while keeping all the other electrodeposition parameters constant. While in case of NiO, Ni-NTs were first synthesized and then further wall thickness tuning and oxidation were achieved by selecting an appropriate temperature and controlling the annealing time.

The aim of this work was not only to synthesize high surface area nanomaterials but also to study their morphology dependent properties such as energy harvesting through electro-oxidation and energy storage capacity for applications in direct liquid fuel cells (DLFCs) and supercapacitors, respectively. Pt and Pd were tested for their performance of electrooxidation of methanol and formic acid respectively while NiO was tested for its performance as redox energy storage supercapacitor. Cyclic voltammetry and chronoamperograms tests were performed on Pt and Pd NSs samples using them as working electrodes in three electrode cell configurations for electrooxidation and long term performance. Similarly cyclic voltammetry and charging-discharging tests were performed on NiO-NSs for supercapacitance behavior evaluation.

The electrocatalysis results for both Pt and Pd NTs show very high electrochemical active surface areas that should make them promising candidates for low cost electrodes in DLFCs. The surface modification of Pt-NTs electrodes with submonolayers of Ru, Sn or Ru/Sn leads to improved performance towards methanol oxidation at different specific voltage ranges. The Sn modified Pt-NTs electrode is particularly effective in terms of lowering the onset potential without substantially altering the maximum peak current density. The Ru-modified electrode exhibits maximum peak current density at moderate voltages, and is in this respect superior to all

the investigated electrodes. A combination of both Ru and Sn leads to intermediate results. Our results clearly show that Ru, Sn, and Ru/Sn modified Pt-NTs electrodes display varied activities in different potential ranges. Their tuneable efficiency and long term stability, combined with the infinitely low Ru-loading and therefore lower costs, make them promising candidates for electrocatalytic applications.

One-dimensional NiO-NSs for energy storage applications were processed using a combination of AAO aided template synthesis and annealing treatments. The suitable selection of annealing time and temperature enabled us to control the morphology of the NiO-NSs, from NTs to NRs. Our electrochemical capacitance results show a large dependence of capacitance on morphology of the NSs. The NiO-NTs structure in particular, shows exceptionally good supercapacitance value; superior to the literature results published so far for different NiO-NSs. Apart from the high capacitance value of our NiO-NSs, they also exhibited excellent rate capability (charge-discharge capacitance at high current density). The long-term stability tested through cyclic charging-discharging showed full capacity retention for both NSs over 500 cycles.

On one hand this work reassures the promise of nanomaterials to offer potential solutions to the demands of efficient energy harvesting from DLFCs and high energy storage capacity in electrochemical supercapacitors. The importance of morphology control of NSs is evident from the results of electrochemical testing which shows strong dependence of electrochemical properties on the morphology pertinent to the electrodes. On the other hand it is expected that presented work will prove a way forward in template aided synthesis and morphology control of nanomaterials through electrodeposition and annealing times. It opens not only further possibilities of processing and controlling the morphology of other metals, oxides and alloys but also of multimetallic NSs for different applications. A proof of the concept for processing of layered multimetallic NTs has been successfully shown in the form of Pt-Cu, Pt–Ni–Au and Pt-Au-Cu which for example might find their application in tuning the optical properties. It is hoped that techniques applied in this work will contribute in morphology controlled processing of many more metals, oxides, alloys and multimetallic NSs.

Acknowledgments

I would like to take this opportunity to sincerely thank almighty God and all of the people who helped, supported and guided me in successfully completing this thesis.

First and foremost, I would like to express my sincere gratitude to Prof. Dr. Mohammad Es-Souni for providing me the opportunity to pursue PhD under his supervision. His consistent guidance and advice greatly supported me during my research. The enthusiasm he has for his research work not only kept me motivated throughout this period, but also developed my interest in nanoscale materials. I benefited numerous times from his valuable scientific inputs during our discussions. I appreciate his contributions of time, instructions, innovative ideas and funding for my PhD.

I am deeply grateful to Prof. Dr. Franz Faupel for supporting and approving me to write my PhD thesis in materials science department of Christian-Albrechts university of Kiel.

I am thankful to Dr. Salah Habouti for sharing his expertise of working with nano materials. I learnt the art of handling and working with nano templates from his experience.

In regard to electrochemistry, I thank Dr. Robert Minch for his guidance, cooperation and fruitful discussions.

I would also like to thank Dipl.-Ing. Matthias Dietze for his co-operation in laboratory. I appreciate his skillful assistance in using laboratory equipment especially for teaching me how to work with scanning electron microscope.

My thanks go to Dr. Kevin Radakishna Moonoosawmy for his scientific intake in our numerous discussions. Especially I got benefited from his wise vision in our joint research on supercapacitors.

I am grateful to Dipl.-Phys Claus-Henning Solterbeck for his significant technical contributions especially in making software to perform charge-discharge and long term performance tests with Source meter.

Andreas Dreher has my thanks for his immediate and efficient support in technical issues in the laboratory which helped avoiding undue resistance in on-going work.

Last but not least I would like to express my heartiest thanks to my parents: father Mohammad Iqbal Dar who supported my decision of coming Germany for higher education, mother Rasheeda Begum for her selfless love and countless prayers for my success. I am also thankful to my brothers and sisters for their well-wishing. I am truly grateful to my wife Nadia Farrukh for patiently waiting for months of writing and supporting me in every possible way. Finally, my cordial thanks go to my beloved daughter Haniya Farrukh for making writing joyful with her cheerful smiles and affection.

List of Publications

1. F. I. Dar, S. Habouti, R. Minch, M. Dietze and M. Es-Souni, *Morphology control of 1D noble metal nano/heterostructures towards multi-functionality*, J. Mater. Chem. **22**, 8671–8679 (2012).

2. Farrukh Iqbal Dar, Kevin Radakishna Moonoosawmy and Mohammed Es-Souni, *Morphology and property control of NiO nanostructures for supercapacitor applications*, Nanoscale Research Letters **8**, 363 (2013).